

5-2013

Improving Cervical Cancer Nodal Boost Radiation Therapy by Quantifying Uncertainties and Exploring Advanced Radiation Therapy Modalities

Zhiqian Yu

Follow this and additional works at: https://digitalcommons.library.tmc.edu/utgsbs_dissertations



Part of the [Medical Biophysics Commons](#)

Recommended Citation

Yu, Zhiqian, "Improving Cervical Cancer Nodal Boost Radiation Therapy by Quantifying Uncertainties and Exploring Advanced Radiation Therapy Modalities" (2013). *The University of Texas MD Anderson Cancer Center UTHealth Graduate School of Biomedical Sciences Dissertations and Theses (Open Access)*. 333. https://digitalcommons.library.tmc.edu/utgsbs_dissertations/333

This Dissertation (PhD) is brought to you for free and open access by the The University of Texas MD Anderson Cancer Center UTHealth Graduate School of Biomedical Sciences at DigitalCommons@TMC. It has been accepted for inclusion in The University of Texas MD Anderson Cancer Center UTHealth Graduate School of Biomedical Sciences Dissertations and Theses (Open Access) by an authorized administrator of DigitalCommons@TMC. For more information, please contact digitalcommons@library.tmc.edu.

**IMPROVING CERVICAL CANCER NODAL BOOST RADIATION
THERAPY BY QUANTIFYING UNCERTAINTIES AND EXPLORING
ADVANCED RADIATION THERAPY MODALITIES**

by

Zhiqian Henry Yu B.S.

Approved:

Rajat Kudchadker, Ph.D.
Supervisory Professor

Laurence E Court, Ph.D.

Lei Dong, Ph.D.

Patricia J Eifel, M.D.

Ann H Klopp, M.D., Ph.D.

Firas Mourtada, Ph.D.

Susan Tucker, Ph.D.

Approved:

Dean, The University of Texas
Graduate School of Biomedical Sciences at Houston

**IMPROVING CERVICAL CANCER NODAL BOOST RADIATION
THERAPY BY QUANTIFYING UNCERTAINTIES AND EXPLORING
ADVANCED RADIATION THERAPY MODALITIES**

A

DISSERTATION

Presented to the Faculty of
The University of Texas
Health Science Center at Houston
and
The University of Texas
MD Anderson Cancer Center
Graduate School of Biomedical Sciences
in Partial Fulfillment

of the Requirements

for the Degree of

DOCTOR OF PHILOSOPHY

by

Zhiqian Henry Yu, B.S.
Houston, Texas

May, 2013

Acknowledgements

I would like to take this opportunity to thank everyone that has been part of my graduate school journey especially my advisors Dr. Lei Dong and Dr. Rajat Kudchadker. Thank you Dr. Dong for giving me the opportunity to enter the field of medical physics and patiently teaching me the basic in-and-outs of the field. Thank you Dr. Kudchadker for taking over after Dr. Dong left and being such a great career and life coach. I am extremely fortunate to have two great mentors.

I also want to thank the rest of my committee, Dr. Firas Mourtada, Dr. Patricia Eifel, Dr. Susan Tucker, Dr. Ann Klopp, and Dr. Laurence Court for not only helping me on my project but everything else in life as well. Thank you for being patient, encouraging, and providing constant guidance every step of the way. You were the best advisory committee any student could hope for and every single one of you has made such huge contributions to my project and my knowledge.

To the computational scientist group including Joy Zhang, Yongbin Zhang, Jinzhong Yang, and Ryan Williamson, thank you for teaching me MATLAB and debugging my programs when I am at dead ends. Without your help, this project would have taken much longer to complete. To the physicists and dosimetrist in the GYN service including Ann Lawyer, Laura Rechner, Paula Berner, Teresa Bruno, and Mandy Cunningham, thank you for teaching me everything about the clinical aspects of radiation therapy of cervical cancer, especially the art of brachytherapy.

I want to thank my former and current classmates Adam Melancon, Blake Cannon, Ming Yang, Peter Park, Jason Matney, Joey Cheung, Adam Yock, and Luke Hunter for being there to bounce ideas off and always keeping the daily grind entertaining.

I want to thank Georgeanne Moore, Linda Stall, Bill LaCour, Norma Hall, Scharlene Wilson, and Sarah Welch for always providing me assistance and making things go as smoothly as possible even when trouble always seems to find me.

Last but not least, I want to thank my parents for their nonstop encouragement and being supportive of all my decisions. I also want to thank my dearest, Lauren Yu, for being by my side this entire journey. Together we went through the good and rough times. Thank you for keeping me humbled and sane.

Words cannot express how much you all mean to me and I will cherish the entire graduate experience for the rest of my life.

**IMPROVING CERVICAL CANCER NODAL BOOST RADIATION
THERAPY BY QUANTIFYING UNCERTAINTIES AND EXPLORING
ADVANCED RADIATION THERAPY MODALITIES**

Publication No. _____

Zhiqian Henry Yu, Ph.D.

Supervisory Professor: Rajat Kudchadker, Ph.D.

Radiation therapy for patients with intact cervical cancer is frequently delivered using primary external beam radiation therapy (EBRT) followed by two fractions of intracavitary brachytherapy (ICBT). Although the tumor is the primary radiation target, controlling microscopic disease in the lymph nodes is just as critical to patient treatment outcome. In patients where gross lymphadenopathy is discovered, an extra EBRT boost course is delivered between the two ICBT fractions. Since the nodal boost is an addendum to primary EBRT and ICBT, the prescription and delivery must be performed considering previously delivered dose. This project aims to address the major issues of this complex process for the purpose of improving treatment accuracy while increasing dose sparing to the surrounding normal tissues.

Because external beam boosts to involved lymph nodes are given prior to the completion of ICBT, assumptions must be made about dose to positive lymph nodes from

future implants. The first aim of this project was to quantify differences in nodal dose contribution between independent ICBT fractions. We retrospectively evaluated differences in the ICBT dose contribution to positive pelvic nodes for ten patients who had previously received external beam nodal boost. Our results indicate that the mean dose to the pelvic nodes differed by up to 1.9 Gy between independent ICBT fractions.

The second aim is to develop and validate a volumetric method for summing dose of the normal tissues during prescription of nodal boost. The traditional method of dose summation uses the maximum point dose from each modality, which often only represents the worst case scenario. However, the worst case is often an exaggeration when highly conformal therapy methods such as intensity modulated radiation therapy (IMRT) are used. We used deformable image registration algorithms to volumetrically sum dose for the bladder and rectum and created a voxel-by-voxel validation method. The mean error in deformable image registration results of all voxels within the bladder and rectum were 5 and 6 mm, respectively.

Finally, the third aim explored the potential use of proton therapy to reduce normal tissue dose. A major physical advantage of protons over photons is that protons stop after delivering dose in the tumor. Although theoretically superior to photons, proton beams are more sensitive to uncertainties caused by interfractional anatomical variations, and must be accounted for during treatment planning to ensure complete target coverage. We have demonstrated a systematic approach to determine population-based anatomical margin requirements for proton therapy. The observed optimal treatment angles for common iliac nodes were 90° (left lateral) and 180° (posterior-anterior [PA]) with additional 0.8 cm and

0.9 cm margins, respectively. For external iliac nodes, lateral and PA beams required additional 0.4 cm and 0.9 cm margins, respectively.

Through this project, we have provided radiation oncologists with additional information about potential differences in nodal dose between independent ICBT insertions and volumetric total dose distribution in the bladder and rectum. We have also determined the margins needed for safe delivery of proton therapy when delivering nodal boosts to patients with cervical cancer.

Table of Contents

List of Tables	xiv
List of Figures	xv
Chapter 1: Introduction	1
1.1 Radiation Therapy for Cancer Treatment	1
1.1.1 What is Radiation Therapy?.....	1
1.1.2 Planning and Delivery of Radiation Therapy	1
1.2 Background of Cervical Cancer.....	3
1.2.1 Statistics and Pathology	3
1.2.2 Treatment Methods	3
1.2.3 Radiation Therapy of Cervical Cancer	5
External Beam Radiation Therapy.....	6
Intracavitary Brachytherapy.....	8
1.2.4 Boosting Radiation Dose to Positive Nodes	14
1.3 Current Obstacles (and possible solutions) in High Precision Radiation Therapy of Cervical Cancer	19
1.3.1 Motivation for this Project.....	19

1.3.2 Difficulty in Prescribing Nodal Boost	20
1.3.3 Rethinking How Nodal Boost Dose is Delivered	22
1.4 About Dissertation	23
1.4.1 Purpose and Hypothesis.....	23
1.4.2 Specific Aims.....	23
1.4.3 Organization of Dissertation	24
 Chapter 2: Variability in Pelvic Nodal Dose between Independent Intracavitary Brachytherapy Fractions for Treatment of Cervical Cancer.....	
2.1 Specific Aim 1	25
2.2 Introduction.....	25
2.3 Methods and Materials.....	26
2.3.1 Patient Cohort	26
2.3.2 Aligning ICBT Film Images and 3D Dose to EBRT CT Image Sets	27
2.3.3 Analyzing Nodal Dose Differences between Independent ICBT Fractions.....	33
2.4 Results.....	36
2.4.1 Validation of Image Registration Algorithm	36
2.4.2 Nodal Dose Differences from Independent ICBT Fractions	38

2.4.3 Correlation between Tandem and Applicator Location Variations and Nodal Dose Difference	42
2.5 Discussion	43
2.5.1 Nodal Dose Variations in the Proximal Pelvic Region.....	45
2.5.2 Nodal Dose Variations in the Distal Pelvic Region.....	46
2.5.3 Differences in Result between Mean Dose and D_{90}	47
2.5.4 Limitations and Assumptions	48
2.6 Conclusion	49
Chapter 3: Voxel-by-Voxel Bladder and Rectum Dose Accumulation between External Beam Radiation Therapy and Intracavitary Brachytherapy.....	50
3.1 Specific Aim 2	50
3.2 Introduction.....	50
3.2.1 Importance of Accurately Evaluating Total Bladder and Rectum Dose for the Prescription of Nodal Boost	50
3.2.2 Image registration	51
3.2.3 In-house accelerated demons algorithm.....	53
3.2.4 Using DIR for Dose Summation of Bladder and Rectum.....	55
3.3 Methods and Materials.....	56

3.3.1 Patient Cohort	56
3.3.2 Contour Based Validation Metrics.....	56
3.3.3 Binary deformation	58
3.3.4 Voxel-by-voxel Validation Method.....	59
3.3.5 Validation of Deformation Results	68
3.4 Results.....	68
3.4.1 Contour Based Validation.....	68
3.4.2 Mean Error from Voxel-by-Voxel Validation	69
3.5 Discussion	71
3.5.1 The importance of voxel-by-voxel validation.....	71
3.5.2 Comparing Binary and Normal Methods Using DIR Evaluation Metrics.....	74
3.6 Conclusion	77

Chapter 4: Beam Angle Specific Margins to Account for Anatomical Uncertainties

during Proton Therapy in Nodal Boost Planning for Cervical Cancer	78
4.1 Specific Aim 3	78
4.2 Introduction.....	78
4.3 Methods and Materials.....	80
4.3.1 Patient Cohort	80

4.3.2 Automatic Contour Delineation	81
4.3.3 Patient Setup	81
4.3.4 Calculation of anatomical changes	82
4.3.5 Margin calculation	84
4.3.6 Proton Therapy Planning Test Case.....	85
4.4 Results.....	86
4.4.1 Patient Weight Changes.....	86
4.4.2 Distal and Proximal Margin Requirements for Common and External Iliac Nodes	86
4.4.3 Comparison of Photon and Proton Dose Distribution in Test Case.....	89
4.5 Discussion	91
4.5.1 Beam Angle Dependence of Interfractional Anatomical Variations	91
4.5.2 Differences in Distal and Proximal Margin Requirements.....	93
4.5.3 Differences between Common and External Iliac Nodal Margin Requirements	94
4.5.4 Potential Small Bowel Sparing using Protons for Nodal Boost	95
4.5.5 Assumptions and Limitations	95
4.6 Conclusion	96

Chapter 5: Conclusion.....	97
5.1 Summary of the Problems, Purpose, and Hypothesis.....	97
5.2 Specific Aims.....	98
5.2.1 Specific Aim 1	98
5.2.2 Specific Aim 2	99
5.2.3 Specific Aim 3	99
5.3 Translating Findings to the Clinic.....	100
5.4 The End?	101
Bibliography	102
Vita.....	122

List of Tables

Table 1: Results for auto-alignment algorithm. A reference DRR image set was first generated using isocenter near the center of the pelvis. Shifted-DRR image set were generated by shifting the isocenter ± 2 cm, ± 3 cm, ± 4 cm in the LR, AP, and SI directions, respectively.	37
Table 2: Evaluation of contour agreement between deformed and delineated for bladder using image intensity alone (Normal) and Binary methods.....	69
Table 3: Evaluation of contour agreement between deformed and delineated for rectum using image intensity alone (Normal) and Binary methods.....	69
Table 4: Mean errors in registration (mm) for all voxels in the bladder and rectum.....	70

List of Figures

- Figure 1: The Fletcher-Suit-Delclos applicator system which composes of a tandem and two ovoids. In the picture, one can see different ovoid sizes (mini to large) and tandems with varying angles (15° to 45°). Different combinations of tandem and ovoids can be used depending on patient specific anatomical features.9
- Figure 2: Locations of Point A, B, bladder and rectum as defined in ICRU 38. Point A is defined as the point 2 cm lateral to the central canal of the uterus and 2 cm up from the external os. Point B is defined as the point crossing the internal OS, parallel to the tilt of the pelvis, and 5 cm lateral from the midline. Bladder and rectum points can be identified on the lateral images. The bladder point is located on the most posterior surface point of the Foley balloon. The rectal point is located on a line drawn from the midpoint of the ovoids and 5 mm behind the posterior vaginal wall.13
- Figure 3: Kaplan-Meier disease-specific survival probability curves separated by (A) FIGO staging and (B) PET detected nodal involvement. (Kidd, E et al: J Clin Oncol Vol. 28, 2010: 2108-13. Reprinted with permission. © 2010 American Society of Clinical Oncology. All rights reserved.)15
- Figure 4: Example of extended field EBRT which includes primary disease, pelvic nodes, and para-aortic nodes. Two four-field 3D-CRT sets of beams matching at L5 were used.16

- Figure 5: The lymphatic trapezoid of Fletcher as defined by ICRU Report 38 (61). Shows the method to determining external iliac, common iliac, and para-aortic nodal dose from x-ray films. The nodal points are based on bony locations since there is no soft tissue contrast on radiographs.....18
- Figure 6: Example of beam setup and dose distribution for a patient receiving nodal boost in both para-aortic (A) and external iliac (B) nodal regions. Para-aortic nodes were planed and treated with 8-field IMRT while external iliac nodes are treated with two field AP-PA beams.....19
- Figure 7: Schematic of the procedure to determine differences in nodal dose between independent intracavitary brachytherapy (ICBT) fractions. First, films from ICBT fractions 1 and 2 (ICBT 1 and ICBT 2) were aligned to the computed tomography (CT) image set from treatment simulation (sim) performed before delivery of the nodal boost. Specifically, the original ICBT clinical plans were replicated using an Oncentra treatment planning system with dwell positions identical to those in the original clinical plans, and dose calculations were performed using guidelines provided by the American Association of Physicists in Medicine Radiation Therapy Committee Task Group 43 (87, 88). To permit alignment of ICBT film images to CT images, digitally reconstructed radiographs (DRRs) were generated from CT images in the anterior-posterior (AP) and lateral (Lat) directions. The replicated ICBT films and the DRRs were then aligned using a published algorithm (89). The alignment result was used to shift the ICBT dose into the CT coordinate system to obtain shifted doses for the first and second ICBT fractions, and these doses were imported into a Pinnacle (PINN) treatment planning system. Finally, differences in dose were analyzed volumetrically.....28

Figure 8: User interface created in-house using MATLAB for aligning digitally reconstructed radiographs (DRRs) and film images. Auto-alignment results can be verified manually by using the graticules and fusion display.	30
Figure 9: Reference DRR and 4 out of the 8 shifted DRRs used for validation testing of our rigid alignment algorithm. Only shifts in the LR and SI direction are shown in figure.	32
Figure 10: Tandem angle (θ) was determined by measuring the separation in angle between the tandem and midline of the pelvis.	35
Figure 11: Differences in system shifts between the first and second intracavitary brachytherapy fractions. Variation was smallest in the lateral direction, while most variation occurred in the anterior-posterior direction. Most shifts between the first and second fractions were in the anterior and inferior direction. Box graphs show 25th percentile, median, 75th percentile, and outliers for variations in each axis.	36
Figure 12: Approximate centroid locations of all analyzed nodes for all patients displayed on an atlas computed tomography image. The blue and green spheres represent nodes in the distal and proximal pelvic regions, respectively.	39
Figure 13: Differences between the expected and delivered nodal dose from intracavitary brachytherapy for the proximal and distal pelvic regions. Box graphs show 25th percentile, median, 75th percentile, and outliers for both the mean nodal dose and the dose received by at least 90% of the nodal volume (D_{90}). ...	41
Figure 14: Graphs of normalized dose differences for pelvic nodes between the first and second intracavitary brachytherapy (ICBT) fractions versus applicator changes between the first and second ICBT fractions for relationships with significant correlations ($p < 0.05$).	43

Figure 15: Example of a static (inhale) and a moving (exhale) image taken from a 4-dimensional CT image set. Deformation field resulted from DIR are shown on the moving image. We can see that in order for the exhale phase to be deformed to match the inhale phase, voxels (especially ones near the diaphragm) must be transformed inferiorly resulting in expansion of the lungs.....	53
Figure 16: Example showing the differences between EBRT-CT and ICBT-CT with the bladder (yellow) and rectum (blue) delineated by a radiation oncologist. The image on the right shows deformed contours (colorwash) mapped onto the ICBT-CT image. One can see that neither bladder nor rectum agreed well with radiation oncologist delineated contours.	58
Figure 17: Example of binary EBRT-CT and binary ICBT-CT generated based on radiation oncologist drawn contours. The image on the right shows binary deformed contours (colorwash) mapped onto the ICBT-CT image. One can see that compared to using image intensities alone (Figure 16), both deformed bladder (yellow) and rectum (blue) contours agreed very well with their delineated counterparts.....	59
Figure 18: Using a reference patient to create a group of deformation fields.	62
Figure 19: The group of deformation field is then used to create a inter-patient deformation field.....	63
Figure 20: Using the Inter-Patient Deformation Field, we generated an artificial population CT image.....	63
Figure 21: Creating a group of deformation fields between external beam CT images and brachytherapy images.	65

Figure 22: Using the group of intra-patient deformation fields to create a population deformation field between external beam radiation therapy and brachytherapy CT images (Intra-Patient Deformation Field).....	66
Figure 23: The deformation field between the Reference images (Ref Def Field) is needed for creating the simulation ICBT image.....	66
Figure 24: In order to create the ICBT Artificial CT, the original ICBT-CT Ref must go through a few transformations into different CT image space.	67
Figure 25: Example of EBRT Artificial CT and ICBT Artificial CT generated using $D_{max} = 2$. Since our choice for D_{max} is not large, the deformation between the two images is not as severe.....	67
Figure 26: Histogram of errors in registration between deformed and known deformation fields. Both bladder and rectum were analyzed using normal and binary deformation methods. D_{max} in this example was 2.....	71
Figure 27: Sagittal view of total magnitude registration errors for normal and binary methods for each voxel. One can see that errors in registration on the normal method occurred at places where voxels lacked correspondence between the EBRT-CT and ICBT-CT images. For the binary method, registration errors were greatest in regions where deformation was large.....	76
Figure 28: Simulation of daily treatment setup by transferring target contours (yellow) from Reference to Daily CT image sets using bony structures (red).....	82
Figure 29: A ray-tracing method was used to determine the water-equivalent path-length (WEPL) from the patient surface to the distal and proximal edges of all targets. Ray tracing is parallel to the treatment beam direction. This method results in two 2-dimensional matrices that represent the distal and proximal WEPL map for each target on any particular computed tomography scan.	83

Figure 30: After the water-equivalent path-length (WEPL) maps for both distal and proximal surfaces were obtained on all planning and weekly computed tomography (CT) images, the reference planning maps were subtracted from each daily map to obtain the variation maps. The WEPL difference value to cover 95th percentile of the pixels was used as the margin needed to account for anatomical variations on that particular fraction. Multiple measurements were obtained for each repeat CT image and a group of patients.....84

Figure 31: Range margins for common (a) and external iliac (b) nodes were analyzed. Several angles were selected to test the impact of beam angle on the magnitude of change in the proton beam range due to anatomical variation. Box graphs showing median, 75th percentile, 90th percentile, and outliers for both distal and proximal variations are shown.....88

Figure 32: Differences between the dose-volume histograms for intensity-modulated radiation therapy (IMRT) and proton therapy for both common iliac and external iliac nodes. Three-field IMRT plans were used for each node. A 2-field proton plan was used for the common iliac nodes, and a single proton posterior-anterior field was used for the external iliac nodes. The small bowel dose was reduced by half with proton therapy.....90

Figure 33: Examples of anatomical variations at different beam angles. Bowel path differences can be seen clearly in (a) and (b) for the 315° (right anterior oblique) angle. Differences in subcutaneous adipose tissue can be seen in (c) and (d). In both cases, differences in range are greater than the spread-out Bragg peak of the beam.93

Chapter 1: Introduction

1.1 RADIATION THERAPY FOR CANCER TREATMENT

1.1.1 What is Radiation Therapy?

Ever since x-rays were discovered by Wilhelm Conrad Röntgen in 1895, it did not take long for it to be adopted for both diagnostic and therapeutic uses. One of the first reported uses of radiation for therapeutic purposes was by an Austrian surgeon named Leopold Freund when he noted the disappearance of a mole following x-ray radiation in 1896 (1). Although radiation therapy has advanced tremendously in the past century, the basic biological principles have remained the same; deliver sufficient ionizing radiation to malignant cells with the purpose of breaking enough chemical bonds in the malignant cell DNA to damage it and prevent cell division. However, the challenge in radiation therapy (RT) is that radiation does not differentiate between malignant and normal healthy cells. Therefore, advances in RT have been primarily in the direction of minimizing deposition of radiation to normal cells while maximizing radiation deposition to malignant cells.

1.1.2 Planning and Delivery of Radiation Therapy

Regardless of treatment modality and site, all radiation therapies contain three major components; simulation, planning, and delivery. For example, in external beam radiation therapy, patients are first simulated on a computed tomography (CT) scanner. This provides radiation oncologists volumetric information about location of disease and normal tissue. Also, the Hounsfield unit (HU) of voxels of a CT scan acquired from a calibrated CT scanner

can be converted to electron density, which gives treatment planning systems the capability of heterogeneous dose calculation (2). CT simulation is followed by treatment planning. Normal tissues and treatment targets are delineated by the radiation oncologist. Physicists or dosimetrists then generate treatment plans which satisfy the prescription criteria set by radiation oncologists while minimizing radiation to the normal tissues. Finally, after the plans are approved by the radiation oncologists, patients start receiving daily treatment at typically 2 Gy per fraction delivered using a linear accelerator.

One of the potentially major problems in the current RT process is that the simulation CT scan only represents a snapshot of the patient's anatomy and the assumption that this represents the patient through the entire treatment is made. Since most radiation therapy courses last 6 – 7 weeks, the assumption that patient anatomy remains unchanged through the entire treatment is naïve. However, the effects of anatomical variation on target dose coverage have historically been minimal since beam configurations were simplistic and margins used were generous. With new technologies such as intensity modulated radiation therapy (IMRT), treatment plans have become more conformal, which leads to increased sensitivity to anatomical changes.

Uncertainty caused by anatomical variation is just one of many uncertainties present in radiation therapy. As technologies become more advanced and more conformal delivery methods are developed, better understanding of uncertainties is essential to minimize the risk of underdosing the target. Although some uncertainties are universal, such as CT number and dose calculation, most uncertainties, including anatomical variations, are treatment site specific. This work focuses on uncertainties in the treatment of cervical cancer, especially in

the treatment of lymph nodal boost, with the hope of improving both the treatment planning and dose delivery process.

1.2 BACKGROUND OF CERVICAL CANCER

1.2.1 Statistics and Pathology

The cervix is the area connecting the lower part of the uterus and upper vagina. According to the statistics collected by International Agency for Research on Cancer in 2008 (3), cervical cancer is the third most common type of cancer in women worldwide. However, mortality rates of cervical cancer in the United States and other Western countries have reduced dramatically because of advanced screening techniques such as Pap smears. The National Cancer Institute estimates that there were 12,170 new cases and 4,220 deaths in the United States in 2012 (4). Pathology of cervical cancer suggests that more than 75% of all cervical cancer cases are squamous cell carcinoma with the remaining composed of adenocarcinoma and undifferentiated neuroendocrine.

1.2.2 Treatment Methods

Surgery, chemotherapy, and radiation therapy may all be incorporated into treatment of cervical cancer. Cancer characteristics and side effects must be considered by the radiation oncologists when determining which treatment option best suits the patient. Clinical staging of invasive cervical cancer are classified using the internationally accepted International Federation of Gynecology and Obstetrics (FIGO) system (5). Originally created in 1938 with four major stage groupings, the system has undergone many revisions including the creation

of substages, which starting in 1994 distinguishes microinvasion (IA1 and IA2) and cervical diameter (IB). The system is unique because it is a clinical and not a surgical or radiographic staging system. Although it is not perfect, FIGO stages correlates with outcome when classification rules are strictly followed.

Surgery can be most effectively used in early stage cervical cancer cases. In patients with stage IA1 disease, where the risk of extracervical involvement is low, type I simple extrafascial hysterectomy can be performed. Type II radical hysterectomy and pelvic lymph node dissection is generally recommended for stage IA2 and IB1 cervical cancers. For more advanced cancers, ultra-radical surgical procedures may be performed, although definitive chemoradiation is generally recommended in these cases.

Radiation can be used to treat cervical cancer at all stages. Early stage cases such as IA1 and IA2 can be effectively treated with intracavitary brachytherapy alone for patients who are not operative candidates (6, 7). More advanced cases require external beam radiation therapy to treat the nodes as well. The debate between RT and surgery has been a heated topic with original research showing approximately equal 5 year survival rate of 80% for both treatment modalities (8). However, retrospective studies could be biased since younger patients in better health tend to opt for surgical methods because RT could potentially lead to loss of reproductive function and secondary cancers. On the other hand, one prospective study comparing RT to surgery showed equivalent disease control but a higher rate of grade 2 to 3 complications in patients who received hysterectomy (9). In addition to being used alone, radiation therapy is often used in combination with surgery. Two recent prospective studies have shown the benefits of postoperative pelvic radiation therapy for patients with

intermediate risk features (10, 11). These randomized trials have shown a 46% reduction in risk of recurrence and statistically significant improvements in rate of death in patients receiving postoperative radiation.

In the past 30 years, many researchers have investigated using either sequential or concurrent chemotherapy in combination with radiation therapy. Although initial results for neoadjuvant chemotherapy showed improved tumor response, they did not show improved survival rates (12-16). However, prospective trials published around the year 2000 showed significant improvement in overall survival, disease-free survival, and local control rates when cisplatin based chemotherapy was used concurrently with radiation therapy (11, 17-20). For example, one of the studies has shown improved 5-year survival rates for patients with stage IB to IIB disease (79% versus 55%) (18). Because findings in those studies were so significant, the National Institute of Health made concurrent chemoradiation the standard of care for patients with locally advanced cervical cancer (21).

1.2.3 Radiation Therapy of Cervical Cancer

The goal of radiation therapy is to deliver sufficient dose to the target without exceeding normal tissue tolerance. However, in most cases of radiation therapy of cervical cancer, paracervical sites and regional lymph nodes are part of the treatment target area in addition to primary tumor. This makes the target irregularly shaped and conformal treatment planning very difficult. Because of greater than 3 cm interfractional internal organ motion (22), large treatment planning margins must be used to assure target coverage throughout entire treatment. However, using large margins often also means that normal tissues adjacent

to the target, such as bladder, rectum, sigmoid, and small bowels, are included in the treatment fields as well. Therefore, if dose is delivered using external beam RT alone, tolerance of normal tissues will be reached prior to the targets receiving the prescription dose (23-25). To maintain normal tissue dose below tolerance, intracavitary brachytherapy (ICBT) is normally given in conjunction with external beam RT. Brachytherapy treatments take full advantage of the inverse square law, delivering high doses to tissue closest to the source while sparing normal tissue beyond a few centimeters.

External Beam Radiation Therapy

There are two major functions of external beam radiation therapy (EBRT); to control microscopic disease and reduce size of primary tumor. EBRT treatment fields must cover the cervix, paracervical tissues which include the broad ligaments and uterosacral ligaments, and involved lymphatic nodes. The most common treatment field technique is using four fields (anterior-posterior [AP] and laterals). Traditionally, this was the best option because this field setup spared superficial tissue when low energy beams such as Co-60 sources and 6MV photons were used. Modern linear accelerators can generate greater than 15MV beams which makes a two field setup using only AP-PA beams also acceptable. Most radiation oncologists still prefer the traditional four field setup because studies have shown that using four beams instead of two can reduce dose to the small bowel and rectum (26). Four field box treatments are often also referred to as 3-dimensional conformal treatment (3D-CRT). Radiation oncologists are responsible for delineation of uterus, nodes, vagina, cervix, bladder, rectum, and margins for the fields.

In recent years, many institutions have explored the usage of IMRT for women with cervical cancer (27-35) with the hope of creating better conformal plans for normal tissue sparing. Unlike 3D-CRT, IMRT uses inverse planning techniques which automatically create a plan based on series of planner defined constraints. Planning studies so far have shown decreased bladder, rectum, small bowel, and even bone marrow dose without compromising target coverage when IMRT is used instead of 3D-CRT (28, 29, 32, 33). Prospective follow-up studies comparing IMRT and 3D-CRT have also shown less acute and chronic gastrointestinal (GI) toxicity for patients receiving IMRT (27, 30, 31, 34). Another method of delivering intensity modulated radiation therapy is by using volumetric modulated arc therapy (VMAT) (36). Unlike traditional IMRT, which delivers dose in using predefined fixed angles, VMAT deliver dose using continuous gantry rotation and multileaf collimator motion with modulated dose rate. A planning study done by Cozzi et al. comparing IMRT to intensity modulated arc therapy with results showing improved homogeneity and conformality index with VMAT and decrease in rectum and bladder mean dose (37). Although all these results appear promising, the studies do not have enough patients and long follow-up duration to conclude that local control and survival rates are comparable to traditional 3D-CRT methods. Also, with the exception of the study by Van de Bunt et al. (35), which have shown anisotropic anatomical variation requiring treatment margin as large as 2.4 cm, none of the studies have analyzed anatomical variations during a RT course and its effect on conformal treatment methods. Because of uncertainties related to patient outcomes using conformal methods and large interfractional anatomical variations, most intact cervical

cancer patients receiving primary EBRT at The University of Texas MD Anderson Cancer Center are still treated with 3D-CRT.

Intracavitary Brachytherapy

ICBT is an integral part of radiation therapy for cervical cancer. Its primary function is to deliver boost dose to the gross tumor by using solid applicators which consists of a central tube called tandem and two lateral capsules, called ovoids. Figure 1 shows an example of the classic Fletcher-Suit-Delclos applicator system. There are three major reasons why the cervix is ideal for being irradiated using ICBT. First, radioactive sources can be placed in the center (in middle of cervix), above (inside the uterus), and below (inside the vagina) the tumor. Second, packing can be used in the vagina to push the bladder and rectum further away from the radioactive sources, which lowers the dose and toxicity to these organs. Finally, the uterus and vagina are relatively radioresistant and can tolerate doses as much as 90 Gy without developing radiation related complexities (38). Historically, ICBT was delivered using Radium-226 (^{226}Ra), which has the average energy of 830 keV and half-life of 1602 years. However, because of the high energy photon released (up to 2.45 MeV), ^{226}Ra sources require thick shielding. Also, since it is also an alpha emitter, it is extremely hazardous if the encapsulation holding the radium sulfate powder were to break. An alternative source to ^{226}Ra is Cesium-137 (^{137}Cs) which is a 662 keV gamma-ray emitting radioisotope with 30 year half-life. ^{137}Cs is better than ^{226}Ra because it requires less shielding and is also less hazardous. It overtook ^{226}Ra as the most used source for ICBT in the mid 1970s. Since the introduction of afterloading methods, Iridium-192 (^{192}Ir) has become the

source of choice for ICBT. ^{192}Ir has average energy of 380 keV and half-life of 74 days. The lower energy compared to ^{226}Ra and ^{137}Cs makes shielding more convenient and because it has high specific activity, it has enough activity for high-dose-rate treatments (described in more detail next paragraph). The only downside of using ^{192}Ir is its short half life. However, 74 days is long compared to the average treatment time and dose rate decreases by less than 2% during treatment.

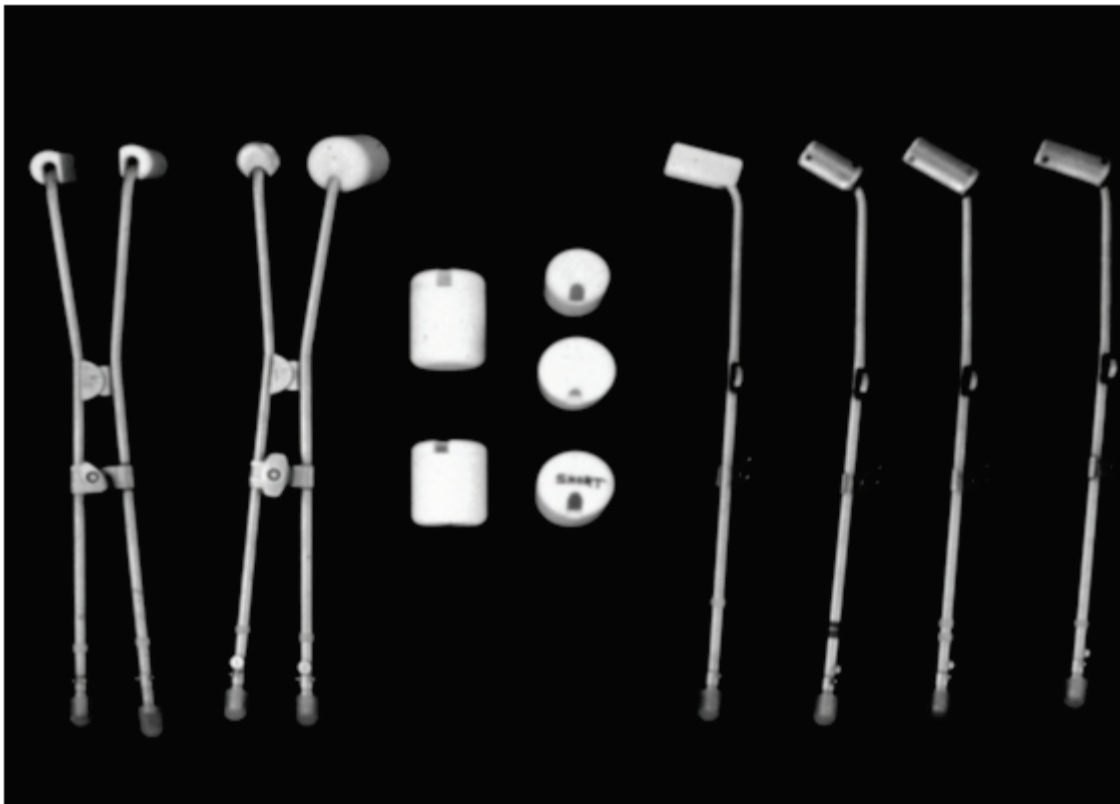


Figure 1: The Fletcher-Suit-Delclos applicator system which composes of a tandem and two ovoids. In the picture, one can see different ovoid sizes (mini to large) and tandems with varying angles (15° to 45°). Different combinations of tandem and ovoids can be used depending on patient specific anatomical features.

Historically, low-dose-rate (LDR) ICBT was the preferred method of treatment because it offers greatest radiobiological advantages (39-44). It is a unique situation where

damage and repair occurs at the same time. When the dose rate is as low as 1 cGy/min (LDR dose rates are typically between 0.7 to 1 cGy/min), radiosensitivity of cells decrease and the curved shoulder portion of the cell survival curve becomes straighter. This effect is critical because as the survival curves become straighter, the survival percentage difference increases between normal tissues and tumor cells as dose is increased. Dose delivered using LDR has almost identical biological effect as dose delivered in 2 Gy per fraction using external beams. One of the downsides of LDR is in order to deliver enough dose to the target at low dose rates, long delivery times (typically 72 hours), has to be used. The patient must be hospitalized and immobile through the entire process, making it very uncomfortable and inconvenient. When ICBT was first performed, manual loading methods were used. The sources were preloaded into the applicator before it was inserted into the patient in the operating room. However, to reduce radiation to medical personnel, afterloading systems, where sources are manually or remotely loaded into the applicator after it has been inserted into the patient, were developed and used in the clinic. Afterloading systems also have the advantage of allowing dose distribution optimization based on patient anatomy and applicator location after insertion.

In the past fifteen years, a new method of delivering ICBT, using high-dose-rate (HDR) sources ($>1\text{Gy/min}$), has gained popularity around the world (45-56). This technique uses a computer controlled remote afterloader to precisely move a single ^{192}Ir source with activity greater than 10 Ci (3.7×10^{11} Bq) to different spots (dwell positions) in the applicator. With tremendous precision in timing and location, a single source can be used to replicate dose distribution of a LDR treatment. Also, when HDR planning is done using CT images,

the dose distribution can be inversely optimized like IMRT to create more conformal treatment plans with greater normal tissue sparing. The advantage of using HDR is that the entire treatment process takes only a few minutes instead of days. This leads to more convenience for patients and much less radiation exposure to medical personnel. The major disadvantage of HDR brachytherapy is that the radiation biology aspect is not well understood. The current method for calculating biological equivalent (BED) dose of HDR uses the identical linear-quadratic model as EBRT, which does not factor in typical brachytherapy BED calculation parameters, such as repair time and exposure duration. Also, there is no standard method for the delivery of dose using HDR. The dose per fraction and number of fractionations can vary significantly between institutions. The most common fractionation scheme in the United States is once per week using 6 Gy per fraction concurrent with primary EBRT. Literature comparing outcome results between HDR and LDR have showed equal survival rates between the two for small tumors but significantly lower survival rates for patients with stage IIIB disease when HDR is used (47, 49, 51, 52, 55).

A third brachytherapy dose delivery method named pulsed-dose rate (PDR) irradiation can also be used for the delivery of ICBT. A 1 Ci (3.7×10^{10} Bq) ^{192}Ir source is used instead of a 10 Ci (3.7×10^{11} Bq) source as in the HDR system. The source leaves the remote afterloading unit for approximately 15 min per hour to deliver a 50 to 70 cGy “pulse”. PDR is a great alternative to LDR and HDR because it has some of the advantages of HDR irradiation while having similar radiobiological effect as LDR treatments (57-59). For example, the lower dose rate reduces the room shielding requirements compared to HDR. Also, since the sources are not inside the patient at all times, nurses and visitors can avoid

exposure to radiation by entering the room when the source is in the safe. Finally, the applicators used for PDR are identical to LDR and HDR applicators, which facilitate use for individuals who have familiarity with such applicators. From all the advantages of using PDR as discussed above, it is the preferred method of delivering ICBT here at MD Anderson Cancer Center.

The first guidelines for ICBT treatment planning were the Paris and Manchester methods (60). In an effort to standardize dose prescriptions and distribution, the International Commission on Radiation Units and Measurements (ICRU) released a report with recommendations on dose prescription and treatment techniques on ICBT in 1985 (61). Traditional points used in the Manchester system such as point A (the location where the uterine artery cross the ureter) and point B (location of obturator lymph nodes) were redefined. Additional points including bladder, rectal, and pelvic nodes were defined as well. Figure 2 shows the location of point A, B, bladder, and rectum. Nodal point definitions are explained in Section 1.2.4.

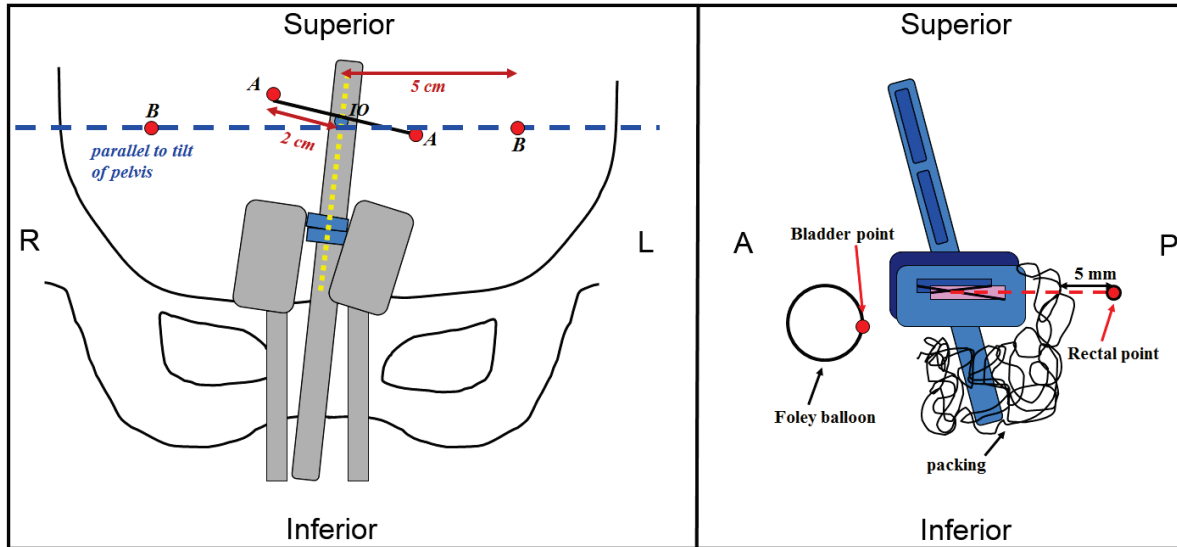


Figure 2: Locations of Point A, B, bladder and rectum as defined in ICRU 38. Point A is defined as the point 2 cm lateral to the central canal of the uterus and 2 cm up from the external os. Point B is defined as the point crossing the internal OS, parallel to the tilt of the pelvis, and 5 cm lateral from the midline. Bladder and rectum points can be identified on the lateral images. The bladder point is located on the most posterior surface point of the Foley balloon. The rectal point is located on a line drawn from the midpoint of the ovoids and 5 mm behind the posterior vaginal wall.

In recent years, with advances in imaging technology, ICBT treatment planning using volumetric modalities such as CT and magnetic resonance imaging (MRI) have gained popularity. One of the advantages of using 3-dimensional images such as CT and MRI instead of radiographs is much better assessment of the dose delivered to target and critical organs, since organs are visible with varying tissue contrast. Volumetric imaging provides information about the tumor, which allows anatomy based dose optimization and inverse planning. Dose delivered to normal tissues such as bladder and rectum can also be determined more accurately. Studies comparing ICRU organ points, which represent maximum dose in theory, with actual dose hotspots (D_{2cc}) determined using volumetric

images have shown varying discrepancy (62-64). In response to the increasing popularity of using CT or MRI during the ICBT process, the gynecology group of the Groupe Européen de Curiethérapie-European Society for Therapeutic Radiation and Oncology (GEC-ESTRO) published a set of recommendations for target volume delineation and treatment planning using 3-dimensional based treatment planning (65).

1.2.4 Boosting Radiation Dose to Positive Nodes

Lymph node involvement is a very important predictor of patient treatment outcome. Studies have shown that survival rates for patients with positive para-aortic nodes are approximately half compared to patients without para-aortic involvement with similar disease stage (66-69). Therefore, it is important to detect nodes positive for metastasis and prescribe the appropriate treatment course for patients. There are many methods to detect lymph node involvement. The most sensitive method is surgical with either transperitoneal lymphadenectomy or laparoscopic lymph node dissection. Although sensitive, surgical methods are highly invasive and may cause severe complications (70). Non-invasive imaging techniques such as CT and MRI can also be used to evaluate lymph node involvement. Large nodes with diameter greater than 1 to 1.5 cm could potentially suggest disease metastases but using nodal size alone can result in false positives since inflammation could also cause nodal enlargement. On the contrary, ¹⁸F-fluorodeoxyglucose positron emission tomography (FDG-PET) imaging, which measures metabolic activity, is very useful for detecting disease metastasis in the lymph nodes, with a sensitivity of 82% and specificity of 95% reported in literature (71-75). Kidd et al. found that using FDG-PET imaging for positive node detection

is comparable to historical data and correlates to patient recurrence and survival outcomes (76). Their results showed significant correlation between PET detected positive lymph nodes and prognosis (Fig. 3).

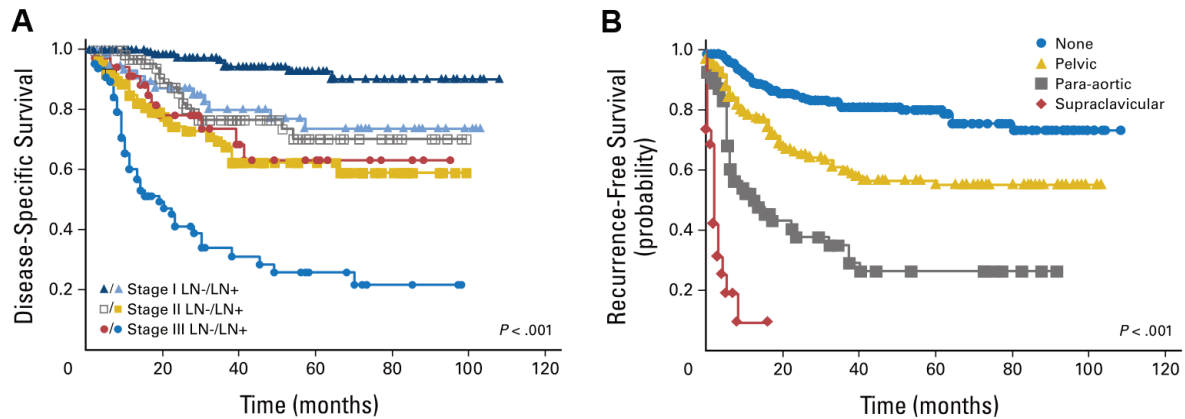


Figure 3: Kaplan-Meier disease-specific survival probability curves separated by (A) FIGO staging and (B) PET detected nodal involvement. (Kidd, E et al: J Clin Oncol Vol. 28, 2010: 2108-13. Reprinted with permission. © 2010 American Society of Clinical Oncology. All rights reserved.)

Although nodal involvement from cervical cancer may occur anywhere along the lymphatic drainage pathway, cervical cancer most commonly spreads to the external iliac nodes and common iliac nodes with lower percentage of spread further away from the primary site (77, 78). Typically, 45 to 50 Gy is adequate to control microscopic disease in the lymph nodes and delivered as part of the primary EBRT. Guidelines for delineation and field setup can be found in ICRU Report 38 (61). When nodal involvement is only in the pelvic region, nodes are included in the primary fields treating the central disease. Four-field 3D-CRT setup is used for extended para-aortic fields to reduce dose to small bowel and kidneys. In addition, recent studies have shown advantages of using IMRT for extended fields to

further reduce toxicity (32, 34). An example of an extended field EBRT treatment plan with all nodal regions treated can be seen in Figure 4.

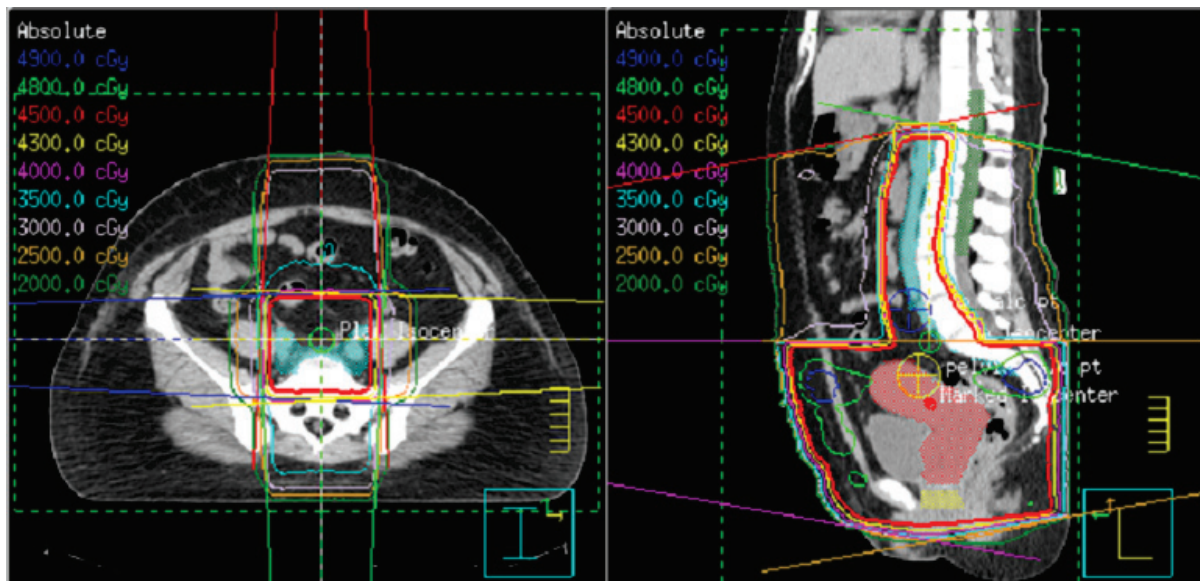


Figure 4: Example of extended field EBRT which includes primary disease, pelvic nodes, and para-aortic nodes. Two four-field 3D-CRT sets of beams matching at L5 were used.

In patients where gross lymphadenopathy is discovered, nodal regions are typically boosted to a total dose of 60 to 66 Gy (79). Prescribing dose for nodal boost is not straight forward. Although radiation oncologists know how much total dose the nodal region needs to receive, they must take into account dose contributions to the nodes from primary EBRT and ICBT. Determining dose contribution from primary EBRT is simple. Since it is part of the treatment planning target, the nodes receive full prescription homogeneous dose. Nodal dose contribution from ICBT is slightly more difficult to determine. When 2-dimensional radiographs are used for treatment planning, nodal structures cannot be seen since soft tissue contrast on x-ray films is minimal. Therefore, bony structures are used to estimate nodal

locations and dose. ICRU Report 38 recommends using the reference points on the lymphatic trapezoid of Fletcher, shown in Figure 5. When CT or MRI images are used for ICBT planning, positive nodal structures can be seen and delineated by radiation oncologists. The nodal dose contribution from ICBT is commonly described by taking the mean nodal dose of the entire volume. Because studies have shown strong correlation between longer treatment time and decrease in disease control (80-82), the optimal time to deliver nodal dose boost is during the two weeks of ICBT to prevent elongation of overall treatment duration. However, since nodal boosts are given prior to the second ICBT fraction, radiation oncologists must make the assumption that both ICBT fractions contribute equal dose to the nodes. Therefore, the equation used to calculate boost dose to positive nodes is:

$$\text{External Nodal Boost} = \text{Total Dose} - \text{Primary EBRT} - (\text{ICBT1} \times 2)$$

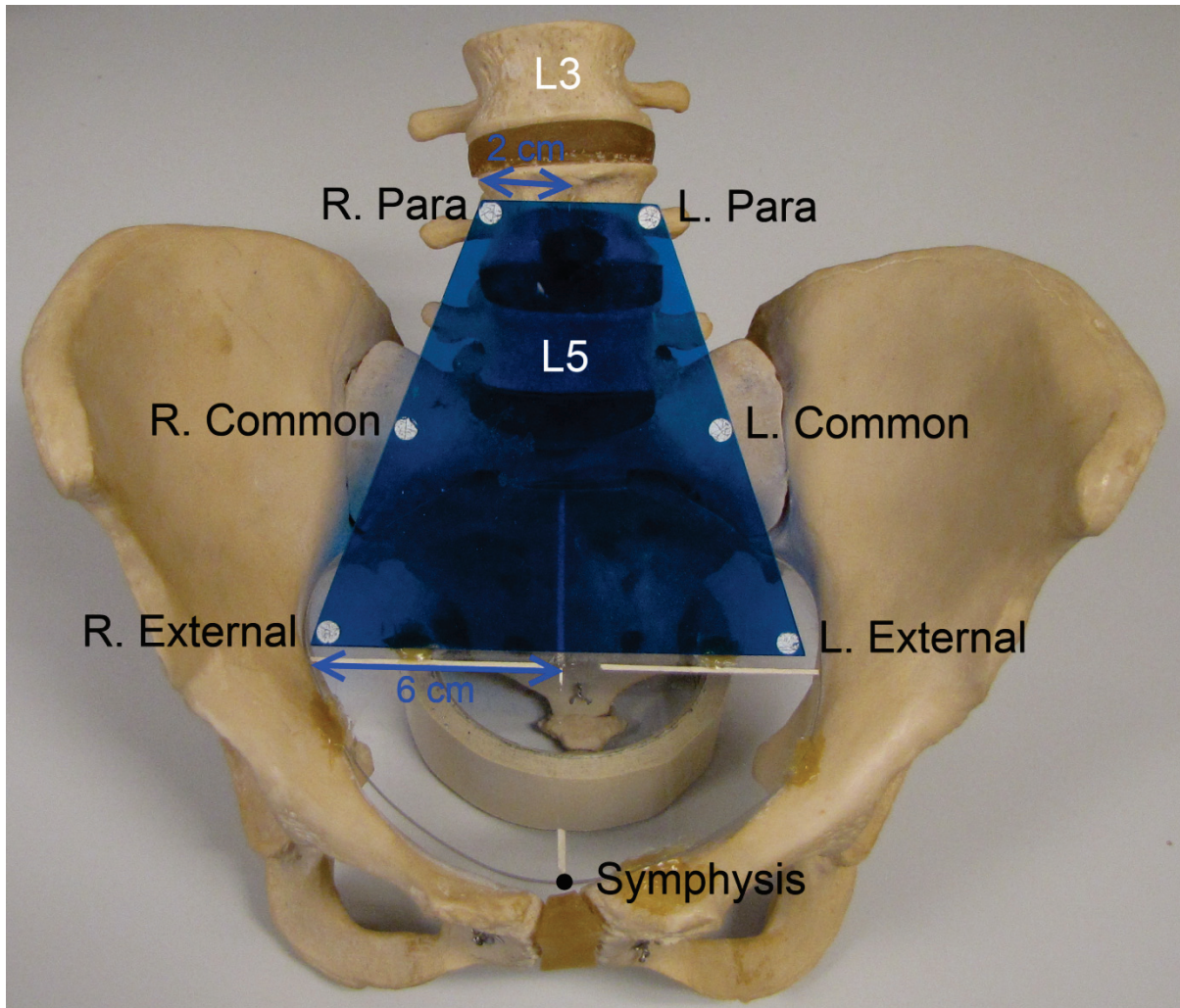


Figure 5: The lymphatic trapezoid of Fletcher as defined by ICRU Report 38 (61). Shows the method to determining external iliac, common iliac, and para-aortic nodal dose from x-ray films. The nodal points are based on bony locations since there is no soft tissue contrast on radiographs.

Pelvic nodal boost are normally boosted with small AP-PA opposing fields. Using such field setup allows the avoidance of bladder and rectum, and reduce the risk of ureteral stricture (83). However, any small bowel in the field will receive the full prescribed dose, as seen in Figure 6b. For the common iliac and para-aortic nodes, multifield 3D-CRT or IMRT is normally used to spare the anterior small bowel. Example of a para-aortic nodal boost is

shown in Figure 6a.

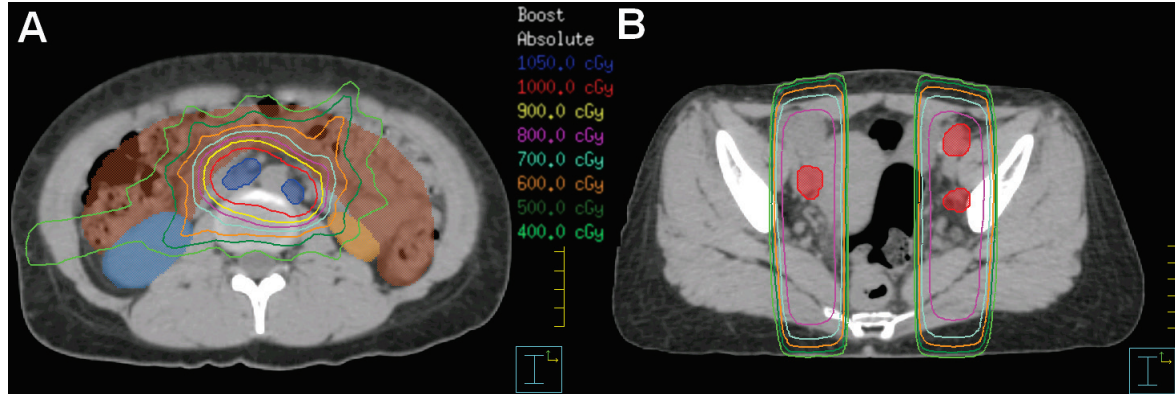


Figure 6: Example of beam setup and dose distribution for a patient receiving nodal boost in both para-aortic (A) and external iliac (B) nodal regions. Para-aortic nodes were planned and treated with 8-field IMRT while external iliac nodes are treated with two field AP-PA beams.

1.3 CURRENT OBSTACLES (AND POSSIBLE SOLUTIONS) IN HIGH PRECISION RADIATION

THERAPY OF CERVICAL CANCER

1.3.1 Motivation for this Project

Cervical cancer is one of the few anatomical sites where radiation therapy combines multiple courses from different modalities for curative intent. As Section 1.2.3 has shown, this is a complex process requiring external beam radiation therapy and brachytherapy to strongly complement each other. Although most researchers have focused on improving primary EBRT and ICBT, one aspect of cervical cancer treatment that has not been a focus of research is external beam nodal boost. As discussed in Section 1.2.4, disease detection and treatment in the nodal regions is extremely crucial to patients' survival probabilities. Even though not all patients require nodal boosts, the number of patients requiring nodal boost is

not negligible. Out of the 95 intact cervical cancer patients treated with primary EBRT and ICBT at MD Anderson in 2011, 46 (51%) received external beam boost to at least one nodal region. The motivation behind this project is to seek areas of potential improvement in boosting dose to lymph nodes and provide solutions.

1.3.2 Difficulty in Prescribing Nodal Boost

Because nodal boost dose is delivered prior to the second ICBT fraction, radiation oncologists must make assumptions about the second ICBT fraction prior to nodal boost dose prescription. In current practice, radiation oncologists assume that the first and second ICBT fractions contribute equal dose to the pelvic nodes. However, this assumption might not be accurate because the purpose of ICBT is to treat the primary tumor. Independent insertions of applicators can have many variations; tandem length and rotation, ovoid sizes, applicator locations in the pelvic, and dose distributions are just a few of the examples. In most situations, radiation oncologists make the attempt to remain as consistent as possible between the two ICBT fractions. In practice, this is difficult because patient anatomy could change dramatically between the two insertions. In cases where radiation oncologists suspect the nodal dose contribution from the second fraction will be lower, often due to shrinkage of primary tumor, conservative prescriptions methods are used for nodal boost to prevent underdosage. Such practice makes nodal dose prescription subjective and highly dependent on radiation oncologist experience. However, if variations in nodal dose between independent ICBT insertions are analyzed in an unbiased patient population, variations can be quantified and provide radiation oncologist with extra information when prescribing nodal boost dose.

Another difficulty in nodal boost dose prescription is caused by the increasing use of more conformal radiation therapy methods. Organ dose distributions from whole pelvis IMRT and inverse planning of ICBT are vastly different from 3D-CRT and brachytherapy dose distributions. Traditionally, understanding the total dose received by the normal organs such as bladder and rectum has been simple. During primary EBRT, the bladder and rectum essentially receive full prescription dose. During ICBT, bladder and rectum dose hotspots can be estimated using ICRU bladder and rectum points. Therefore, maximum dose to each organ can be estimated by summing the prescription EBRT dose and ICRU point dose from ICBT. Bladder and rectum dose distributions from conformal radiation therapy methods are much more heterogeneous. For example, hotspots and coldspots from inverse planned IMRT are much less predictable because of the large number of beams and leaf segments. Therefore, using traditional methods to quantify dose received by normal tissues may lead to inaccuracies. Since the hotspots from EBRT and ICBT might not be at the same location, traditional dose summation methods only represent the worst case scenario. One solution to this problem is by using deformable image registration (DIR) methods, which has the capability to locate locations of matching voxels on different images. Using DIR, dose summation can be performed volumetrically since the images are matched voxel-by-voxel. Better understanding of total normal tissue dose such as bladder and rectum is very important in prescribing nodal boost. Since normal tissue dose tolerances could be the limiting factors in nodal boost prescription, higher dose could potentially be prescribed when the actual 3D dose distributions are viewed instead of just the worst case scenario.

1.3.3 Rethinking How Nodal Boost Dose is Delivered

Currently, external radiation nodal boosts are delivered using photons. Since photon beams are attenuated exponentially after the build-up region, all tissues along the beam path receive some radiation. Therefore, regardless of the beam configuration, some normal tissue will receive a large amount of prescription dose. For example, although the bladder and rectum are avoided during external iliac nodal boost, as shown in Figure 6b, the small bowel receive essentially the full prescribed dose. An alternative method of delivering dose is by using protons. In proton therapy, the beam has finite range and delivers almost all of its energy at the end of its range (termed the Bragg peak). Clinically, this feature of protons is extremely advantageous because all organs beyond the distal edge of the beam can be spared. Contrary to photons, a single PA proton beam can be used to deliver conformal dose to external iliac nodes. Small bowel will be spared because it lies beyond the distal margin. However, the advantages of proton therapy are not without a cost. Proton beams are extremely sensitive to changes in the beam path. Uncertainty related to anatomical changes need to be considered thoroughly in order to use proton therapy to target the boost volume. Dosimetric differences caused by interfractional anatomical variations are magnified in nodal boosts because a very small target is irradiated over a small number of fractions. Variations in anatomy in the beam path can cause the proton beam edge to shift off the target, resulting in under-coverage in either the distal or proximal end of the target. In order for protons to be used in the clinic, adequate distal and proximal margins must be used during proton nodal boost planning to account for anatomical uncertainties.

1.4 ABOUT DISSERTATION

1.4.1 Purpose and Hypothesis

The purpose of this project is to improve external beam radiation therapy of lymphatic nodal boost during a course of cervical cancer treatment by: 1) Quantifying interfractional uncertainties. 2) Developing and validating dose accumulation tools between external beam radiation therapy and brachytherapy. 3) Exploring alternative treatment modalities.

The hypothesis of this project is separated into three parts. First, rigid 2D-3D image alignment between films and CT images can be used to quantify nodal dose differences from independent ICBT insertions. Second, deformable image registration can be used to sum normal tissue dose from EBRT and ICBT. Third, ray-tracing methods can be used to determine interfractional anatomical variation margin requirements for proton therapy of nodal boost.

1.4.2 Specific Aims

There are three specific aims to this project, which are used to address the purpose and validate the hypothesis. The aims are listed below:

1. Quantify variations in pelvic nodal dose due to applicator placement during a multi-fraction ICBT course.
2. Develop and validate deformable image registration methods for the use of volumetric summation of bladder and rectum dose from ICBT to an external beam planning CT image set.

3. Calculate nodal boost planning margins needed for proton therapy to account for interfractional anatomical variations.

1.4.3 Organization of Dissertation

This dissertation is separated into five chapters. The first chapter is used to provide the necessary background information to the issues and problems that are being tackled in this project. The next three chapters provide details on the methods used to address each specific aim and their respective results. Extra background relating to the tools and method in each specific aim are provided in the middle chapters as well. The final chapter is where all the results are brought together. It is where we look at the big picture and anticipate the impact of the findings in this project, discuss how results can be implemented in clinical practice, and identify future work that could be done to improve upon current findings.

Chapter 2: Variability in Pelvic Nodal Dose between Independent Intracavitary Brachytherapy Fractions for Treatment of Cervical Cancer

2.1 SPECIFIC AIM 1

Quantify variations in pelvic nodal dose due to applicator placement during a multi-fraction ICBT course.

2.2 INTRODUCTION

In patients with involved lymph nodes, which are often identified by PET and/or biopsy, additional radiation following primary pelvic radiation therapy is delivered to bring the total lymph node dose to 60 – 66 Gy range (79). Because brachytherapy can contribute a significant dose to pelvic lymph nodes, it needs to be taken into account when determining the appropriate final boost dose. At MD Anderson, the external beam boost to involved lymph nodes is given before the completion of ICBT. Therefore, assumptions about the boost to positive lymph nodes for future implants are made to determine the lymph node boost dose.

As discussed in Section 1.3.2, in current practice, radiation oncologists assume that the first and second ICBT fractions contribute equal doses to the pelvic nodes. However, this assumption might not be accurate since independent insertions of applicators can vary with respect to many factors: tandem length and rotation, ovoid size, applicator location in the pelvis, and dose distributions (84-86), which may all contribute to the variation in node doses. The purpose of this specific aim was to quantify differences in nodal dose between

independent ICBT fractions due to applicator placement between ICBT fractions.

Correlations between dose variations and external factors such as tandem angle rotation and applicator system placement were evaluated as well.

2.3 METHODS AND MATERIALS

2.3.1 Patient Cohort

The MD Anderson Cancer Center Institutional Review Board approved this retrospective study. Ten patients with intact cervical cancer and positive nodes which required nodal boost were selected for this study. The patients had clinical stage IIA to IIB cervical cancer and were treated between August 2008 and December 2010. All patients received primary EBRT delivered in 1.8-Gy fractions to a total dose of 45 Gy. Two fractions of PDR ICBT were delivered immediately after EBRT at approximately 20-Gy per fraction prescribed to Point A. Delivery duration for each ICBT fraction was 44 hours, and the two fractions were spaced 2 weeks apart. ICBT was delivered using Fletcher-Suit-Delclos tandem and ovoid applicators with ovoid sizes ranging from small (20-mm dia.) to medium (25-mm dia.). ICBT planning was performed using orthogonal radiographic films obtained after applicator insertion in the operating room. All patients also had PET-positive pelvic nodes that were treated with a boost to a mean total dose of 62.1 Gy (range 60 Gy – 66 Gy). All patients underwent two CT simulations, one before primary EBRT and one before delivery of the nodal boost. Positive nodes were delineated on the CT scans by the radiation oncologist.

2.3.2 Aligning ICBT Film Images and 3D Dose to EBRT CT Image Sets

Since CT images at the time of ICBT were not available for all patients, we had to devise a method to determine spatial correlation between film and CT images and then transfer the ICBT dose from the film images to the CT images. Figure 7 provides a schematic of the methodology that was used; the details of which are presented below. Original ICBT planning for all patients was performed by dosimetrists and approved by radiation oncologists. AP and lateral films used for planning were obtained in the operating room immediately after applicator insertion. In this work, original clinical plans were done in the Plato treatment planning system (TPS) v. 14.3.7 (Nucletron, Netherlands) and replicated using the Oncentra TPS v. 4.0 (Nucletron, Netherlands) with dwell positions identical to those in the original clinical plans. Dwell times on the replicated plans were adjusted to account for differences in the activity of the current radioactive source and the activity of the source used at the time of treatment. Dose calculations were performed using guidelines provided by the American Association of Physicists in Medicine Radiation Therapy Committee Task Group #43 (87, 88). Unlike its predecessor, Plato, the Oncentra TPS allows calculation of the dose in three-dimensional space, which we calculated using a dose grid of $30 \times 30 \times 40 \text{ cm}^3$ with a voxel size of $2 \times 2 \times 2 \text{ mm}^3$ centered at the internal os. International Commission on Radiation Units and Measurements (ICRU) point A (left+right), as defined in Section 1.2.3, was placed on the replicated plans as a method to verify the accuracy of the replication process. The plans were then exported as DICOM files, which contained DICOM images of the AP and lateral films along with the DICOM-dose file. Since each patient had two ICBT fractions, 20 replica treatment plans were done.

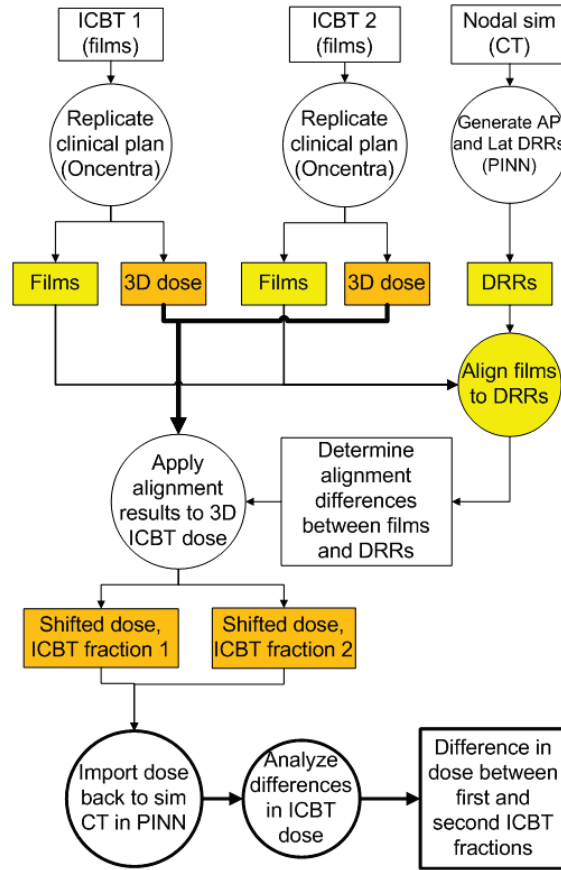


Figure 7: Schematic of the procedure to determine differences in nodal dose between independent intracavitary brachytherapy (ICBT) fractions. First, films from ICBT fractions 1 and 2 (ICBT 1 and ICBT 2) were aligned to the computed tomography (CT) image set from treatment simulation (sim) performed before delivery of the nodal boost. Specifically, the original ICBT clinical plans were replicated using an Oncentra treatment planning system with dwell positions identical to those in the original clinical plans, and dose calculations were performed using guidelines provided by the American Association of Physicists in Medicine Radiation Therapy Committee Task Group 43 (87, 88). To permit alignment of ICBT film images to CT images, digitally reconstructed radiographs (DRRs) were generated from CT images in the anterior-posterior (AP) and lateral (Lat) directions. The replicated ICBT films and the DRRs were then aligned using a published algorithm (89). The alignment result was used to shift the ICBT dose into the CT coordinate system to obtain shifted doses for the first and second ICBT fractions, and these doses were imported into a Pinnacle (PINN) treatment planning system. Finally, differences in dose were analyzed volumetrically.

Because we are aware of no commercial tools that can align two-dimensional film images to three-dimensional CT image sets and can transfer dose from film plans to CT images, in-house software using MATLAB v. 7.12.0 (The MathWorks, Inc, Natick, MA) was generated to achieve the desired task. To align ICBT film images to external beam planning CT images, digitally reconstructed radiographs (DRRs) were first generated from CT images in the AP and lateral directions. These DRRs were then exported and aligned with their respective film counterparts. This is possible because although film images are two-dimensional, orthogonal films with a common reference point can provide three-dimensional information. Aligning two sets of orthogonal two-dimensional radiographs can provide offsets in the x, y, and z directions.

To align the ICBT films and DRRs, rectangular regions with identical dimensions encompassing the nodal region of interest and surrounding bony anatomy were first drawn on both the films and DRR image sets to localize the area used for alignment. Global image registration was not used because it is more critical to align the region closest to the nodes correctly than to have the entire pelvic and lumbar region aligned reasonably well. Because contrast on radiographs is greatest between bone and soft tissue, pelvic and lumbar bony anatomy within the rectangular regions delineated on the films and DRR image sets were aligned automatically using cross-correlation algorithm developed by Guizar-Sicairos et al. (89) and modified for this project. The algorithm uses rigid image registration that allows three degrees of freedom: translation in the AP, SI, and RL axes. Some of the modifications such as two secondary checks of alignment accuracy were also developed to facilitate use of the software. The first displays graticules centered at the isocenter on both film and DRR

images. The second overlays film and DRR images and displays each using 50% visibility or a checkerboard of alternating images. When auto-alignment results were inadequate or appeared incorrect, because of either bad image quality or lack of information, secondary alignment methods were used and results were adjusted manually. Manual alignment also allowed for rotations, i.e., pitch, yaw, and roll, of the film images to provide more accurate alignment. An example screen capture of the graphical user interface of the in-house software is shown in Figure 8.

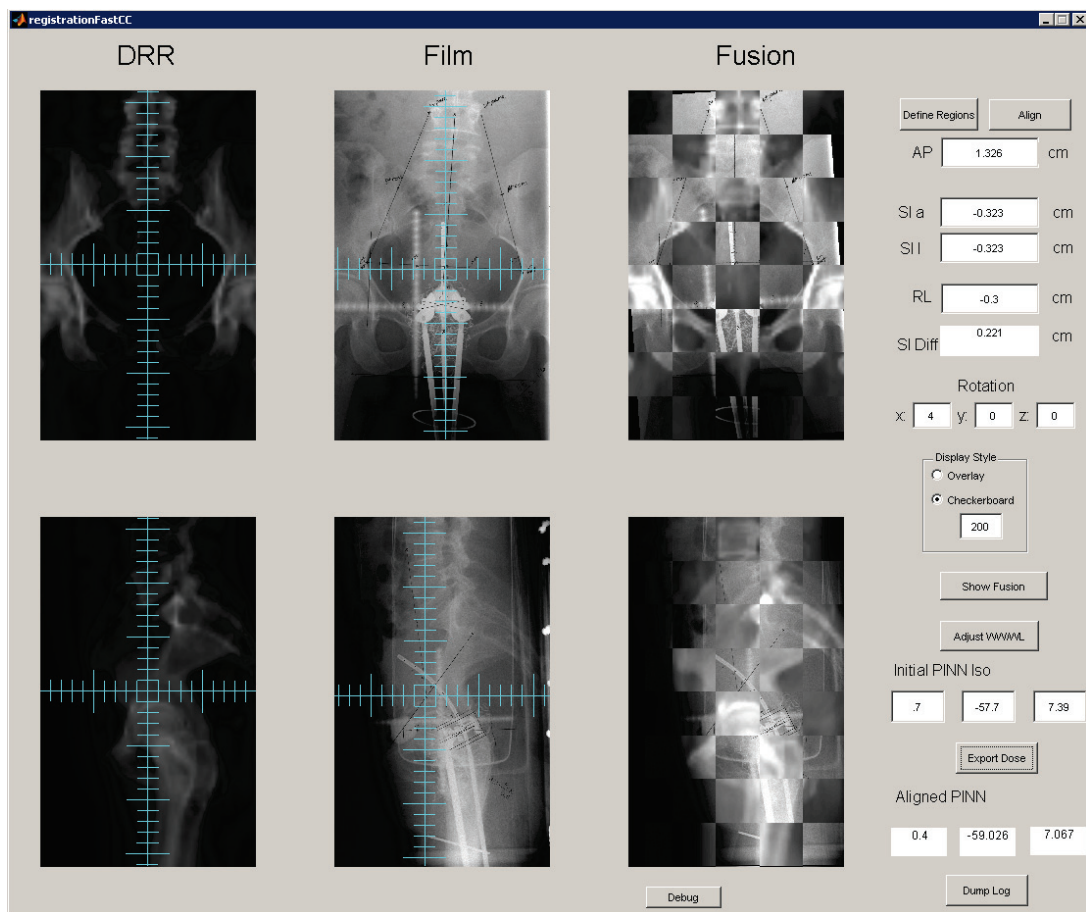


Figure 8: User interface created in-house using MATLAB for aligning digitally reconstructed radiographs (DRRs) and film images. Auto-alignment results can be verified manually by using the graticules and fusion display.

To validate the accuracy of our automatic image registration algorithm, a reference DRR image set and eight shifted DRR image sets with known shifts were created from a single CT image set, as shown in Figure 9. The shifted DRR image sets were created by shifting the reference DRR isocenter ± 2 cm, ± 3 cm, and ± 4 cm in the RL, AP, and SI directions, respectively. Large shifts were chosen to test the robustness of the alignment method. Using our alignment software, shifted DRRs were treated as simulated ICBT film images and aligned to the reference DRR images. Without any manual intervention, the shifts calculated by the alignment software were compared to the known shifts of the isocenters. Differences in shifts were recorded.

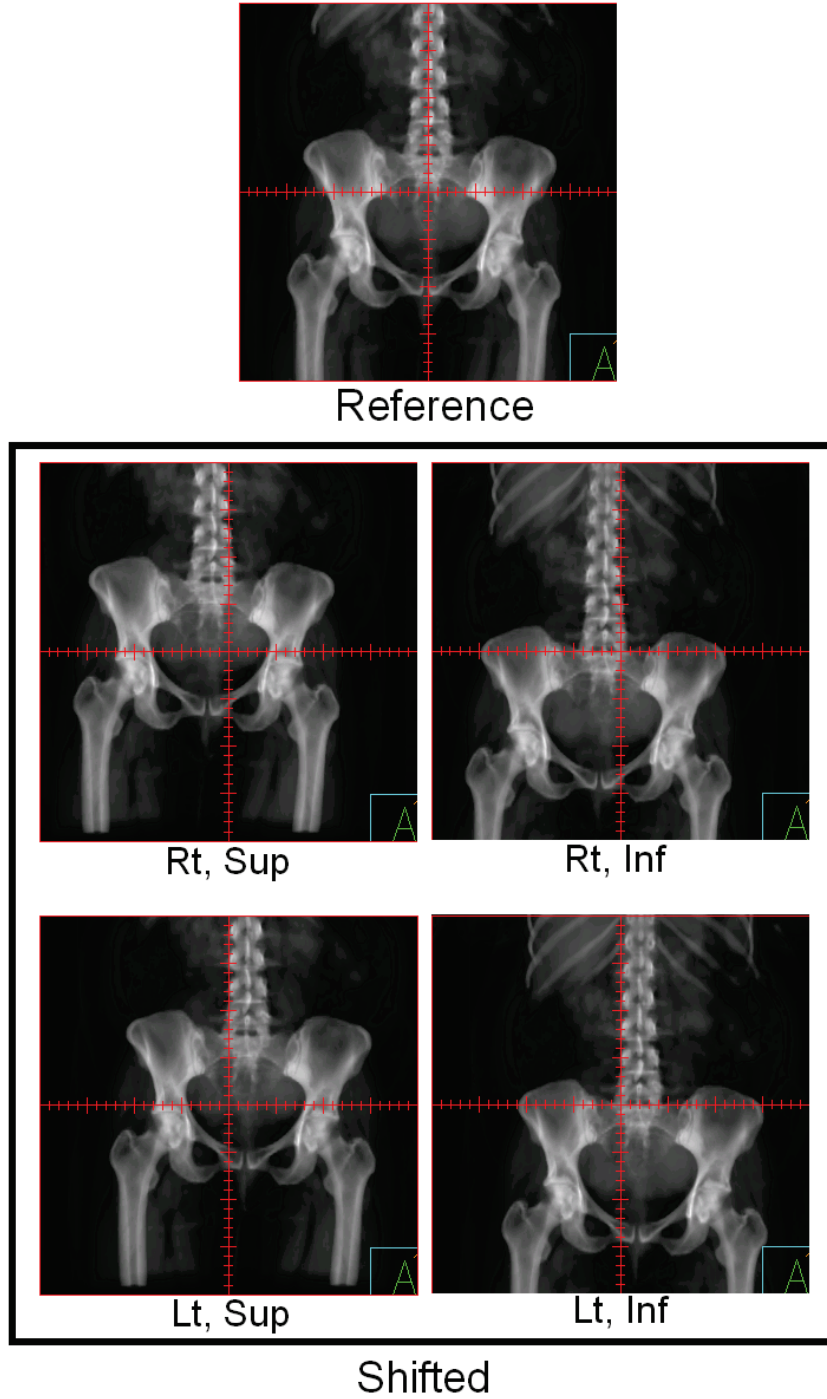


Figure 9: Reference DRR and 4 out of the 8 shifted DRRs used for validation testing of our rigid alignment algorithm. Only shifts in the LR and SI direction are shown in figure.

To link the ICBT three-dimensional dose to external beam planning CT images, we needed to know the spatial association between the ICBT dose grid, film images, and external beam planning CT images. The center of the ICBT dose grid is also the planning isocenter, which was defined at the internal os during treatment planning. Prior to image registration, the ICBT film images were cropped so that the internal os was at the center of the image, which made the center of the images and the dose grid identical. Differences in film and DRR isocenter, obtained from our image registration software, were then used to calculate the location of the film isocenter on the CT image set. Once we identified the location of the film isocenter on the CT image sets, the exported DICOM-dose files from Oncentra were converted to Pinnacle (Philips Medical Systems, Andover, MA) dose format, rotated and shifted to the correct isocenter location, and imported into Pinnacle using in-house-developed software tools.

2.3.3 Analyzing Nodal Dose Differences between Independent ICBT Fractions

The Pinnacle TPS is limited in dose-manipulation such as voxel-by-voxel dose accumulation and cumulative dose-volume histogram analysis. Therefore, to analyze differences in nodal dose between two independent ICBT fractions, a three-dimensional binary mask of all the positive nodes and their doses was exported from Pinnacle to be analyzed using another in-house MATLAB program. Since dose and CT voxel sizes are not the same, dose grids were then resampled to obtain the same resolution as the CT image set. With the binary mask and dose having an identical resolution, we were able to extract dose within the structures of interest to be evaluated or manipulated. Differences in nodal dose

contribution between the first (ICBT1) and second (ICBT2) insertions in terms of mean dose and D_{90} (the dose received by at least 90% of the volume) were calculated.

Calculating differences in nodal dose between independent ICBT fractions does not explain the source of the variations. We wanted to quantify and correlate factors that cause these dose differences. To eliminate differences caused by dose prescription, we calculated the ratio between the average ICRU point-A doses from the first and second ICBT fractions and multiplied the dose from the second ICBT fraction by this ratio. This normalized the dose of the second fraction, such that its dose prescription was identical to that of the first fraction. After dose normalization, tandem angle and length variations and system location shifts were analyzed. Tandem angle variations were determined by measuring the separation in angle between the tandem and midline of the pelvis, as shown in Figure 10. Tandem length variations were calculated by measuring the length of tandem from the tip to the internal os. System location variations were determined by comparing the differences in internal os location within the pelvis on the CT image set between the first and second ICBT fractions in RL, AP, and SI directions. The total magnitude of system location shift was calculated by taking the root of the sum of squares in the three directions. Figure 11 shows differences in isocenter location between the two ICBT fractions. Two-tailed Spearman's rho correlation tests were used to determine whether correlations existed between tandem angle, system location, and variations in nodal dose.

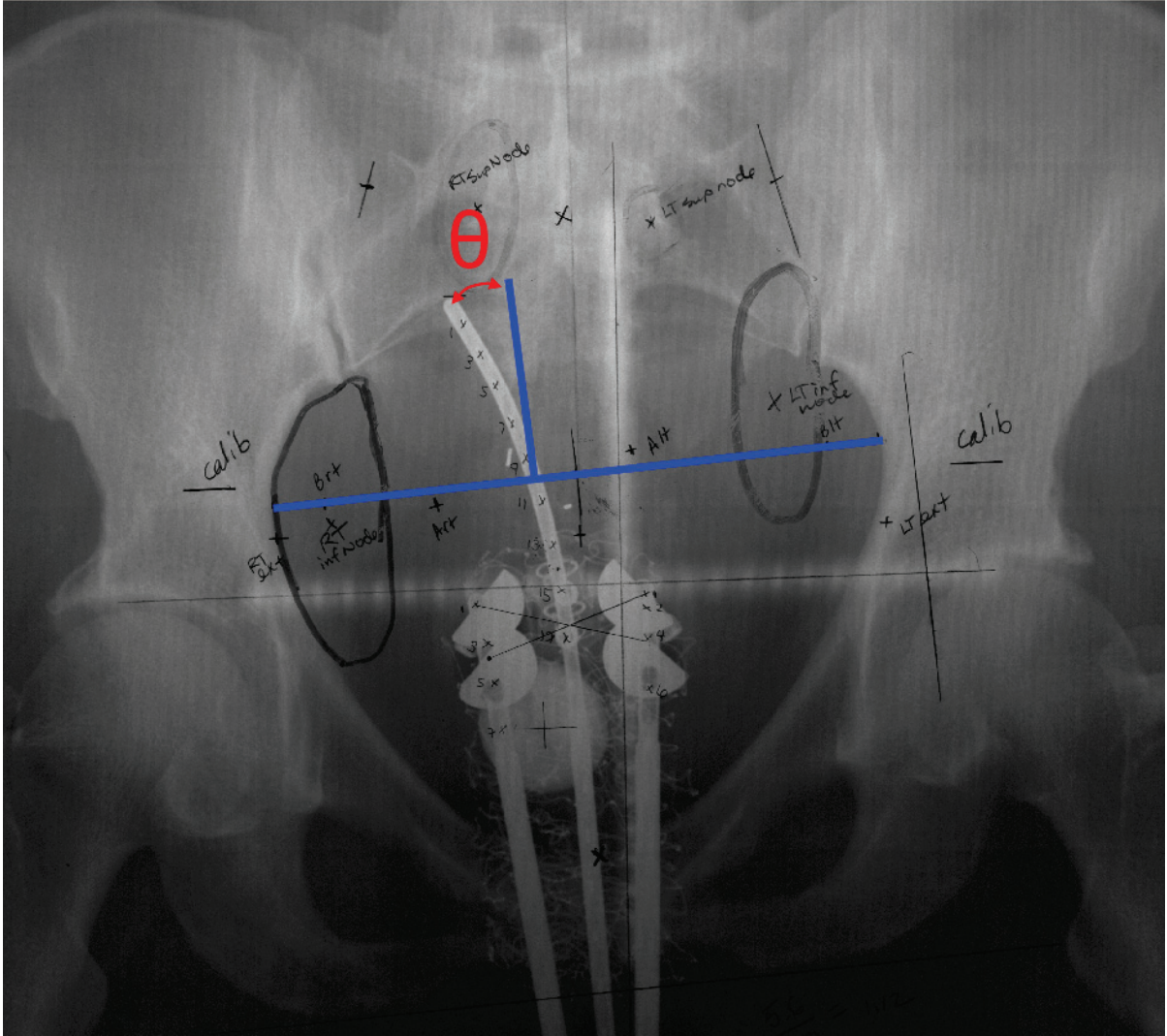


Figure 10: Tandem angle (θ) was determined by measuring the separation in angle between the tandem and midline of the pelvis.

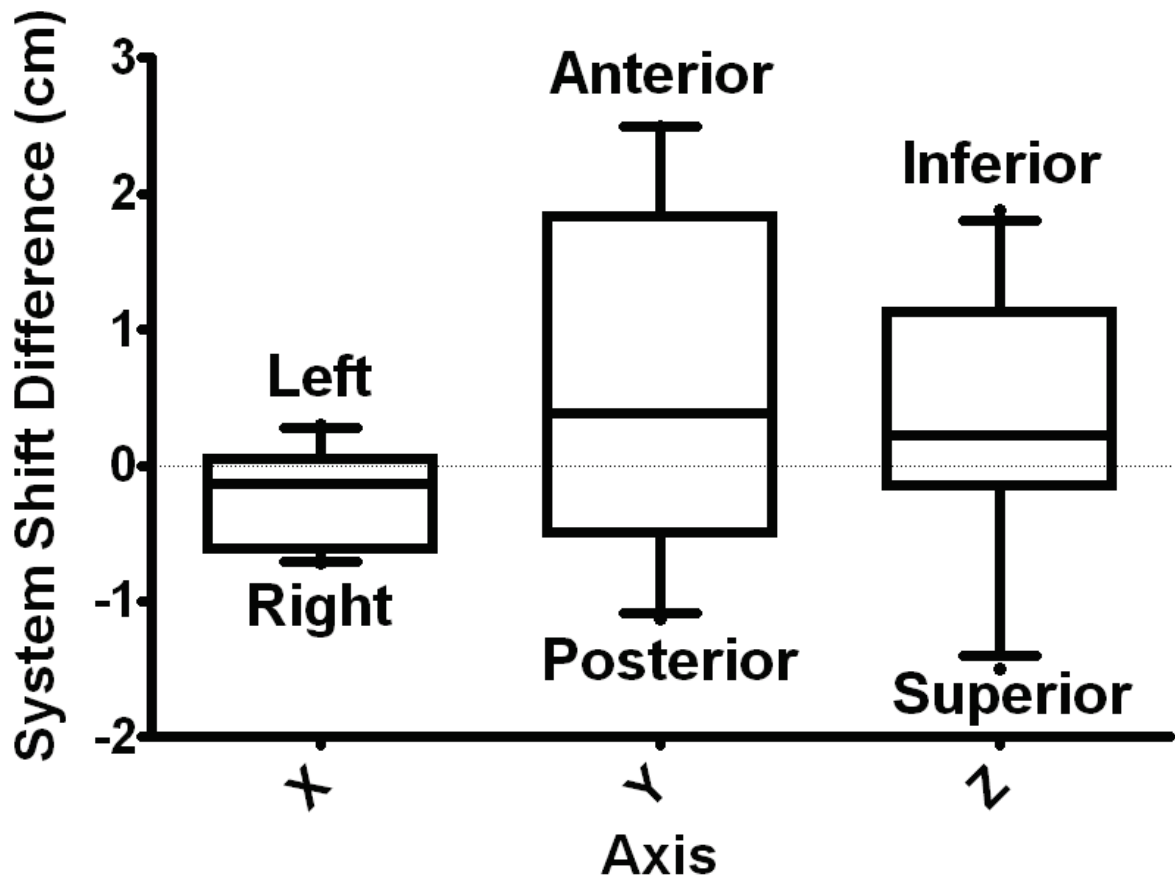


Figure 11: Differences in system shifts between the first and second intracavitary brachytherapy fractions. Variation was smallest in the lateral direction, while most variation occurred in the anterior-posterior direction. Most shifts between the first and second fractions were in the anterior and inferior direction. Box graphs show 25th percentile, median, 75th percentile, and outliers for variations in each axis.

2.4 RESULTS

2.4.1 Validation of Image Registration Algorithm

Validation results of the automatic image registration algorithm used in this study is shown in Table 1. The mean discrepancies between the calculated and known shifts were

0.78 mm, 0.8 mm, and 1.14 mm in the RL, AP, and SI directions, respectively. Maximum discrepancies between the calculated and known shifts were 1.25 mm, 1.88 mm, and 2.5 mm in the RL, AP, and SI directions, respectively.

Table 1: Results for auto-alignment algorithm. A reference DRR image set was first generated using isocenter near the center of the pelvis. Shifted-DRR image set were generated by shifting the isocenter ± 2 cm, ± 3 cm, ± 4 cm in the LR, AP, and SI directions, respectively.

Shifted-DRR image set (isocenter shift)	Difference (mm)		
	RL	AP	SI
2 cm left			
3 cm anterior	1.25	1.88	2.11
4 cm inferior			
2 cm left			
3 cm anterior	1.25	1.09	1.33
4 cm superior			
2 cm left			
3 cm posterior	0.31	0.47	2.50
4 cm inferior			
2 cm left			
3 cm posterior	0.31	0.47	0.16
4 cm superior			
2 cm right			
3 cm anterior	1.25	0.47	0.94
4 cm inferior			
2 cm right			
3 cm anterior	1.25	0.47	1.72
4 cm superior			
2 cm right			
3 cm posterior	0.31	0.47	0.23
4 cm inferior			
2 cm right			
3 cm posterior	0.31	1.09	0.16
4 cm superior			
Mean	0.78	0.80	1.14
Max	1.25	1.88	2.50

2.4.2 Nodal Dose Differences from Independent ICBT Fractions

For analysis of differences in patient nodal dose between the first and second ICBT fractions, nodes were divided into two regions, distal pelvic and proximal pelvic, with respect to location of central disease. The distal pelvic region included common iliac lymph nodes, and the proximal pelvic region contained external, internal, and obturator lymph nodes. Of the 10 patients, 6 had PET-positive distal and proximal pelvic nodes, 3 had PET-positive proximal pelvic nodes only, and 1 had PET-positive distal pelvic nodes only. All nine patients with positive proximal pelvic nodes had bilateral positive nodes. Of the seven patients with positive distal pelvic nodes, five had multiple positive distal pelvic nodes, and two had a single positive distal pelvic node. Together, the 10 patients in the study had 20 positive proximal pelvic nodes and 14 positive distal pelvic nodes. Approximate locations of all nodal centroids, or geometric center, as calculated by Pinnacle TPS are show in Figure 12.

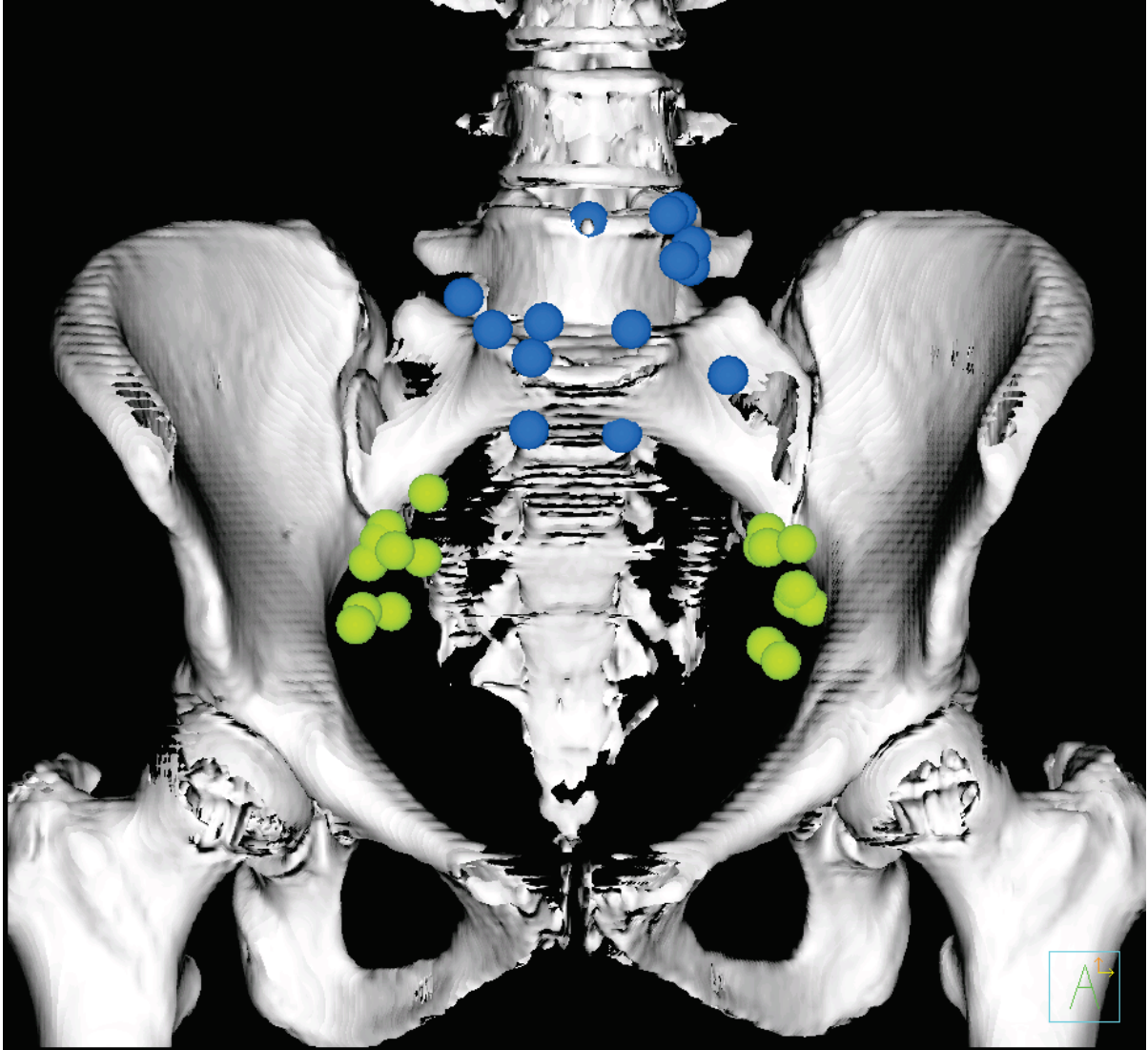


Figure 12: Approximate centroid locations of all analyzed nodes for all patients displayed on an atlas computed tomography image. The blue and green spheres represent nodes in the distal and proximal pelvic regions, respectively.

Differences in nodal dose contributions between the ICBT1 and the ICBT2 are shown in Figure 13. Positive and negative nodal dose differences between the two ICBT fractions means higher and lower ICBT dose from the second fraction, respectively. For the proximal and distal pelvic nodal regions, the mean \pm 1SD (range) differences between the ICBT1 and

ICBT2 mean nodal dose were 8.6 ± 85.1 (-134.5 to 192.8) cGy and -46.8 ± 55.3 (-172.7 to 20.0) cGy, respectively. The 10th-percentile, 90th-percentile, and median differences between ICBT1 and ICBT2 mean nodal dose were -92.8 cGy, 134.1 cGy, and 8.9 cGy, respectively, in the proximal pelvic region and -143.4 cGy, 14.1 cGy, and -18.86 cGy, respectively, in the distal pelvic region. Mean differences between ICBT1 and ICBT2 D_{90} for proximal and distal pelvic nodal regions were 5.2 ± 69.8 (-110.6 to 145.2) cGy and -21.9 ± 38.4 (-84.6 to 46.9) cGy, respectively. The 10th-percentile, 90th-percentile, and median differences between ICBT1 and ICBT2 D_{90} were -82.4 cGy, 109.1 cGy, and 0.9 cGy, respectively, in the proximal pelvic region and -83.9 cGy, 30.3 cGy, and -10.5 cGy, respectively, in the distal pelvic region.

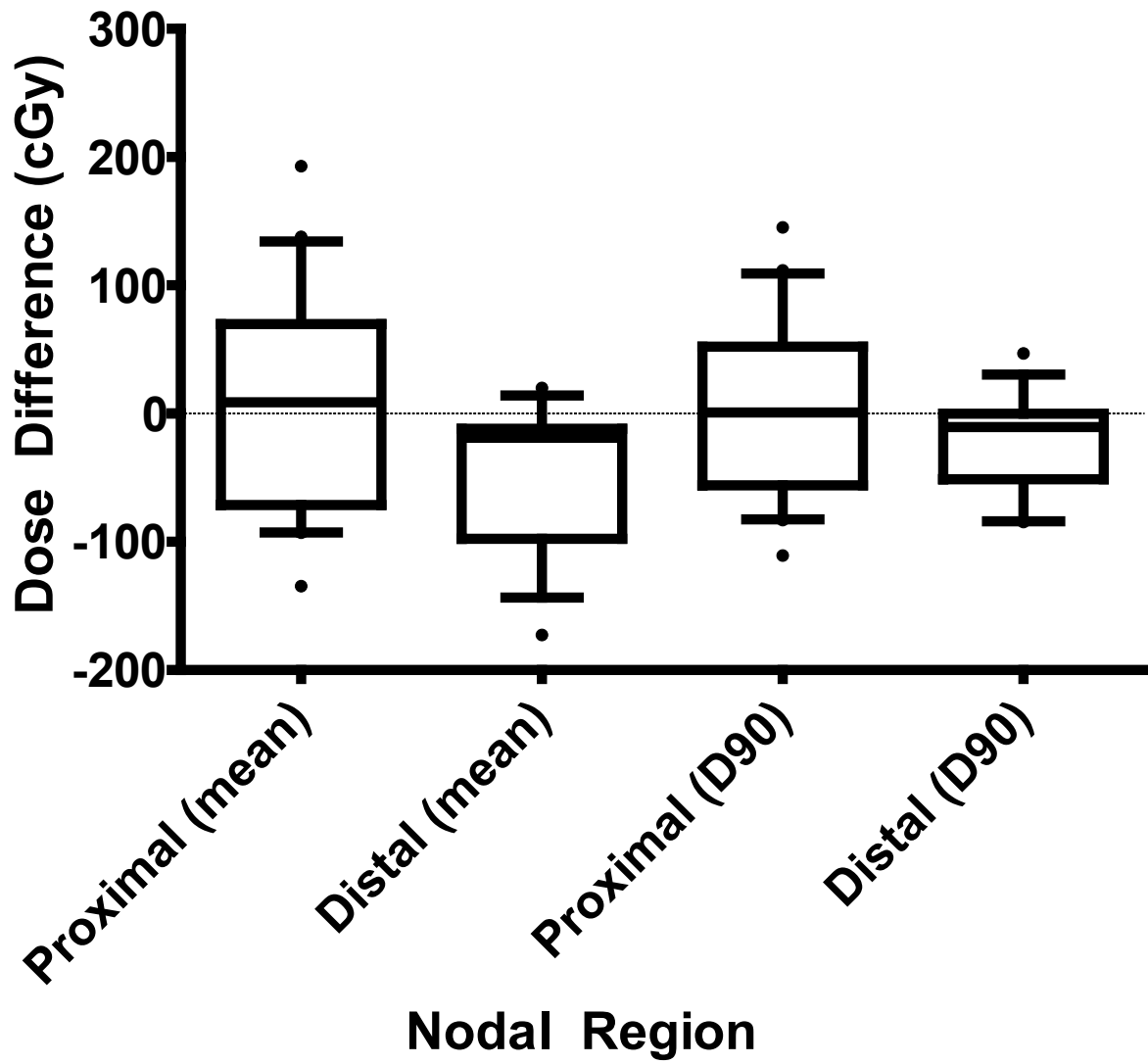


Figure 13: Differences between the expected and delivered nodal dose from intracavitary brachytherapy for the proximal and distal pelvic regions. Box graphs show 25th percentile, median, 75th percentile, and outliers for both the mean nodal dose and the dose received by at least 90% of the nodal volume (D_{90}).

2.4.3 Correlation between Tandem and Applicator Location Variations and Nodal Dose Difference

Two-tailed Spearman's rho correlation tests were performed between tandem angle and length variations, applicator system location variations in the RL, AP, SI directions, total magnitude of applicator system shift, and normalized nodal dose differences from independent ICBT fractions. Proximal pelvic node dose was affected by AP and lateral shifts in applicator placement. Distal pelvic nodes were impacted by tandem angle and total magnitude of applicator shift. Also, with the exception of one node, anterior shifts increased pelvic node doses, while posterior shifts decreased node doses. Plots for all significant pairs are shown in Figure 14.

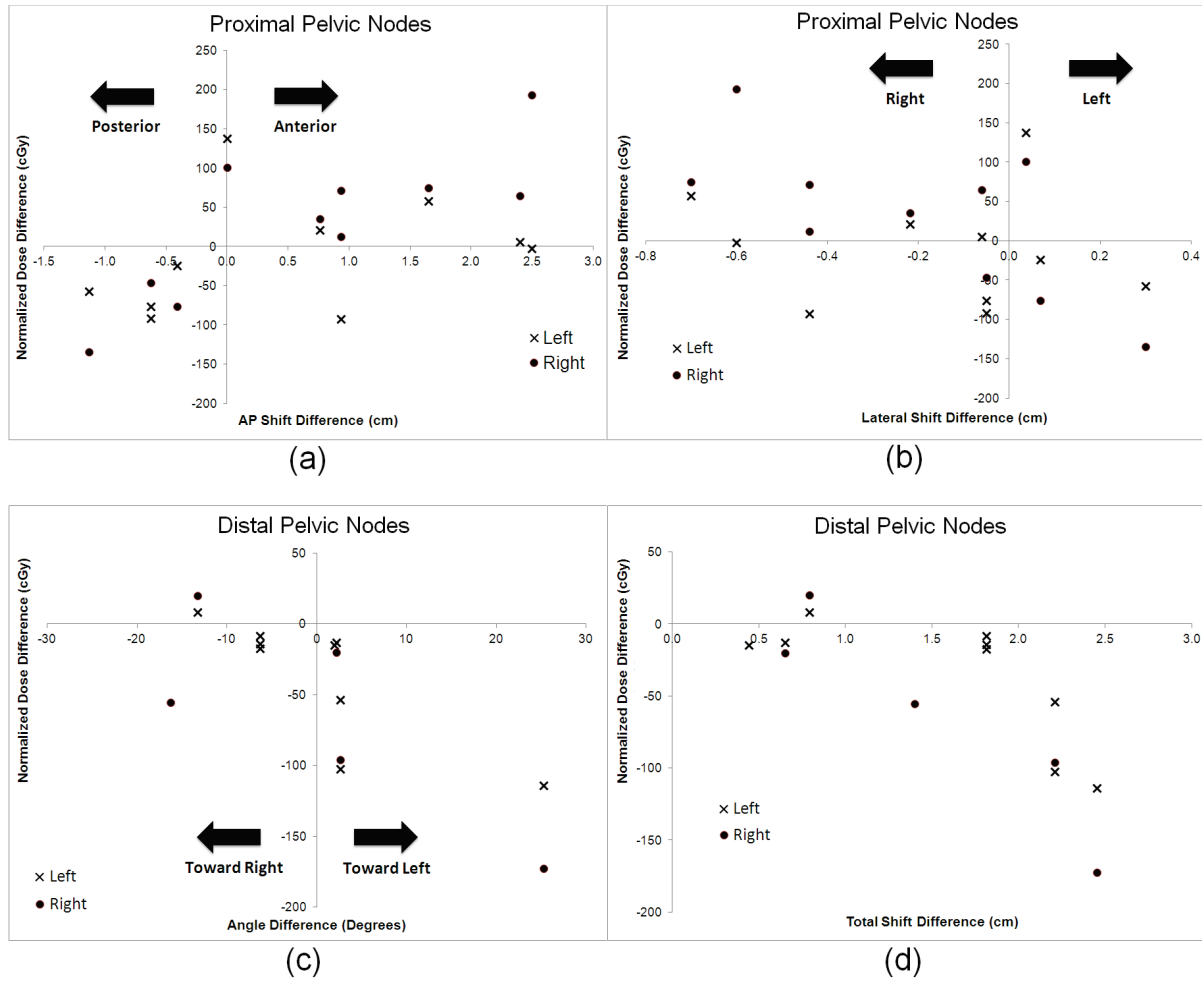


Figure 14: Graphs of normalized dose differences for pelvic nodes between the first and second intracavitary brachytherapy (ICBT) fractions versus applicator changes between the first and second ICBT fractions for relationships with significant correlations ($p < 0.05$).

2.5 DISCUSSION

To the best of our knowledge, difference in pelvic nodal dose from different ICBT fractions has not been explored previously. Results from this work show that the absolute difference in mean node dose from independent implants can be as high as 1.9 Gy and 1.7 Gy

in proximal and distal pelvic nodes, respectively. However, only 20 percent of proximal and 21 percent of distal mean nodal dose absolute differences were greater than 1 Gy.

To achieve this study objective, we developed an in-house software with the capacity to utilize exported DICOM images and dose files from the Oncentra TPS, align the two-dimensional film images with CT image sets from EBRT, and import corrected brachytherapy dose onto the CT image. The results from validation of our auto-alignment algorithm showed that on average, the registration error was small. In the RL and AP directions, the average difference was less than 1 mm, while it was slightly more than 1 mm in the SI direction. The worst registration errors in the RL, AP, and SI directions were 1.25 mm, 1.88 mm, and 2.50 mm, respectively. This is not surprising because registration accuracies are highly dependent on image resolution and the CT image set used for testing had 1.2-mm resolution in the RL and AP directions and 2.5-mm resolution in the SI direction. Therefore, in the worst-case scenario, differences resulted from misalignments is approximately 1 pixel. Also, although the DRRs were generated from the same CT image set, there are still differences because shifting isocenter and regenerating DRR images is not equivalent to shifting the center and cropping the reference DRR images. DRRs are generated by projecting a point source through the CT image. By shifting the isocenter, we essentially shifted the point source and generated new images from the new reference point. Therefore, regenerated DRR images are not identical, especially for pixels that are further from the isocenter.

2.5.1 Nodal Dose Variations in the Proximal Pelvic Region

In the proximal pelvic region, the mean difference between the ICRT1 and ICRT2 mean nodal dose was 8.6 cGy, such difference is negligible. This indicates equal probability for the second ICBT fraction to contribute lesser or greater dose than the first ICBT fraction. However, the 1SD in dose difference for proximal pelvic nodes was almost 1 Gy with maximum absolute difference being 1.93 Gy. Spearman's rho two-tailed tests indicated that the difference in proximal pelvic nodal dose was significantly correlated with shifts in the applicator system in the RL and AP directions ($p < 0.05$). This is not unexpected because dose distribution directly follows the applicator placement and any shifts in the axial plane would move the distribution either closer to or further from the nodal region of interest. Figure 14a shows that in general, the contribution to nodal dose from the second ICBT fraction increased when the applicator system moved anteriorly and decreased when the applicator system moved posteriorly. This occurred because applicator placement is normally posterior to the proximal pelvic nodes and if the applicator is moved more anteriorly, the higher-dose region will be closer to the nodes and cause an increase in nodal dose. Figure 14b shows that in general, when the applicator system was shifted laterally, dose to the nodes on the side of the shift increased. Differences in nodal dose are always caused by a combination of factors, and there are always exceptions to the rule. For example, from Figure 14b, one of the proximal pelvic nodes on the left side of the patient decreased in dose when the applicator system is shifted to the left side by 3-mm. However, for the same patient, the system shift also moved posterior in the second ICBT fraction, by 1.1-cm, thus causing decrease in proximal pelvic nodal dose.

Another factor which would result in differences in pelvic node doses between the first and second ICBT fraction is ovoid size. In theory, changes in ovoid size would result in dose distribution variations, which potentially can lead to dose changes to the proximal pelvic nodes. However, in the patient cohort used in this study, only one of the ovoids used in a single ICBT fraction was medium sized. Since all remaining ovoids were small, no conclusion can be made about nodal dose differences caused by ovoid size changes.

2.5.2 Nodal Dose Variations in the Distal Pelvic Region

Compared to the proximal pelvic nodes, the distal pelvic nodes had a more negative mean difference in mean nodal dose (-46.8 cGy) and a smaller 1SD (55.3 cGy). This shows that the dose contribution to the distal pelvic nodes was almost always lower during the second ICBT fraction. This could potentially be caused by tumor shrinkage between the first and second ICBT fractions, necessitating a more conformal dose distribution. Correlation tests showed that the difference in distal pelvic nodal dose was significantly correlated ($p < 0.01$) with tandem angle and the total magnitude of the applicator system shift. Plotting tandem angle versus dose change (Figure 14c), we see that with the exception of one patient, dose decreased when tandem angle changed during the second ICBT fraction. This is expected because dose to the distal pelvic nodes is mainly contributed by the tip of the tandem. Rotating the tandem away from the midline where the nodes are located will move the dose away. Figure 14d shows that as the system was shifted further away from its original location, dose to the distal pelvic nodes decreased. This is reasonable since most shifts in system between the first and second ICBT fractions were in the anterior and inferior

direction, as shown in Figure 11. Both shift directions will move the dose cloud away from the distal pelvic nodes.

For the seven patients with positive distal pelvic nodes, tandem length differences varied between -1 cm to 1 cm between ICBT1 and ICBT2. We originally hypothesized that tandem length difference significantly correlates with distal pelvic nodes because increases in tandem length would move the tandem tip closer to the nodal regions and the opposite effect occurs when tandem length is shortened. However, correlation tests showed no significance between the two factors. The reason for that is the location of the tandem tip relative to patient anatomy is dependent on two factors, tandem length and system location in the SI direction. For example, one of the patients with decreased distal pelvic nodal dose from the second ICBT fraction also had a 1-cm longer tandem in ICBT2. However, its system location shifted 1.8 cm in the inferior direction. The tip of the tandem is actually 0.8-cm lower in the second ICBT fraction, thus causing lower distal pelvic nodal dose. Therefore, tandem length alone is not a predictor of nodal dose differences.

2.5.3 Differences in Result between Mean Dose and D_{90}

Because nodes are volumetric structures, it is not trivial to pick a point dose to describe the dosimetric properties of the entire nodal volume. Traditionally, mean dose has been used to describe nodal dose since nodes are typically small. However, when the dose gradient within the nodal structure is high, which is normally the case for ICBT, prescribing based on mean dose could lead to areas of underdose. Therefore, in addition to studying differences in mean dose, we studied differences in D_{90} . Prescribing nodal boost on the basis

of D_{90} guarantees that underdosage may occur in at most 10% of the target. For proximal and distal pelvic nodes, the mean \pm 1SD differences between ICBT1 and ICBT2 were closer to zero when D_{90} is used instead of mean dose: 5.2 ± 69.8 cGy and 8.6 ± 85.1 cGy for proximal, respectively, and -21.9 ± 38.4 cGy and -46.8 ± 55.3 cGy for distal, respectively. These results show that because of the dose gradient in the nodes, there are fewer differences in nodal dose in the low dose region. Using mean dose to represent entire nodal dose when analyzing nodal dose differences from independent ICBT fractions will result in an overestimation in the low dose region, thus not cause underdosage in the nodes.

2.5.4 Limitations and Assumptions

In this work, we made several assumptions. First, we assumed that the film images were orthogonal and were obtained exactly at 0° and 90° . However, although very close, this may not be exact for every patient because the films were obtained in the operating room with a portable computed radiography system. The film plate and x-ray unit may not be exactly perpendicular since they are independent entities. However, during treatment planning in Oncentra, common points on the orthogonal films were used by the treatment planning system to create a three-dimensional space model as accurately as possible. This ensures that the dose distribution is correct even when the films are not exactly orthogonal. Also, since DRRs are generated at exactly 0° and 90° , aligning them to films that are not exactly orthogonal might create misregistration. Second, we assumed that nodal regions are not deformed by applicator insertions. Previous studies at our institution have shown that applicator insertion has minimal effect on dose distribution of the nodes (90). Finally, the

method used to normalize ICBT prescription—normalizing ICRU point A dose—is crude. Although point A is one of the methods of evaluating dose prescription, it certainly does not provide all the information about the dose distribution. However, normalizing point A dose does improve consistency and is better than not normalizing at all.

2.6 CONCLUSION

We have demonstrated that the mean dose to the pelvic nodes can differ by up to 1.9 Gy between independent ICBT fractions. Tandem angle and total system shifts were found to impact distal pelvic nodes while AP/PA and lateral shifts were found to impact proximal pelvic nodal dose. Intracavitary brachytherapy can make a significant contribution to the total dose delivered to pelvic lymph nodes. Although the dose delivered from a single system is often a good predictor of the overall contribution from brachytherapy, in some cases the dose delivered from separate treatments in the same patient can vary significantly. This should be carefully considered in the overall planning of treatment for patients who have evidence of lymph node metastasis.

Chapter 3: Voxel-by-Voxel Bladder and Rectum Dose Accumulation between External Beam Radiation Therapy and Intracavitary Brachytherapy

3.1 SPECIFIC AIM 2

Develop and validate deformable image registration methods for the use of volumetric summation of bladder and rectum dose from ICBT to an external beam planning CT image set.

3.2 INTRODUCTION

3.2.1 Importance of Accurately Evaluating Total Bladder and Rectum Dose for the Prescription of Nodal Boost

During the prescription of external beam nodal boost, dose to the bladder and rectum is a major constraint on how much radiation can be delivered to the positive lymph nodes. For radiation therapy of cervical cancer, dose tolerances for maximum bladder and rectum point dose are 80 Gy and 75 Gy, respectively (91). As mentioned in Chapter 1, maximum doses to the bladder and rectum can be estimated by summing the EBRT prescription dose (this is done because a great portion of bladder and rectum are included in the primary EBRT field) with ICRU bladder and rectum point from ICBT. However, when conformal methods such as IMRT are used, this method becomes invalid because IMRT dose is heterogeneous with unpredictable hot and cold spots. Unless the maximum dose points from both EBRT and ICBT coincides at the same spot, simple dose summation can only represent the worst case

scenario and total organ dose will be overestimated. In order to accurately determine maximum organ dose, dose summation of bladder and rectum must be performed volumetrically.

3.2.2 Image registration

Image registration is the process of transforming different sets of data into one coordinate system. The process involves a 'static' and a 'moving' image, with the moving image transformed into the coordinate system of the static image. There are two major types of image registration, rigid and deformable. Rigid registration aligns two image sets by rotation, translation, scaling, or shearing. Since each of these transformations provides 3-degrees of freedom (ie. roll, pitch, and yaw for rotation and RL, AP, and SI shifts for translation) there are a total of 12 possible degrees of freedoms for rigid registration. Because rigid registration is a global process, its applications are limited and mostly used for cases where the anatomy does not change between images. In radiation therapy, rigid registration is mostly used in image guided radiation therapy (IGRT) where daily x-ray or CT images are taken prior to treatment and compared to digital reconstructed radiographs (2D/2D matching) or planning CT (3D/3D matching) respectively, for daily patient setup (92-94).

For organs that change shape non-rigidly, such as bladder and rectum, rigid registration is inadequate and deformable image registration (DIR) must be used. DIR is a voxel mapping process. Instead of registering the images globally, the algorithm looks to find corresponding voxels on the static and moving images. Since each voxel is registered independently, the number of degrees of freedom becomes infinite. There are two major

categories of DIR algorithms, feature-based and intensity-based. Feature-based algorithms are also often referred to as point-based or model-based methods. It extracts features, such as points, curves, and surfaces on the static and moving images to find its correspondence (95-99). Feature-based methods are normally very fast but require robust feature extraction to produce accurate results. On the other hand, intensity-based methods only require information from the image intensity values (100-104). It finds correspondence by maximizing an intensity similarity measure while also producing smooth transformations. Image intensity algorithms involve excessive computational power and pre-registration of the static and moving images must be performed to prevent the algorithm from being trapped by local minima.

Although there are differences between feature and intensity-based methods, both result in a vector field describing the transformation between the static and moving image. The field contains vectors indicating the direction and magnitude of transformation needed for each voxel on the moving image to match its corresponding voxel on the static image (Figure 15). The deformation field by itself is not very useful in radiation therapy. However, it can be used as a guide for contour and dose deformation, depending on the clinical needs. The deformation field is applied to the contours or dose from the moving image so users can view and evaluate them on the static image.

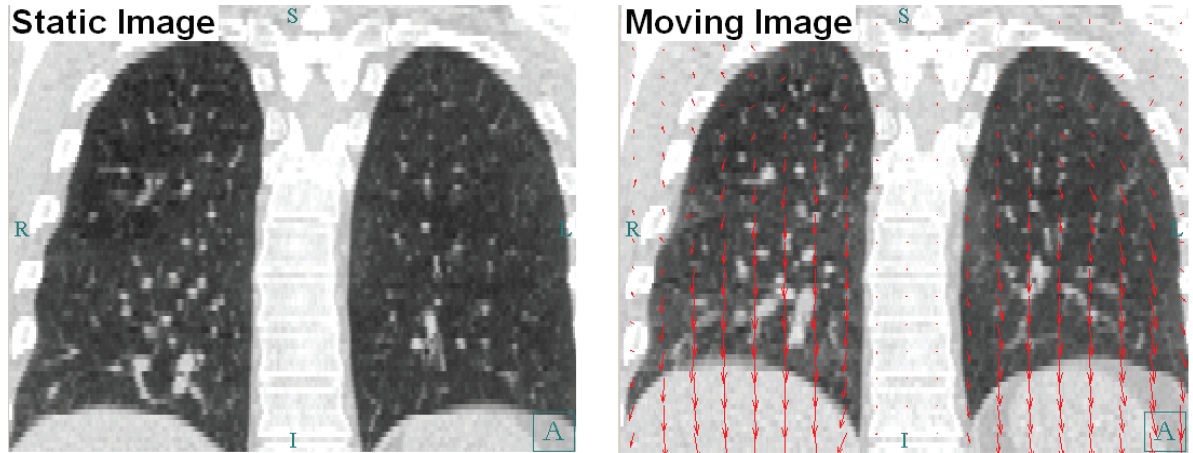


Figure 15: Example of a static (inhale) and a moving (exhale) image taken from a 4-dimensional CT image set. Deformation field resulted from DIR are shown on the moving image. We can see that in order for the exhale phase to be deformed to match the inhale phase, voxels (especially ones near the diaphragm) must be transformed inferiorly resulting in expansion of the lungs.

3.2.3 In-house accelerated demons algorithm

The intensity-based DIR method used in this project was first proposed by Thirion (103). It is referred to as the demons algorithm based on its analogy with Maxwell's demons (105). The demons algorithm uses the intensity of both static and moving images and the gradient of the static image to find correspondence between the two. The equation for the demons algorithm is:

$$\vec{v} = \frac{(m-s)\vec{\nabla}s}{|\vec{\nabla}s|^2 + (m-s)^2} \quad (1)$$

with m and s indicating voxel values on the moving and static image, $(m - s)$ indicating the registration force between the images, and $\vec{\nabla}s$ representing the gradient of the static image. Equation 1 is calculated iteratively for each voxel until the solution converges. In areas of low gradient, the original demons algorithm becomes inefficient. To solve this problem and

increase speed, Wang et al. (104) added an active force to the original diffusion process. If we make the assumption that diffusion of the images is bi-directional, the active force is the force which allows the static image to diffuse into the moving image. This lowers the number of iterations needed for the demons algorithm to converge and increases speed of registration. The equation for “accelerated” demons algorithm is:

$$\vec{v} = (m - s) \times \left(\frac{\vec{v}_s}{|\vec{v}_s|^2 + \alpha^2(s-m)^2} + \frac{\vec{v}_m}{|\vec{v}_m|^2 + \alpha^2(s-m)^2} \right) \quad (2)$$

The first term inside the second bracket is the passive force as shown in Equation 1 and the second term is the active force. The α^2 term was added to the denominator of the terms in the brackets to limit the step size of each iteration to $1/(2\alpha)$. Therefore, even with large differences between $(m - s)$, the algorithm cannot make large jumps during any iteration. A Gaussian filter with a variance of σ^2 is applied to the result after each iteration to smooth, suppress noise, and preserve geometric continuity of the deformation field.

To further speed up the algorithm, prevents results from being trapped by local minima, and limits the effect of large deformations Wang et al. also implemented a multi-resolution approach (104). The algorithm is initially calculated at an image resolution that is much coarse than the original. When the solution converges, the resolution is increased and the displacement fields from the previous calculations are used as starting points for the next round of iterations. This process is repeated multiple times until the original image resolution is used.

3.2.4 Using DIR for Dose Summation of Bladder and Rectum

With increasing number of commercially available image registration software, usage of DIR for the purpose of dose summation has increased dramatically in recent years. Currently, most dose summation using DIR are performed in regions where anatomical deformations are reproducible and small, such as different phases of the breathing cycle in the lungs (106). On the other hand, dose summation for bladder and rectum has remained a challenging task. Problems caused by extremely homogeneous features and greatly varying sizes make accurate voxel-by-voxel registration in the bladder very difficult. In the rectum, the major problem with using DIR is the variable rectal filling and gas content. Gas content is especially difficult to address because it may not have corresponding voxels on the aligned images. Errors arise in our image intensity based DIR algorithm when corresponding voxels simply does not exist.

Volumetrically summing bladder and rectum dose between EBRT and ICBT is an even more difficult task. In addition to the problems just described, there are several additional issues which need to be considered. First, the ICBT CT images contain the brachytherapy applicator, Foley balloon and catheter, and vaginal packing; all are nonexistent on the EBRT CT images. Second, the bladder is empty during ICBT which is not the case in EBRT, thus causing large bladder deformations between EBRT and ICBT images. Finally, the vaginal packing is intended to push the bladder and rectum away from the applicator. This causes large and unnatural shifts in bladder and rectum location between EBRT and ICBT. The purpose of this project is to develop and validate a voxel-by-voxel dose summation method for the bladder and rectum between EBRT and ICBT CT image sets.

With more accurate understanding of the total organ dose, radiation oncologists can consider nodal boost prescription escalation without any concern about normal tissue complexities.

3.3 METHODS AND MATERIALS

3.3.1 Patient Cohort

Twenty patients were selected retrospectively for this study. All patients were initially part of a prospective Internal Review Board approved protocol. The patients had clinical stage IB to IVA cervical cancer and were treated between August 2008 and June 2011. Patients were selected based on the criteria of having CT image sets for both external beam radiation therapy and ICBT. Patients were treated using different types of brachytherapy applicators: 14 patients were treated using a unique shielded but CT artifact-free Fletcher-Suit-Delclos tandem and ovoid applicator (107, 108), 2 received tandem and mini applicator, 2 received tandem and ring applicator, and 2 received tandem and cylinder applicator. All applicators were manufactured by Nucletron (Nucletron, Netherlands), CT compatible, and CT image artifact free. It is extremely important that the applicators used do not cause artifacts on the CT images because it would compromise image registration results.

3.3.2 Contour Based Validation Metrics

One method of validating DIR algorithms is by evaluating deformed contour results. Unlike deformed dose, the accuracy of deformed contours can be easily determined. Since the human brain can process gray-scale images much more effectively than computers (109), bladder and rectum contours delineated by radiation oncologists can be used as the ground

truth for DIR validation. In this study, a single radiation oncologist delineated bladder and rectum contours on both external beam planning CT images (EBRT-CT) and ICBT planning CT images (ICBT-CT). Patient bladders were delineated to include the Foley balloon, and patient rectums were delineated from the level of the distal end of the sigmoid colon to that of the ischial tuberosities (110). An example of the contours and the DIR results are shown in Figure 16. To validate the accelerated demons algorithm for bladder and rectum, we deformed radiation oncologist delineated contours from EBRT-CT to ICBT-CT. The deformed contours on ICBT-CT were then compared with delineated contours using volume ratios, Dice's coefficient (111, 112), and mean absolute distance. Volume ratio is calculated by dividing the deformed region volume by the delineated region volume, $V_{\text{deformed}}/V_{\text{delineated}}$. Dice's coefficients are calculated using the equation:

$$s = \frac{2|X \cap Y|}{|X| + |Y|} \quad (3)$$

where X and Y are the different contoured regions. Dice's coefficient measures the similarity between two contoured volumes. More specifically, the formula represents the size of the union of the two sets divided by their average size. The result ranges between 0 and 1, with 0 being no overlap and 1 indicating perfect agreement. Finally, mean absolute distance is calculated by taking the mean of the distances from deformed contours to the nearest point on the delineated contour. The evaluation metrics were calculated independently for bladder and rectum.

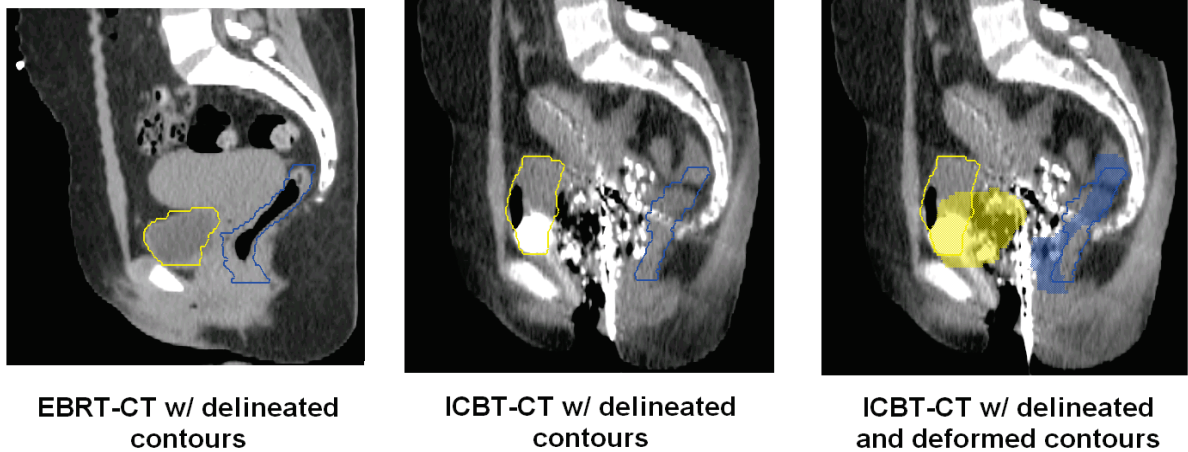


Figure 16: Example showing the differences between EBRT-CT and ICBT-CT with the bladder (yellow) and rectum (blue) delineated by a radiation oncologist. The image on the right shows deformed contours (colorwash) mapped onto the ICBT-CT image. One can see that neither bladder nor rectum agreed well with radiation oncologist delineated contours.

3.3.3 Binary deformation

Evaluating the results using validation metrics presented in Section 3.3.2 have shown that bladder and rectum deformation results between EBRT-CT and ICBT-CT were extremely poor when image registration relied on image intensities alone (further details will be provided in Section 3.4.1). In order to improve registration results, it was necessary to provide extra information to the DIR algorithm in addition to the image intensities. Our proposed method to improve DIR results was to force the organ boundaries to match. To do so, we converted both CT images to binary images based on the delineated contours. All the voxel CT numbers within the contours were changed to 1000 and everything outside was changed to 0, as shown in Figure 17. Because the demons algorithm forces the moving image to diffuse toward the gradient, a definitive binary boundary will force the boundaries to match. Once all images were converted to binary and the binary EBRT-CTs were deformed

to binary ICBT-CTs, deformation results were evaluated once again using volume ratio, Dice's coefficient, and mean absolute distance.

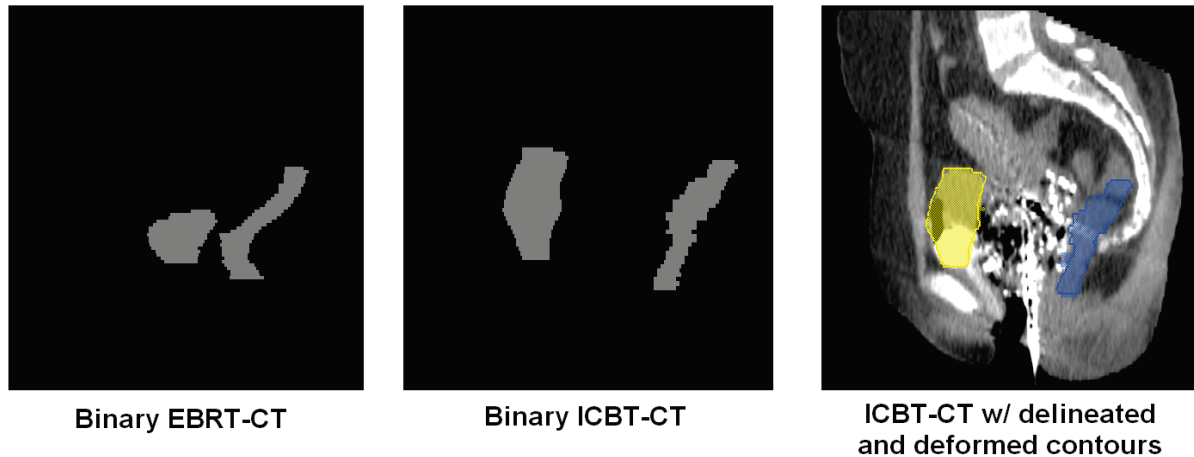


Figure 17: Example of binary EBRT-CT and binary ICBT-CT generated based on radiation oncologist drawn contours. The image on the right shows binary deformed contours (colorwash) mapped onto the ICBT-CT image. One can see that compared to using image intensities alone (Figure 16), both deformed bladder (yellow) and rectum (blue) contours agreed very well with their delineated counterparts.

3.3.4 Voxel-by-voxel Validation Method

Validating DIR results using contours only provide partial information about the overall accuracy of the registration method. Bad boundary agreement means the registration results were poor. On the other hand, good boundary agreement means the results are better, but is not enough to evaluate the accuracy of registrations for voxels within the contours. In order to validate the accuracy of DIR algorithms for the use of dose accumulation, a voxel-by-voxel method must be used. In this study, we proposed a novel method to generate a pair of artificial CT images with known deformation between them so that we are able to test our DIR algorithm by comparing the calculated deformation field with the known deformation

field. A few criteria must be met for the results to be clinically relevant. First, the artificial images must be created using population data in order to represent an entire population, not just a single patient. Second, the images must simulate real clinical situations, in our case, deformation in bladder and rectum between EBRT-CT and ICBT-CT images. Finally, we must know the exact deformation field between the two images in order to use it as ground truth.

The method we used to create population based artificial CT images is based on the active shape model proposed by Cootes et al. (113). The active shape model captures the most prominent variations of certain structure from a population of the structure shapes through principal component analysis technique. In our method, variations between two shapes are represented by a deformation field in a 3D space. The first step is to determine the average variability of shapes within a population and calculate the mean deformation, \bar{d} . Second, the modes of variations, \mathbf{P} , are calculated by applying principle component analysis to the population of deformation fields. $\mathbf{P} = (\mathbf{p}_1, \mathbf{p}_2, \dots, \mathbf{p}_t)$ is the matrix of the first t eigenvectors in the principal component analysis, which represents the most prominent variations (at least 90% of the total variations) deviating from the mean deformation. A new deformation can then be generated from the population model using the equation:

$$d = \bar{d} + \sum_{i=1}^t b_i \bar{p}_i \quad (4)$$

where b_i is generated randomly and represents the deformation contributed by the i^{th} mode of variation. In order to ensure the deformation is reasonable, a maximum value, D_{max} , is enforced on the generation of random number b_i according to equation 5:

$$\sum_{k=1}^t \left(\frac{b_k^2}{\lambda_k^2} \right) \leq D_{\max}^2 \quad (5)$$

Using this method, we can generate a new random deformation field, which can be applied to a reference CT image set to generate artificial CT images resembling real human CT images.

We applied the aforementioned method to our patient population to obtain the inter-patient and intra-patient variations to generate artificial CT images which represent an entire population and have clinically relevant deformations between EBRT-CT and ICBT-CT. Knowing the inter-patient variations allows the creation of population artificial CT images. Intra-patient variations indicate the amount of deformation between EBRT-CT and ICBT-CT for each patient.

To determine inter-patient variations, we first chose one of the 20 patients as the reference patient. The reference patient was chosen to represent the approximate median of the population. We also made sure the reference CT image sets, termed EBRT-CT Ref and ICBT-CT Ref, had high contrast-to-noise ratio and were free of artifacts. To generate the inter-patient deformation field for EBRT-CT, the CT image sets of the remaining patients were aligned to the reference patient using our DIR algorithm, creating 19 deformation fields (EBRTx - EBRT Ref), as shown in Figure 18. The fields were then used to generate the population sampled deformation field (Inter-Patient Deformation Field), shown in Figure 19. When the Inter-Patient Deformation Field is applied to the EBRT-CT Ref image, it creates an artificial CT image (EBRT Artificial CT) which represents the population in the study (Figure 20).

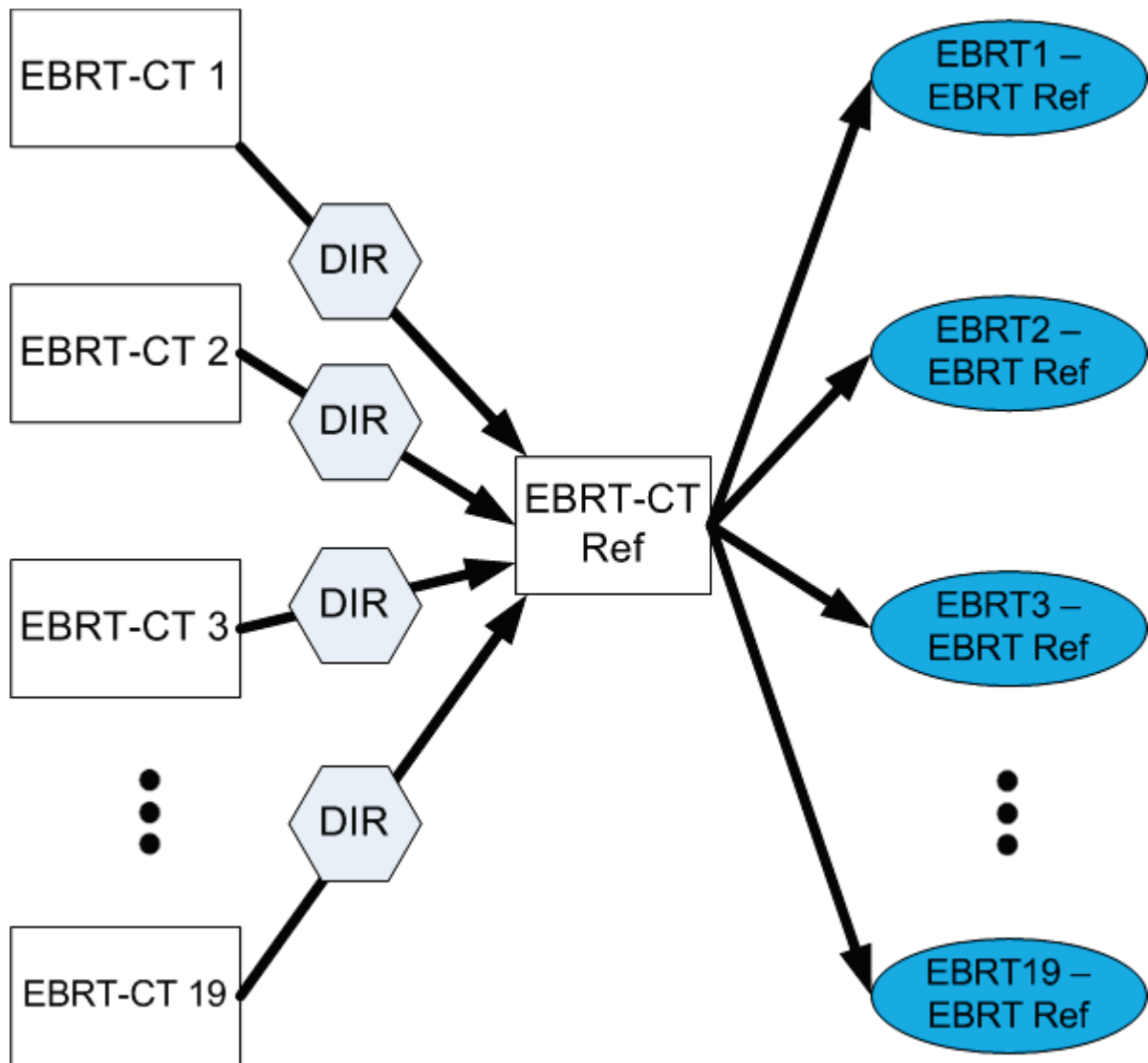


Figure 18: Using a reference patient to create a group of deformation fields.

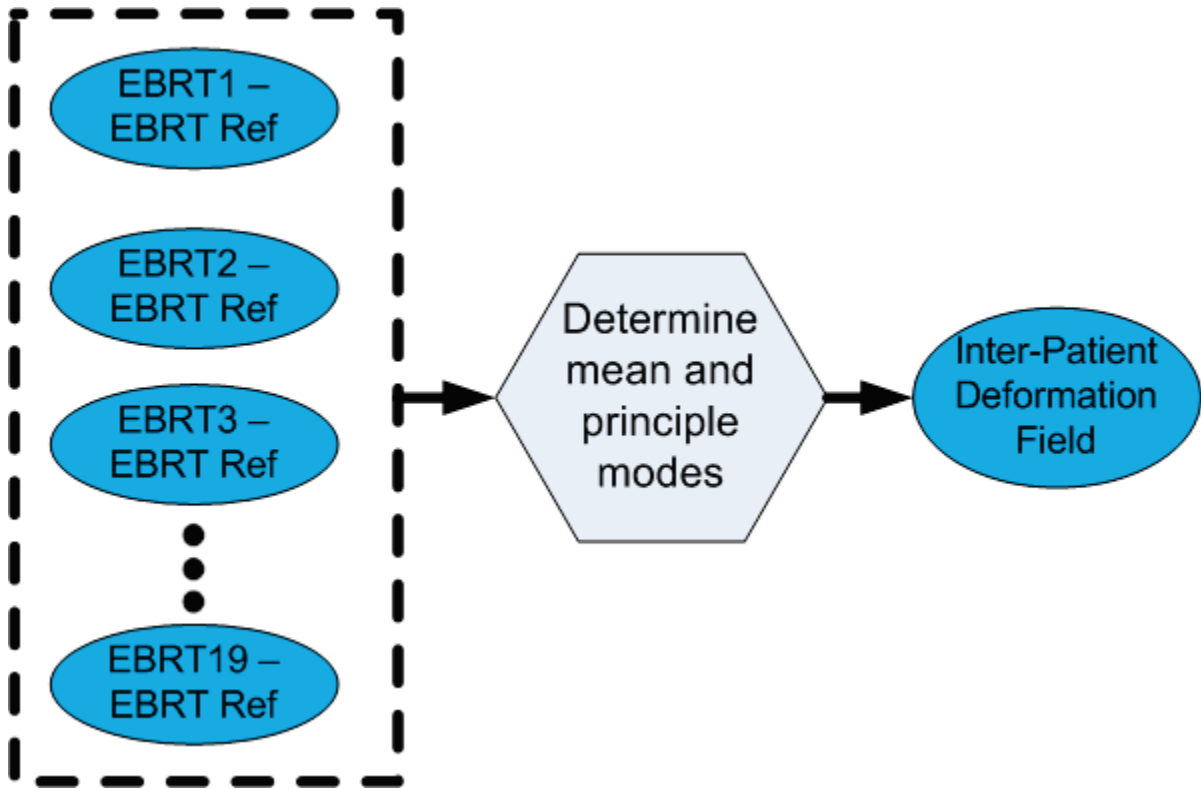


Figure 19: The group of deformation field is then used to create a inter-patient deformation field.



Figure 20: Using the Inter-Patient Deformation Field, we generated an artificial population CT image.

To create the population set which represents variability between EBRT-CT and ICBT-CT, we first deformed the EBRT-CT to its corresponding ICBT-CT for all patients (Figure 21). Once we have the deformation fields for all patients, we generated a intra-patient

deformation field using the same method as before (Figure 22). The resulting deformation field (Intra-Patient Deformation Field) represents the principle anatomical variations between external beam CT images and brachytherapy images. Also, to create the ICBT Artificial CT image, we needed to know the deformation field between the two reference images (Ref Def Field), as shown in Figure 23. Generating the ICBT Artificial CT image is not as straightforward as generating the EBRT Artificial CT image. The detailed process is shown in Figure 24. The concept is to first spatially transform the ICBT-CT Ref image to the EB-CT Ref image, while retaining ICBT characteristics (contains applicator, Foley balloon, etc.). This image with the ICBT characteristics was then spatially transformed into the space of EBRT Artificial CT image using Inter-Patient Deformation Field. Finally, we created the ICBT Artificial CT image by further applying the Intra-Patient Deformation Field. An example of EBRT Artificial CT and ICBT Artificial CT generated using $D_{\max} = 2$ is shown in Figure 25. The variability between EBRT Artificial CT and ICBT Artificial CT is the Intra-Patient Deformation Field and that is our known field.

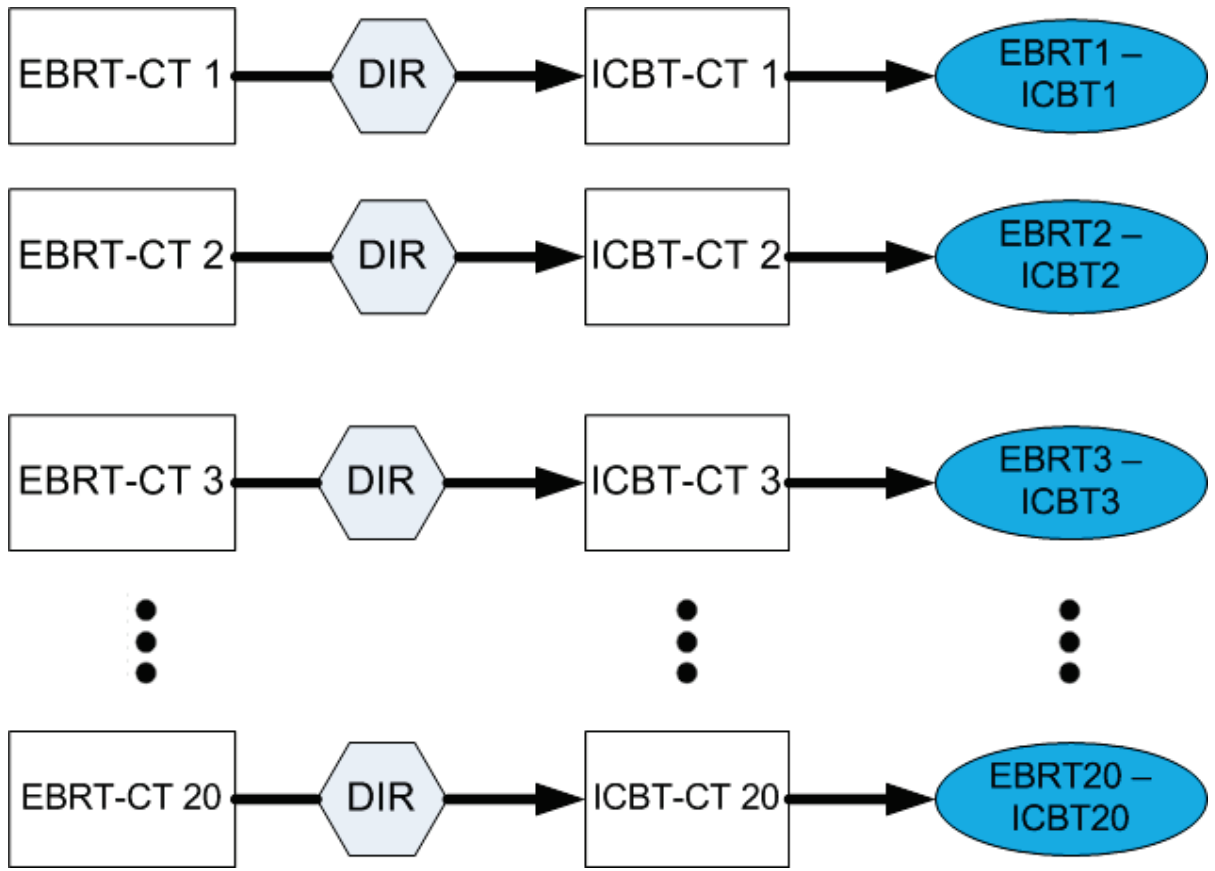


Figure 21: Creating a group of deformation fields between external beam CT images and brachytherapy images.

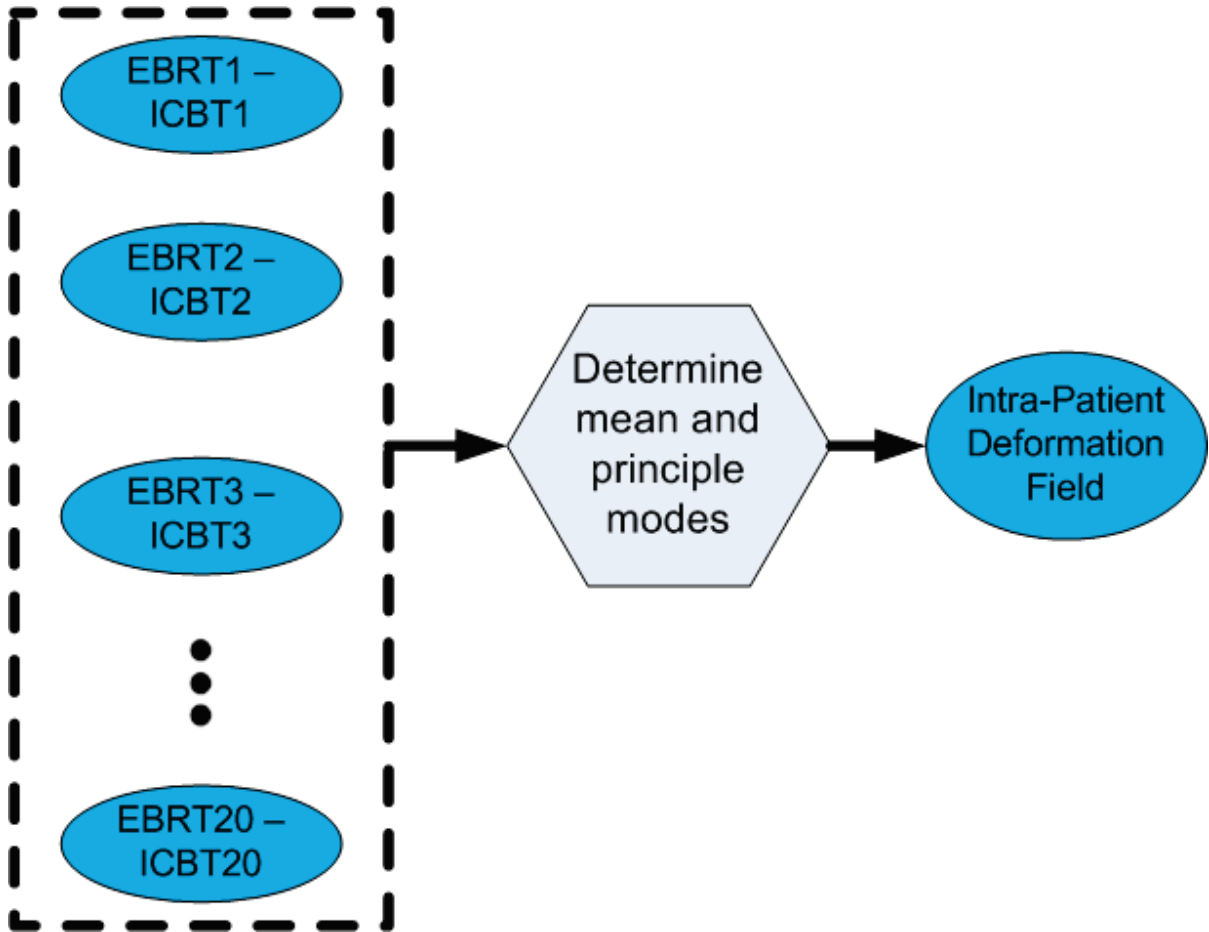


Figure 22: Using the group of intra-patient deformation fields to create a population deformation field between external beam radiation therapy and brachytherapy CT images (Intra-Patient Deformation Field).



Figure 23: The deformation field between the Reference images (Ref Def Field) is needed for creating the simulation ICBT image.

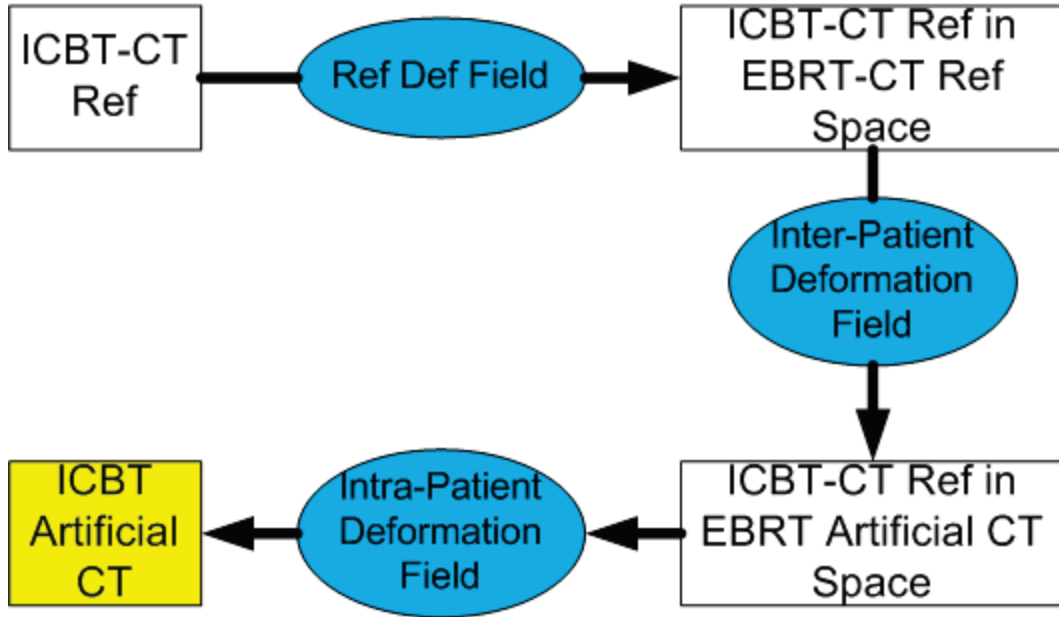


Figure 24: In order to create the ICBT Artificial CT, the original ICBT-CT Ref must go through a few transformations into different CT image space.

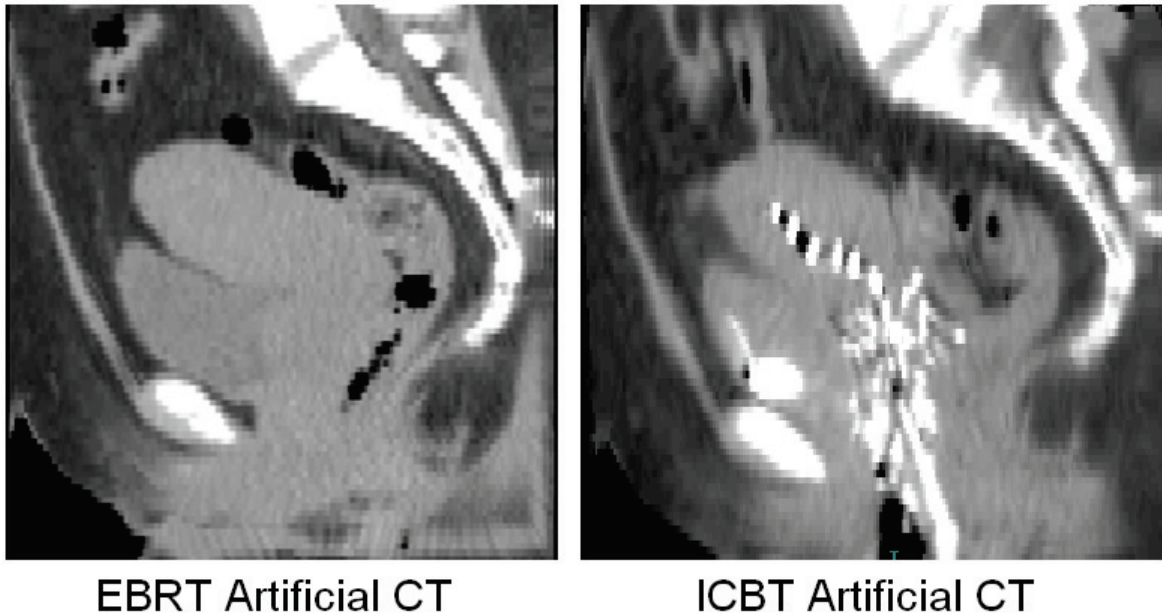


Figure 25: Example of EBRT Artificial CT and ICBT Artificial CT generated using $D_{\max} = 2$. Since our choice for D_{\max} is not large, the deformation between the two images is not as severe.

3.3.5 Validation of Deformation Results

Using the artificial CT image pairs generated by the method described in Section 3.3.4, we could validate the deformation results for the bladder and rectum. By subtracting the deformed field from the known field, we can quantify differences in the RL, AP, SI directions and total magnitude for each voxel. The total magnitude was calculated by taking the root of the sum of squares in the three directions. The mean difference of all voxels was reported as the error in registration. We then converted the simulated CT images into binary images as described in Section 3.3.3 and repeated voxel-by-voxel validation for the bladder and rectum. To test DIR accuracy with varying amounts of deformation, we validated the normal and binary deformation results with D_{\max} set at 2, 3.5, and 4.5.

3.4 RESULTS

3.4.1 Contour Based Validation

Results from contour based validations are shown in Table 2 and 3. By using a binary method instead of image intensities alone, the deformed contours have shown much better agreement with delineated contours. On average, the Dice's coefficient increased by 0.39 and 0.41 for the bladder and rectum, respectively. The mean absolute distance decreased by 5.6 mm for both organs. Typically, when judging similarity of two regions based on Dice's coefficient, which ranges from 0 to 1, a value of 0.7 is considered acceptable and 0.8 is considered good. When deforming using normal methods, Dice's coefficient for the bladder and rectum exceeded 0.7 in 8 of 20 (40%) and 0 of 20 (0%) patients, respectively. When the criteria is raised to 0.8, only 3 of 20 (15%) bladders and 0 of 20 (0%) rectums exceeded it.

On the other hand, when binary methods are used, all 20 bladder and 19 of 20 (95%) rectum deformations exceeded a Dice's coefficient of 0.8.

Table 2: Evaluation of contour agreement between deformed and delineated for bladder using image intensity alone (Normal) and Binary methods.

	Bladder			
	Normal		Binary	
	Mean+1SD	Range	Mean+1SD	Range
Volume Ratio	1.04+0.45	0.36-1.86	0.98+0.02	0.93-1.01
Dice	0.57+0.2	0.2-0.88	0.96+0.02	0.92-0.98
Mean Absolute Distance (cm)	0.65+0.29	0.23-1.06	0.09+0.02	0.05-0.13

Table 3: Evaluation of contour agreement between deformed and delineated for rectum using image intensity alone (Normal) and Binary methods.

	Rectum			
	Normal		Binary	
	Mean+1SD	Range	Mean+1SD	Range
Volume Ratio	0.91+0.44	0.25-1.88	0.95+0.06	0.75-1.05
Dice	0.5+0.1	0.3-0.66	0.91+0.04	0.79-0.95
Mean Absolute Distance (cm)	0.69+0.23	0.39-1.31	0.13+0.07	0.07-0.35

3.4.2 Mean Error from Voxel-by-Voxel Validation

Mean differences of all voxels between deformed and known deformation fields in the RL, AP, SI, and total magnitude are shown in Table 4. The mean error in registration for the bladder using image intensity alone (Normal) DIR methods were 0.98 mm, 1.09 mm, -0.17 mm, and 3.47 mm in the RL, AP, SI, and total magnitude, respectively. Using the binary DIR method, the mean errors in registration for the bladder were 0.24 mm, -2.76 mm, -1.33 mm, and 4.61 mm in the RL, AP, SI, and total magnitude, respectively. For the rectum, the mean errors in registration using Normal DIR methods were 0.02 mm, -0.86 mm, -0.37 mm,

and 2.74 mm in the RL, AP, SI, and total magnitude, respectively, while the mean errors in registration using binary DIR methods were 1.39 mm, 1.54 mm, 3.19 mm, and 5.6 mm in the RL, AP, SI, and total magnitude, respectively. Figure 26 shows an example of the histograms for bladder and rectum voxel misregistration using normal and binary methods when D_{max} is set to 2.

Table 4: Mean errors in registration (mm) for all voxels in the bladder and rectum.

	D_{max}	Bladder			Rectum		
		2	3.5	4.5	2	3.5	4.5
RL	Normal	1.38	1.44	0.12	0.09	-0.14	0.11
	Binary	0.84	-0.30	0.19	1.76	1.34	1.09
AP	Normal	1.12	0.86	1.30	-0.51	-1.06	-1.00
	Binary	-2.73	-3.25	-2.30	1.95	1.23	1.46
SI	Normal	0.64	-0.70	-0.44	-0.22	-0.12	-0.76
	Binary	-1.38	-1.26	-1.35	2.81	3.48	3.28
Mag	Normal	3.32	3.69	3.41	2.51	2.73	2.98
	Binary	4.11	5.09	4.64	5.28	6.08	5.43

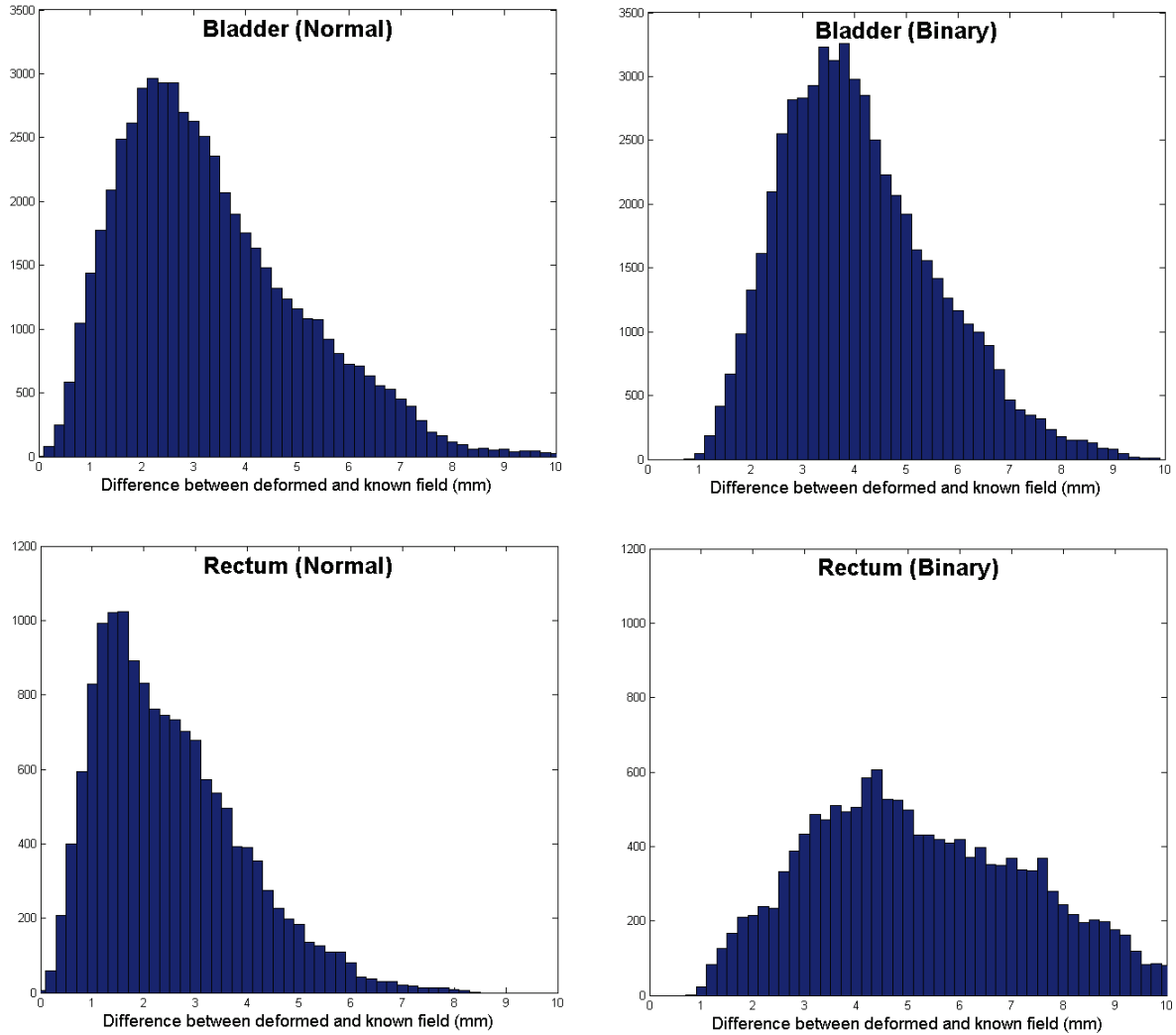


Figure 26: Histogram of errors in registration between deformed and known deformation fields. Both bladder and rectum were analyzed using normal and binary deformation methods. D_{\max} in this example was 2.

3.5 DISCUSSION

3.5.1 The importance of voxel-by-voxel validation

With the increasing availability of commercial software which offers FDA approved DIR tools for volumetric dose summation, it is even more crucial to develop voxel-by-voxel

validation tools to understand the magnitude of uncertainties associated with DIR algorithms. In a recent point/counterpoint published in Medical Physics, the appropriateness of adaptive radiation therapy using dose deformation was hotly debated (114). Although both sides were debated, the consensus was that accurate DIR is a difficult clinical problem which requires full understanding of the limitations from both physicists and radiation oncologists in order to be safely used in the clinic. Quantifying registration errors is the first step toward understanding limitations and determining appropriate uses of DIR.

Currently, the three most commonly used methods of voxel-by-voxel DIR validation use anatomical landmarks, anthropomorphic phantoms, and mathematical phantoms. In regions where anatomical landmarks are easily seen and can be reproduced accurately, landmarks are identified on both static and moving images. After DIR between the two images, landmarks on the deformed moving image is compared to landmarks on the static image. Differences in landmark locations between the two are the errors in registration. Most common uses of landmarks for DIR validation are in the thoracic or liver regions where bronchial or vessel bifurcations can be accurately identified (96, 115). Another method for DIR validation is by using anthropomorphic phantoms which can be physically deformed to a known amount. For example, Kirby et al. (116, 117) built a head & neck and a pelvic phantom which contains glow in the dark optic markers that are CT transparent. This is useful because the optical markers do not influence DIR results. When the phantoms are deformed, the deformation fields can be measured optically and compared with DIR calculated deformation fields based on the pre and post deformed CT images. Finally, one can take a CT image and artificially create simple deformations using software to generate a

new CT image. DIR algorithms are tested by deforming the new CT image with the original CT image and compared with the applied deformation (104, 118).

Established methods such as landmarks or phantoms are not ideal for this study. Unlike thoracic or liver regions where bronchial or vessel bifurcations can be accurately identified, bladder and rectum lack landmark points which may be used for validation. Also, building an accurate anthropomorphic volumetric phantom of the female pelvis with the ability to mimic bladder and rectum changes after an ICBT applicator insertion is not trivial. There are a few reasons why our validation method is novel and advantageous compared to other available methods. First, our method utilizes and creates realistic patient CT images without having to physically build a phantom. This makes the process extremely simple and can be used widely by many clinics with their own patient database. Second, the known deformation field is generated using population data. Therefore, the artificial deformations are clinically relevant and represent real patient anatomical variations. Third, we have provided a method to generate artificial ICBT images while still maintaining the known deformation field between it and the artificial EBRT-CT image. Finally, although we only validated our method for the bladder and rectum between the EBRT-CT and ICBT-CT images, our proposed method can be used for any site and any DIR algorithm. Institutions wishing to validate their in-house or commercial DIR programs can easily do so by generating artificial images with known deformation fields for their organs of interest and patient population using the guidelines provided in this study.

3.5.2 Comparing Binary and Normal Methods Using DIR Evaluation Metrics

As Table 2 and 3 have shown, using image intensity alone for DIR of EBRT-CT to ICBT-CT resulted in very poor agreement at the boundaries. This is not a surprise since we already anticipate deformations in the bladder and rectum region is large. Also, constraints are placed in the DIR algorithm to prevent large “unrealistic” deformations. When deformations are actually large, the maximum deformation vector magnitude allowed is the calculation result instead of the true deformation. Using image intensities alone, the mean Dice’s coefficient for both bladder and rectum is only around 0.5 or 50% similarity between deformed and delineated contours. Even without voxel-by-voxel validation, we can make the conclusion that image intensity alone will not be appropriate for dose summation between EBRT-CT and ICBT-CT. If the boundaries are incorrectly deformed, voxel registrations within the boundaries are going to be incorrect as well. By converting the images to binary images, we forced the boundaries to match, which in theory should improve registration results. Our results have shown that by using the binary method, the boundaries matched extremely well even with large deformations.

Before discussing the results from our voxel based validation method, the limitations and drawbacks of the binary method need to be listed. First, human interaction is required for the binary process. The organs of interest must be manually delineated on both static and moving images. This is not required if using image intensity alone. The accuracy of the deformation results also becomes highly dependent on the accuracy and consistency of the delineated contours. Second, by converting images to binary, we lose the image information within the contours. Since all voxels within the volume are have CT number of 1000, the

deformations of the inner voxels are essentially interpolated based on where they are located and the amount of deformation at the boundary.

Comparing registration results for the bladder and rectum on our artificial images. We observed that overall errors in registration are less for the normal image intensity registrations. This is unexpected since the boundary validations have shown better results using the binary method. Upon reviewing the artificial images, we concluded that one of the main reasons image registration results were good for our artificial images was because the chosen D_{\max} were small. Since D_{\max} determines the maximum amount of deformation that could be created, we did not generate the extreme organ deformations which were observed between EBRT-CT and ICBT-CT. To test this theory, we increased the D_{\max} value from 2 to 3.5 and 4.5. When we increased D_{\max} , DIR becomes less accurate for both image intensity and binary registration methods, as shown in Table 4. We also observed that increasing D_{\max} affected image intensity registrations more than binary registration. This is because binary registrations are much better at handling large deformations than image intensity based registrations. Figure 27 shows a sagittal view of the bladder and rectum with the total magnitude of error for each voxel. For image intensity based registration (Normal), the regions with accurate and inaccurate registrations were scattered throughout the region. For binary registration, the more accurate regions were in areas where deformations were small. On the contrary, less accurate regions were located in areas with large deformations.

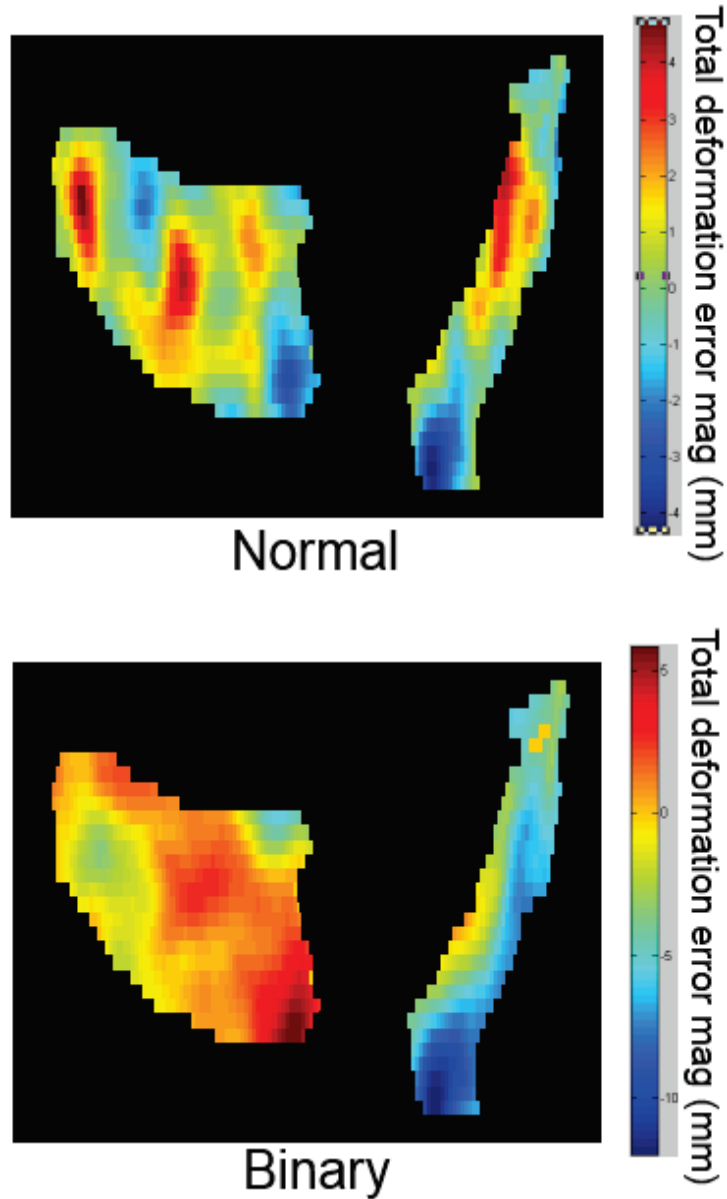


Figure 27: Sagittal view of total magnitude registration errors for normal and binary methods for each voxel. One can see that errors in registration on the normal method occurred at places where voxels lacked correspondence between the EBRT-CT and ICBT-CT images. For the binary method, registration errors were greatest in regions where deformation was large.

Comparing our registration results to results found by other research groups, we found that our results were very much in line with published data, which varied between 2 to 7 mm (96, 104, 115-118). We found that mean errors in bladder and rectum registrations are 3.5 mm and 2.7 mm for image intensity registrations, respectively, and 4.6 mm and 5.6 mm for binary registrations, respectively. The advantage of our voxel validation method is that our results are patient population, organ, and DIR algorithm dependent. The results of this work are specific to our demons algorithm and for bladder and rectum deformations between EBRT-CT and ICBT-CT.

3.6 CONCLUSION

We have created a method to improve DIR of the bladder and rectum between an external beam CT image and an ICBT CT image. We also developed a voxel-by-voxel validation method to quantify the errors in registration. By doing so, we have explored the limitations in such DIR process so that physicist and radiation oncologists can have better understanding of what the deformation results mean and how it can be used clinically.

Chapter 4: Beam Angle Specific Margins to Account for Anatomical Uncertainties during Proton Therapy in Nodal Boost Planning for Cervical Cancer

4.1 SPECIFIC AIM 3

Calculate nodal boost planning margins needed for proton therapy to account for interfractional anatomical variations.

4.2 INTRODUCTION

In recent years, proton therapy has become more mainstream and accessible to patients needing radiation therapy. According to the Particle Therapy Co-Operative Group, as of February 2013, there are 11 centers in operation and 8 under construction in the United States alone (119). The main attraction of protons therapy is that the beam has finite range and delivers almost all of its energy at the end of its range (termed the Bragg peak); almost no energy is deposited beyond the Bragg peak. Clinically, this feature of protons is extremely advantageous because all organs beyond the distal edge of the beam can be spared from radiation. Unfortunately, CT number, beam energy, setup, and patient motion uncertainties can all affect the proton range (120, 121). Currently, a simple method is used to account for such uncertainties: 3.5% of the spread-out Bragg peak is applied as distal and proximal margins, as proposed by Moyers et al. (122). However, current methods rarely explicitly account for patient's interfractional anatomy changes, which could have a big effect on target coverage.

In patients with involved pelvic lymph nodes, nodal boost with radiation (“boost”) is given to increase the total dose to the involved nodes to 60 to 66-Gy (79). Although nodal involvement from cervical cancer may occur anywhere along the lymphatic drainage pathway, cervical cancer most commonly spreads to the external iliac nodes and common iliac nodes (77, 78). Currently, though nodal boost doses are typically delivered using external beam photon therapy, proton therapy can generate theoretical dose distributions unmatched by photons for nodal boosts. For example, a single PA proton beam can be used to deliver conformal dose to external iliac nodes. Small bowel will be spared because it lies beyond the distal margin. However, uncertainty related to interfractional anatomical changes need to be considered thoroughly in order to use proton therapy to target the nodal boost volume.

Dosimetric differences caused by interfractional anatomical variations are magnified in nodal boosts because a very small target is irradiated over a small number of fractions. Any variation in anatomy in the beam path can cause the proton beam edge to shift off the target, resulting in undercoverage in either the distal or proximal end of the target. Shifts in distal and proximal edges of the beam may also potentially move the high dose region into adjacent normal tissues, causing complexities. Thus, adequate distal and proximal margins must be used during proton nodal boost planning to account for anatomical uncertainties, in addition to the uncertainty of CT numbers (122). Modeling and predicting interfractional anatomical changes is not trivial. Anatomical variations are dependent on target location, target size, and beam angle.

The purpose of this aim was to develop a general approach to determining the margins needed to account for interfractional anatomical variations during proton therapy. We applied this approach to determine the optimal beam orientation and required margins for delivery of radiation boost to external iliac and common iliac nodes using proton beams.

4.3 METHODS AND MATERIALS

4.3.1 Patient Cohort

Patients in this study were originally part of an Institutional Review Board approved prospective study of internal organ motion in cervical cancer patients (22). Images obtained from the previous study were retrospectively evaluated in this study. CT images from 16 patients with Stage IB2 through IIIA cervical cancer who had been treated with concurrent chemoradiation without hysterectomy were used for this study. Eight patients had Stage IB2 disease, 1 had Stage IIA disease, 6 had Stage IIB disease, and 1 had Stage IIIA disease. Each patient underwent a simulation CT scan prior to treatment planning, first with the bladder full and then with the bladder empty, performed with a Philips AcQSim3 CT scanner (Philips Medical Systems, Andover, MA) using our standard pelvic CT imaging protocol. All patients received primary EBRT followed by 2 fractions of PDR ICBT. The EBRT fractionation schemes used were 43.2 Gy in 24 fractions (6 patients) and 45 Gy in 25 fractions (10 patients). Patients also underwent a CT scan weekly prior to treatment, performed with an in-room CT-on-Rails system (GE Healthcare, Milwaukee, WI). Patients were weighed prior to chemotherapy and at weekly check-ups to ensure no sudden weight loss or gain.

4.3.2 Automatic Contour Delineation

In each patient, the goal was to design the radiation fields to cover the most frequently involved external iliac and common iliac lymph nodes as identified in a study recently published by Fontanilla et al. (77). To avoid interobserver and contour delineation uncertainties, DIR using an in-house developed software (104) was used. The study by Fontanilla et al. included an atlas in which PET-positive nodal locations from 45 patients were summarized on a single reference CT scan. We designed the clinical target volume (CTV) used in this study to cover external iliac nodal regions that were positive in at least 14% of patients in the Fontanilla et al. study and common iliac nodal regions that were positive in at least 12% of the patients in that study. Since positive nodes may occur anywhere along the lymphatic drainage, nodal regions positive in 12% of the patients is considered high occurrence. Nodal contours from the atlas were deformed to each planning CT. All deformed contours were expanded and smoothed using contouring tools in the Pinnacle TPS version 9.0 (Philips Medical Systems, Andover, MA). Then, all contours were verified and approved by a radiation oncologist.

4.3.3 Patient Setup

Currently, for proton therapy delivered at our institution, in-room kilovoltage x-ray images are used for daily treatment setup alignment. The limitation of such a technique is that only bony anatomy is visible in the image. In the case of nodal boost treatments, bone-based alignment method is sufficient since lymph nodes are typically fixed with respect to bony anatomy. To simulate treatment scenarios for the current study, we delineated a pelvic

bony region of approximately 2-cm in cranial-caudal dimension near the external iliac nodes and a second region at the superior portion of the sacrum. Those regions were used as alignment surrogates for the external iliac and common iliac nodes, respectively. Nodal contours from planning CT were transferred to weekly CT images using rigid image alignment of the delineated bony structures (92, 123). The rigidly aligned nodal contours on the weekly images represented the actual dose delivery region without daily patient setup uncertainties. Illustration of the process can be seen in Figure 28.

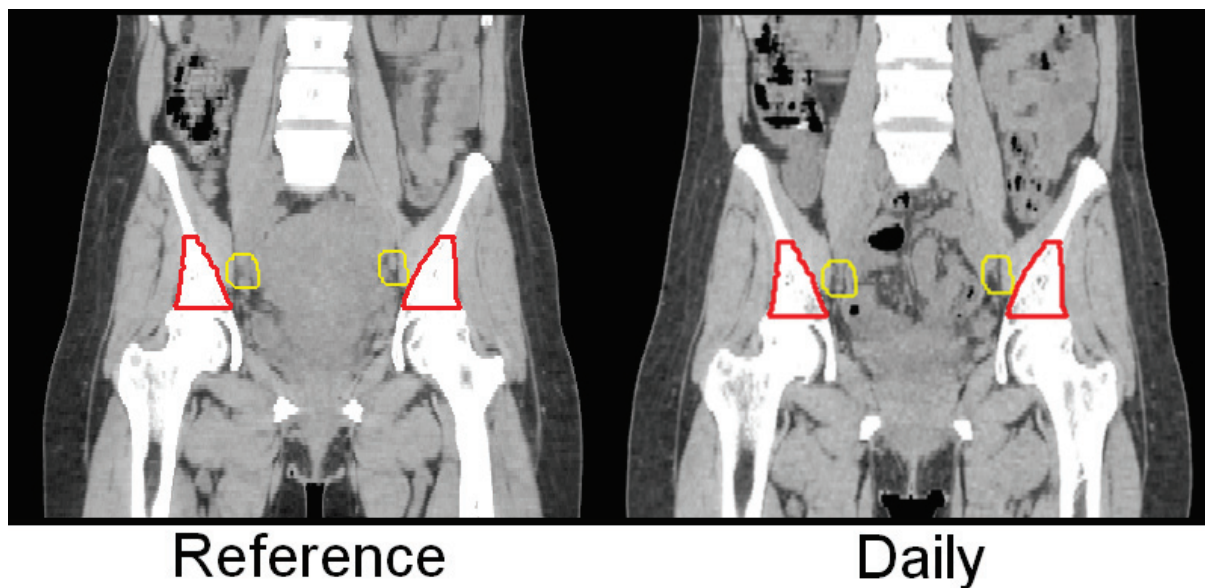


Figure 28: Simulation of daily treatment setup by transferring target contours (yellow) from Reference to Daily CT image sets using bony structures (red).

4.3.4 Calculation of anatomical changes

In this project, we used the ray-tracing method to determine anatomical changes. The method calculates the water-equivalent path-length of parallel rays in the direction of defined beams from the patient surface to the distal and proximal surfaces of the target. The

dimension of each ray size is equivalent to the voxel dimensions of the CT images. Measuring differences in water-equivalent path-length between planning and weekly CT images indicates the magnitude of change in the proton beam range. To evaluate the impact of beam angle on the magnitude of range change due to anatomical variation, we evaluated 8 gantry angles for the treatment of common iliac nodes (from 0° to 315°, at 45° intervals) and 3 gantry angles (90°, 180°, and 270°) for the treatment of external iliac nodes. Using the ray-tracing algorithm, the distal and proximal edges of the nodal contours at each angle for every CT image set were calculated. As shown in Figure 29, each ray-trace results in a 2-dimensional matrix showing the water-equivalent path-length from the beams-eye-view.

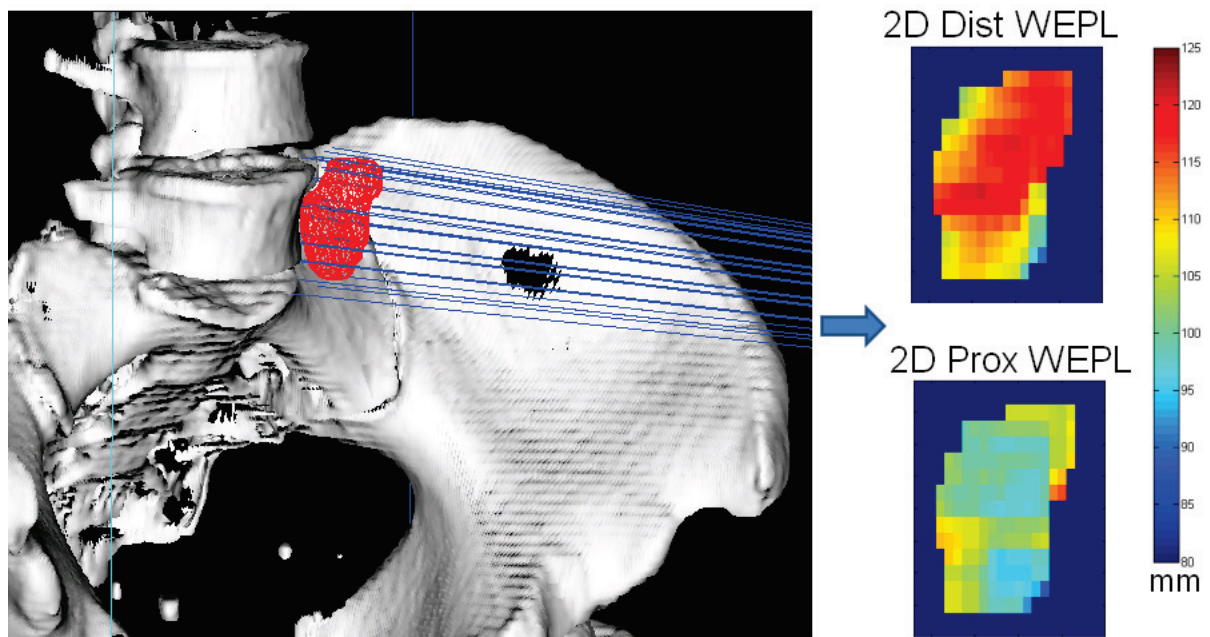


Figure 29: A ray-tracing method was used to determine the water-equivalent path-length (WEPL) from the patient surface to the distal and proximal edges of all targets. Ray tracing is parallel to the treatment beam direction. This method results in two 2-dimensional matrices that represent the distal and proximal WEPL map for each target on any particular computed tomography scan.

4.3.5 Margin calculation

To determine the margin required to ensure coverage of the target in each weekly CT image, the reference water-equivalent path-length matrix (obtained on the planning CT) was subtracted from each weekly matrix, pixel by pixel, for both distal and proximal edges (Figure 30). The margin required to account for anatomical variations in the beam path on any given weekly fraction was defined as the difference corresponding to the 95th percentile of the differences of all the pixels. To determine the margin needed to cover the entire population, all weekly margins were combined, and the mean plus 2 standard deviation was used as the population margin.

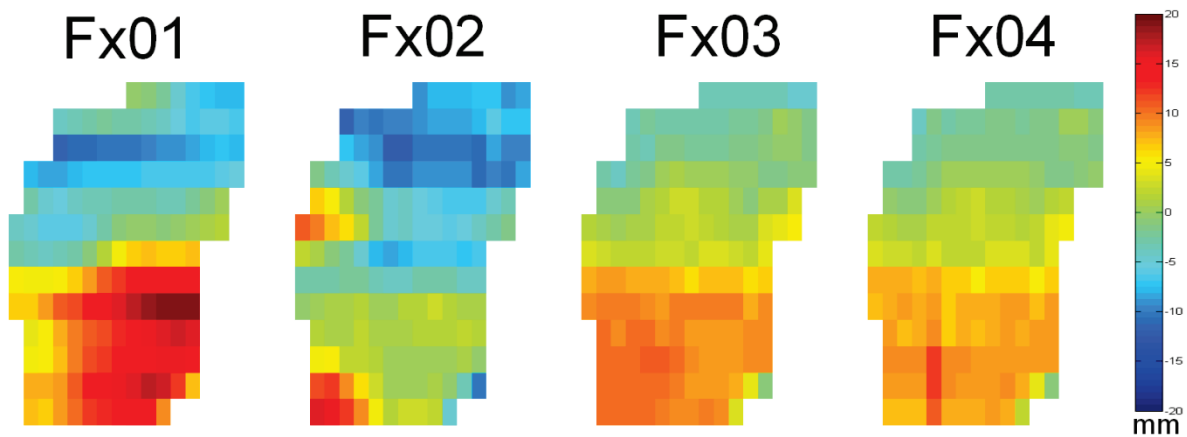


Figure 30: After the water-equivalent path-length (WEPL) maps for both distal and proximal surfaces were obtained on all planning and weekly computed tomography (CT) images, the reference planning maps were subtracted from each daily map to obtain the variation maps. The WEPL difference value to cover 95th percentile of the pixels was used as the margin needed to account for anatomical variations on that particular fraction. Multiple measurements were obtained for each repeat CT image and a group of patients.

4.3.6 Proton Therapy Planning Test Case

To determine the advantages and feasibility of using protons for nodal boosts for cervical cancer, data from a typical cervical cancer patient who had been treated with photon nodal boosts were used. The original clinical prescription for nodal boosts was 10 Gy in 5 fractions to the external iliac nodes and 6 Gy in 3 fractions to the common iliac nodes. Three-field IMRT plans were used for each node. The CT images and all contour delineations were transferred from the original photon therapy plan to the proton therapy plan. Bowel was delineated as the entire peritoneal potential space of bowel. A simulated proton therapy plan was performed in the Eclipse Proton TPS (Varian Medical System, Palo Alto, CA). Two single-field, uniform-dose scanning proton beams, 90° (right lateral) and 180° (PA), were chosen to treat the common iliac region, and a single, 180° (PA) beam was used to treat the external iliac nodes. These angles were chosen because they are associated with the least interfractional anatomical variation (more details shown in Section 4.3.2). Current clinical planning margins, which are 3.5% of the SOBP plus 3 mm, were applied to both distal and proximal edges to account for stopping-power-ratio and dose calculation uncertainties, respectively. The anatomical variation margins derived from this work were also included in addition to current clinical margins. The target dose was normalized to provide coverage similar to that with the original photon therapy plan. Differences in normal tissue dose were analyzed.

4.4 RESULTS

4.4.1 Patient Weight Changes

Out of the 16 patients, 6 patients had 4 weekly CT scans, 9 patients had 5 weekly CT scans, and 1 patient had 6 weekly CT scans. The mean relative weight change between weekly and planning CT scans in this cohort of patients was $-2.3 \pm 2.7\%$, and the maximum relative change was -8.6% (the negative sign represents a weight loss). Seven of the 16 patients had maximum weight loss of greater than 5%.

4.4.2 Distal and Proximal Margin Requirements for Common and External Iliac Nodes

Results for both common iliac and external iliac nodes are shown in Figure 31. For the common iliac nodes, the angles with the greatest anatomical variations were 0° (AP), 45° (left anterior oblique [LAO]), and 315° (right anterior oblique [RAO]). The population proton margin requirements to account for interfractional variations for 0° , 45° , and 315° were 1.9 cm, 1.7 cm, and 2.4 cm, respectively, for the distal edge and 3.0 cm, 2.6 cm, and 3.5 cm, respectively, for the proximal edge. The angles with the least anatomical variations were 90° (left lateral) and 180° (PA). The population planning margin requirements for 90° and 180° were 0.8 cm and 0.9 cm, respectively, for the distal edge and 1.7 cm and 1.4 cm, respectively, for the proximal edge. The remaining angles, 135° (left posterior oblique), 225° (right posterior oblique), and 270° (right lateral), fell somewhere between the 2 extremes, with population margin requirements of 1.2 cm, 1.3 cm, and 1.3 cm, respectively, for the distal edge and 2.1 cm, 2.1 cm, and 1.8 cm, respectively, for the proximal edge.

For the external iliac nodes only interfractional anatomical uncertainties in PA and lateral angles were analyzed because of the strong preference to avoid the central pelvis. For left and right external iliac nodes, the PA margin requirements were 0.8 cm and 0.7 cm, respectively, for the distal edge and 1.0 cm and 1.3 cm, respectively, for the proximal edge. Lateral margin requirements for the left and right external iliac nodes were the same (0.3 cm), for the distal edge and 1.2 cm and 1.3 cm, respectively, for the proximal edge. Combining the left and right nodes and choosing the worst case between the two in each fraction revealed that the population margin requirements for the PA beams were 0.9 cm and 1.3 cm for the distal and proximal edges, respectively. For lateral beams, the population margin requirements were 0.4 cm and 1.4 cm for the distal and proximal edges, respectively.

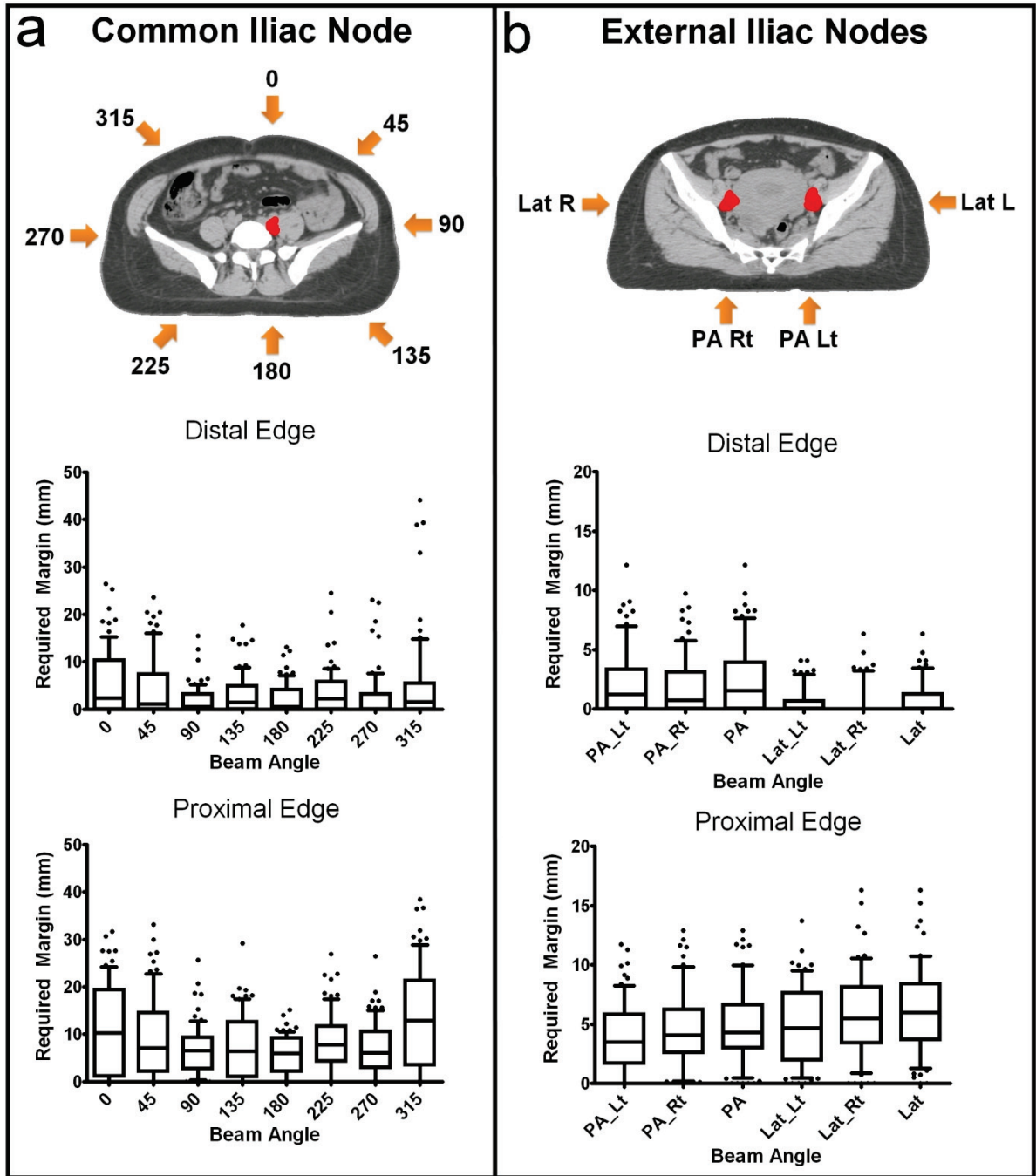


Figure 31: Range margins for common (a) and external iliac (b) nodes were analyzed. Several angles were selected to test the impact of beam angle on the magnitude of change in the proton beam range due to anatomical variation. Box graphs showing median, 75th percentile, 90th percentile, and outliers for both distal and proximal variations are shown.

4.4.3 Comparison of Photon and Proton Dose Distribution in Test Case

We found that the major difference between photon and proton nodal boosts was bowel sparing. Figure 32 shows the dose distribution and dose-volume histogram differences between IMRT and the single-field, uniform-dose proton plan for the sample patient. The difference in target coverage between the 2 modalities was essentially zero, by design. However, the proton dose to the bowel was approximately half the photon dose to the bowel at all dose levels. Using metric guidelines from the Quantitative Analysis of Normal Tissue Effects in the Clinic (QUANTEC) effort (23) indicated that the dose to the 195 cc of the bowel region increased from 2.8 Gy with protons to 5.7 Gy with photons.

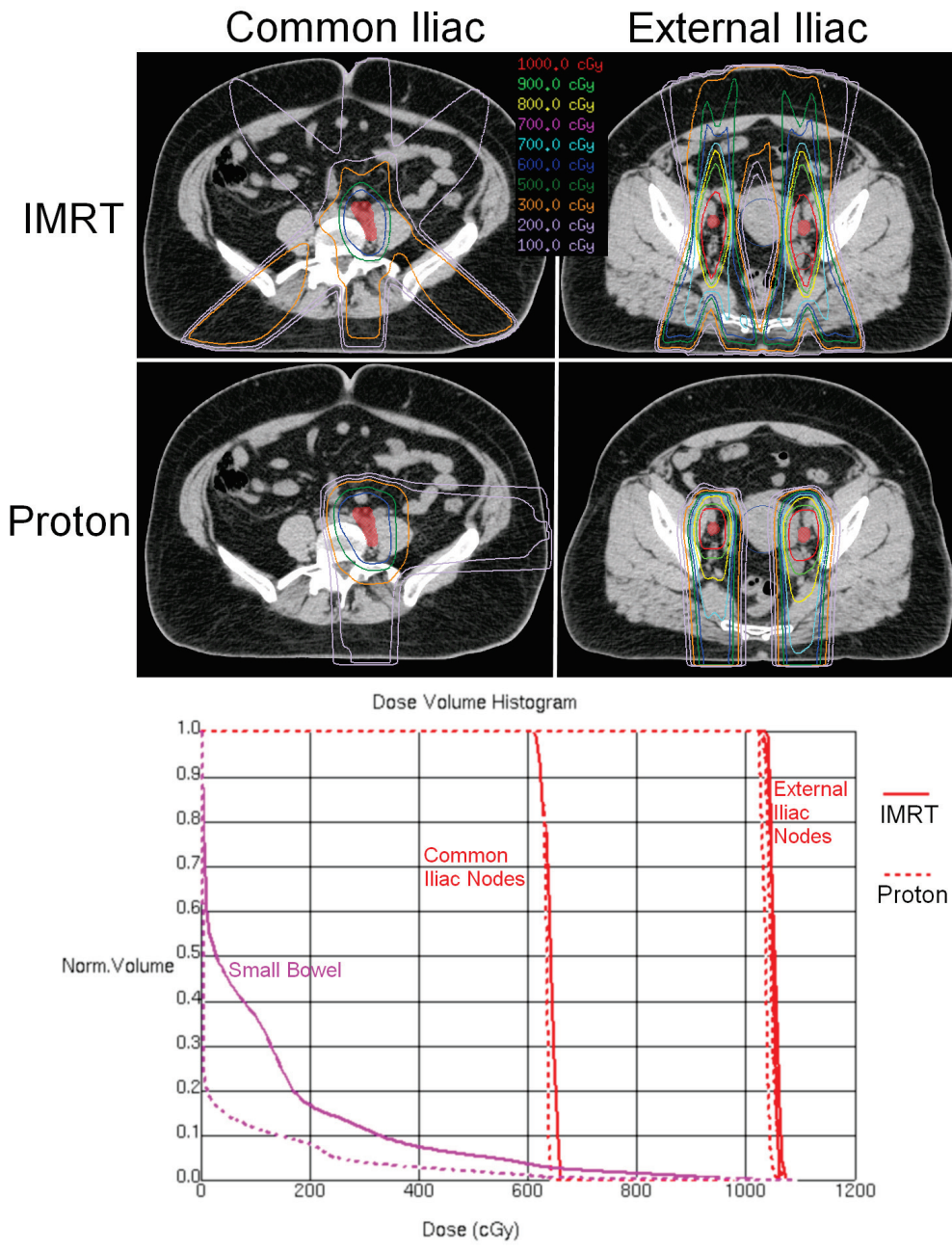


Figure 32: Differences between the dose-volume histograms for intensity-modulated radiation therapy (IMRT) and proton therapy for both common iliac and external iliac nodes. Three-field IMRT plans were used for each node. A 2-field proton plan was used for the common iliac nodes, and a single proton posterior-anterior field was used for the external iliac nodes. The small bowel dose was reduced by half with proton therapy.

4.5 DISCUSSION

Accurate targeting in proton therapy requires the knowledge of range uncertainties during treatment delivery. Interfractional variation of anatomy outside the treatment target could introduce range uncertainties to cause proton beams to shift distally or proximally. Adequate margins are necessary to ensure accurate proton beam delivery especially for treating small targets. Large anatomical variations could potentially shift the distal or proximal edge of the proton beam completely out of the target. It is also important to evaluate range uncertainties as a function of proton beam angles. In this study, we proposed a general approach to construct margins to account for interfractional anatomy variations. We used a ray-tracing method and repeat in-room CT images to quantify beam-specific margin requirement for a group of cervical cancer patients.

Previous studies by Hui et al. and Wang et al. looked at the effects of interfractional anatomical variation during proton therapy (124, 125). However, in those studies, the anatomical sites examined were lung and prostate, and the focus was on evaluating the adequacy of established clinical treatment margins. This work went a step further by calculating the actual required margins. Using protons to boost the dose to the nodes for cervical cancer is a new idea, and the results from this work provide radiation oncologists with adequate information to delivery such therapy with confidence.

4.5.1 Beam Angle Dependence of Interfractional Anatomical Variations

Our results indicate that proton beam uncertainties are very dependent on beam angle selection. Beams passing through the bowel region required margins 2 to 3 times as large as

beams passing at other angles. This is not surprising since bowel contents can vary greatly from day to day, as illustrated in Figure 33a and b. In addition, beams passing through the bowel are not favorable since bowel doses after primary EBRT and brachytherapy may already be close to the maximum tolerated dose. Proton beams at 135° (left posterior oblique) and 225° (right posterior oblique) required less margin than beams passing through the bowel. However, the margin required to account for uncertainties at those angles was still not small. As seen in Figure 33c and d, daily patient setup can greatly affect how much subcutaneous adipose tissue lies between the patient's skin surface and the target. This is the main cause of interfractional variations at those angles. The angles with the lowest uncertainties were the PA and lateral angles. These angles were less affected by bowel content and setup uncertainties.

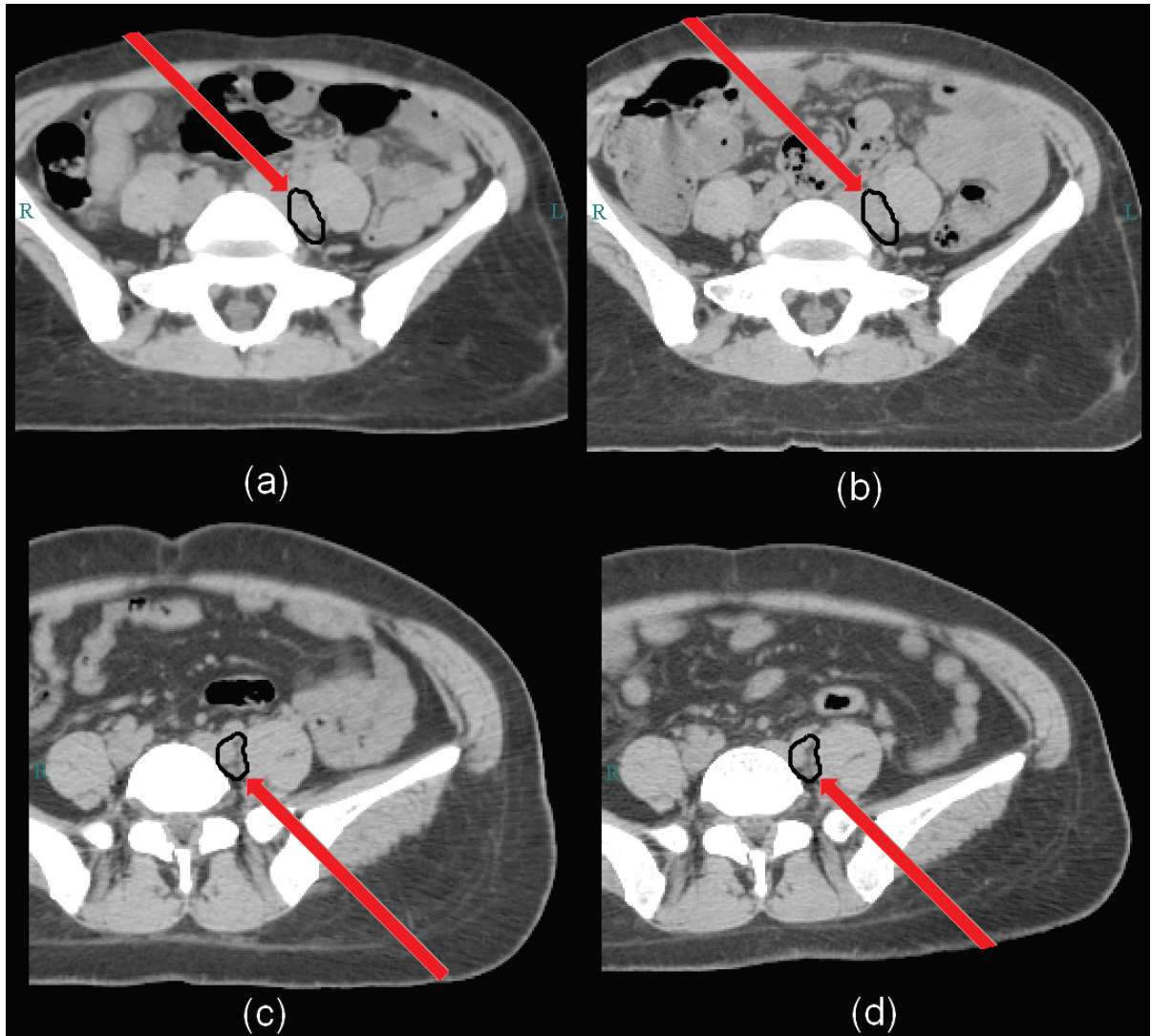


Figure 33: Examples of anatomical variations at different beam angles. Bowel path differences can be seen clearly in (a) and (b) for the 315° (right anterior oblique) angle. Differences in subcutaneous adipose tissue can be seen in (c) and (d). In both cases, differences in range are greater than the spread-out Bragg peak of the beam.

4.5.2 Differences in Distal and Proximal Margin Requirements

Interestingly, our results showed a difference in the magnitude of the required distal and proximal margins. In theory, variations in the beam path should be random. Distal and

proximal required margins should be comparable. However, on average, the required distal margin was 0.8 cm (range, 0.2 to 1.1 cm) smaller than the required proximal margin. We hypothesized that weight loss was a major contributor to the asymmetric margin requirements. Two-tailed Spearman's rho correlations were used to test the statistical significance of the correlation between patient weight change and margin requirements. For common iliac nodes, margin requirements were significantly correlated ($p < 0.01$) with weight change for all angles for both distal and proximal margins except for distal margin requirements at 270° (right lateral). For external iliac nodes, margin requirements were significantly correlated with weight change for all proton beam angles. Correlation coefficients also showed that the magnitude of the proximal margin was directly proportional to the magnitude of weight loss and the magnitude of the distal margin was inversely proportional to the magnitude of weight loss. This is reasonable since proximal margins are required when patients lose weight because the beams will pass through less tissue, thus overshooting the target. Overshooting the target will result in inadequate coverage at the proximal edge. However, from a dosimetric point of view, the proximal fall-off of a proton beam is gradual. The dosimetric impact may not be as significant as in the distal end.

4.5.3 Differences between Common and External Iliac Nodal Margin Requirements

Differences between margin requirements for common and external iliac nodes were analyzed. For PA beams, margin differences between the 2 nodal regions were less than half a millimeter. In the lateral directions, common iliac nodes required an average increase of 0.5 cm and 0.7 cm in the left and right sides, respectively. Once again, weight loss may be a

major contributor to the difference in the lateral beams. Because patient weight loss usually has the largest effect in the abdominal region, common iliac nodes are affected more.

4.5.4 Potential Small Bowel Sparing using Protons for Nodal Boost

Comparison of the IMRT plan with the single-field, uniformly optimized dose proton plan revealed that the sparing in bowel dose was large. The QUANTEC guidelines recommended that the volume of bowel treated to 45 Gy be less than 195 cc (23). However, that dose limit could possibly already have been reached during primary EBRT. Therefore, it is crucial that the small bowel receive minimal additional dose from the boost. With the extra anatomical margins added into our proton therapy plan, it was impossible to totally avoid the bowel region. Nevertheless, the dose to the bowel was reduced by half if protons were used. With that stated, the main focus of this project was angle and margin determination. A dosimetric comparison between proton and photons is beyond the scope of this study.

4.5.5 Assumptions and Limitations

One limitation of this study is the use of a simple ray-trace method. Although this method is fast, it does not account for scatter within the medium. However, the ray-tracing method as a fast dose approximation has been validated by Park et al. (126). In their work, gamma analysis under 3% dose and 3-mm distance-to-agreement criteria was greater than 90%. Another limitation of our study is that CT images were obtained weekly instead of daily. In our clinic, nodal boosts are given in a single week in 5 fractions. Patient may not lose much weight during one week. In this study, we used weekly CT images (because of their availability) and the interfractional anatomical variations are likely to be larger than the

actual interfractional variations in one week. Therefore, the results from this work might have overestimated the margin requirements, especially for patients who lose significant weight.

4.6 CONCLUSION

We have demonstrated a systematic approach to determine population-based anatomical margin requirements for proton therapy. Our ray-tracing approach is not limited to the pelvis and nodal structures; it is universal and can be applied to any disease site. The results of our study indicate that in cervical cancer patients requiring nodal boosts, the optimal treatment angles for common iliac nodes are 90° (left lateral) and 180° (PA) with additional 0.8-cm and 0.9-cm margins, respectively. For external iliac nodes, lateral and PA beams required additional 0.4-cm and 0.9-cm margins, respectively. These results will allow for safe delivery of proton therapy when delivering nodal boosts to patients with cervical cancer.

Chapter 5: Conclusion

5.1 SUMMARY OF THE PROBLEMS, PURPOSE, AND HYPOTHESIS

During a multi-course, multi-modality treatment of cervical cancer, the primary EBRT, ICBT, and external beam nodal boost all contribute substantial dose to the lymph nodes. In many cases, primary EBRT delivers sufficient dose to the nodes to treat microscopic diseases. Radiation boost is only given to patients with positive lymph nodes requiring dose escalation. Prescription of radiation for nodal boost is not straightforward. Many considerations must be taken into account to prevent underdosing the nodal target, which may lead to recurrence or metastasis of disease, while also not overdosing, which could cause normal tissue complexities. Accurate radiation prescription for nodal boost require exact knowledge of previously delivered dose from primary EBRT and ICBT to both the targeted nodes and normal tissues. At MD Anderson, because the second PDR ICBT fraction is delivered post nodal boost, some assumptions about the 2nd ICBT fraction must be made during prescription of nodal boost, which require prior knowledge of potential differences between the two ICBT fractions. Also, current methods of summing bladder and rectum dose using maximum dose points could overestimate when conformal methods such as IMRT are used. Volumetric dose summation needs to be used for more accurate understanding of dose distributions in the normal organs. Prescription of nodal dose is only half of the difficulty; the other half is dose delivery. When photons are used, setups of beam angles always involve tradeoffs and compromises to avoid normal tissues.

The purpose of this project is to improve external beam radiation therapy of lymphatic nodal boost during a course of cervical cancer treatment by: 1) Quantifying interfractional uncertainties. 2) Developing and validating dose accumulation tools between external beam radiation therapy and brachytherapy. 3) Exploring alternative treatment modalities.

The hypothesis of this project is separated into three parts. First, rigid 2D-3D image alignment between films and CT images can be used to quantify nodal dose differences from independent ICBT insertions. Second, deformable image registration can be used to sum normal tissue dose from EBRT and ICBT. Third, ray-tracing methods can be used to determine interfractional anatomical variation margin requirements for proton therapy of nodal boost.

5.2 SPECIFIC AIMS

5.2.1 Specific Aim 1

Specific Aim 1 was to quantify variations in pelvic nodal dose due to applicator placement during a multi-fraction ICBT course. By analyzing differences in positive lymph nodal dose contribution from independent ICBT fractions, we have demonstrated that the mean dose to the nodes can differ by up to 1.9 Gy. However, only 20 percent of nodal dose varied by greater than 1 Gy. Two tailed Spearman's rho correlation tests between tandem angle and length variations, applicator system location variations in the RL, AP, SI directions, total magnitude of applicator system shift, and normalized nodal dose differences from independent ICBT fractions were performed. Tandem angle and total system shifts

were found to impact distal nodal dose differences while AP/PA and lateral shifts were found to impact proximal nodal dose differences.

5.2.2 Specific Aim 2

The goal of Specific Aim 2 was to develop and validate deformable image registration methods for the use of volumetric summation of bladder and rectum dose from ICBT to an external beam planning CT image set. We have successfully developed a method to improve DIR accuracy of bladder and rectum between EBRT and ICBT CT images while creating a voxel-by-voxel method to validate our results. DIR of the bladder and rectum between the EBRT and ICBT image sets were improved by creating a binary image from the original CT images using contours delineated by radiation oncologists. Our novel validation method uses population CT images to generate a pair of simulated CT images with known deformations between them. Validations of our binary method for DIR of bladder and rectum have shown mean deformation error for all voxels to be 4.6 mm and 5.6 mm, respectively.

5.2.3 Specific Aim 3

This aim was to calculate nodal boost planning margins needed for proton therapy to account for interfractional anatomical variations. To determine the required margins, we used a fast ray-tracing method to measure differences in WEPL at the target distal and proximal edges. We used our method to evaluate interfractional anatomical variations in the common iliac and external iliac nodal regions with varying beam angles. We have concluded that beam angles are a major determinant of the margins necessary for patients undergoing proton therapy. Beams passing through the bowel region, where gas content and weight loss may

cause great anatomical variations, require much larger margins than beams entering from other directions.

5.3 TRANSLATING FINDINGS TO THE CLINIC

The results from each one of the three aims can all be independently used to improve current clinical practice. By quantifying the nodal dose variations from independent ICBT fractions, radiation oncologists can refer to the results of Specific Aim 1 when deciding how much extra dose, if necessary, to prescribe to account for the uncertainties in the second ICBT fraction. Also, when conformal radiation therapy is used during external beams and spatial total dose information for the bladder and rectum necessary for evaluation, method developed in Specific Aim 2 can be used to volumetrically deform ICBT dose onto the external beam CT image. Since we also devised a volumetric validation method for our DIR algorithm and calculated the mean errors of DIR in the bladder and rectum, physicists and radiation oncologists understand the limitations and accuracy of the results when evaluating the summed dose.

For dose delivery to the positive nodes, Specific Aim 3 have determined the margins required to ensure target coverage. The margins required to account for interfractional anatomical variations can then be added in quadrature with currently used margins accounting for other proton uncertainties. Since most patients only require a few fractions of nodal boost, treatment with protons for a week should not cause any inconvenience to the patient. Also, by using protons, we take advantage its physical properties and spare normal tissues beyond the distal edge. For patients already experiencing normal tissue complexities

from primary EBRT and ICBT, protons have the potential to spare tissue that would have been impossible to avoid with photons.

5.4 THE END?

Although we have reached conclusive results in all three aims of the project, the knowledge gained from this work will be passed on and be used for future projects. The methodologies and tools developed in this project are universal and can be used in many anatomical sites. Our deformable image registration validation method is extremely useful at a time when dose accumulation using DIR has become much more accessible to the clinic. It is robust and can be used on any treatment site and DIR algorithm. Unlike other validation methods, it does not require intensive and time consuming landmark identification or creating a phantom which might or might not represent the specific patient population and deformation. Also, our method of determining interfractional anatomical variations in proton therapy using ray-tracing method is not just limited to this project. As long as repeat CT images are available for the population of interest, interfractional anatomical variations can be quantified for any target and beam angle. In conclusion, the methods created and used in this project is just as important as the results. My biggest wish is for future researchers to take the methods used in this project and apply it to suit their own specific needs.

Bibliography

1. Birkenhake, S., and R. Sauer. 1995. Historical essentials influencing the development of radiooncology in the past 100 years. *Experientia* 51:681-685.
2. Schneider, U., E. Pedroni, and A. Lomax. 1996. The calibration of CT Hounsfield units for radiotherapy treatment planning. *Phys Med Biol* 41:111-124.
3. Ferlay, J., H. R. Shin, F. Bray, D. Forman, C. Mathers, and D. M. Parkin. 2010. Estimates of worldwide burden of cancer in 2008: GLOBOCAN 2008. *Int J Cancer* 127:2893-2917.
4. Institute, N. C. 2012. Cervical Cancer Home Page.
5. Benedet, J. L., H. Bender, H. Jones, 3rd, H. Y. Ngan, and S. Pecorelli. 2000. FIGO staging classifications and clinical practice guidelines in the management of gynecologic cancers. FIGO Committee on Gynecologic Oncology. *Int J Gynaecol Obstet* 70:209-262.
6. Grigsby, P. W., R. R. Kuske, C. A. Perez, B. J. Walz, M. H. Camel, M. S. Kao, and A. Galakatos. 1987. Medically inoperable stage I adenocarcinoma of the endometrium treated with radiotherapy alone. *Int J Radiat Oncol Biol Phys* 13:483-488.
7. Hamberger, A. D., G. H. Fletcher, and J. T. Wharton. 1978. Results of treatment of early stage I carcinoma of the uterine cervix with intracavitary radium alone. *Cancer* 41:980-985.

8. Grigsby, P. W., and T. J. Herzog. 2001. Current management of patients with invasive cervical carcinoma. *Clin Obstet Gynecol* 44:531-537.
9. Landoni, F., A. Maneo, A. Colombo, F. Placa, R. Milani, P. Perego, G. Favini, L. Ferri, and C. Mangioni. 1997. Randomised study of radical surgery versus radiotherapy for stage Ib-IIa cervical cancer. *Lancet* 350:535-540.
10. Rotman, M., A. Sedlis, M. R. Piedmonte, B. Bundy, S. S. Lentz, L. I. Muderspach, and R. J. Zaino. 2006. A phase III randomized trial of postoperative pelvic irradiation in Stage IB cervical carcinoma with poor prognostic features: follow-up of a gynecologic oncology group study. *Int J Radiat Oncol Biol Phys* 65:169-176.
11. Peters, W. A., 3rd, P. Y. Liu, R. J. Barrett, 2nd, R. J. Stock, B. J. Monk, J. S. Berek, L. Souhami, P. Grigsby, W. Gordon, Jr., and D. S. Alberts. 2000. Concurrent chemotherapy and pelvic radiation therapy compared with pelvic radiation therapy alone as adjuvant therapy after radical surgery in high-risk early-stage cancer of the cervix. *J Clin Oncol* 18:1606-1613.
12. Kumar, L., R. Kaushal, M. Nandy, B. M. Biswal, S. Kumar, A. Kriplani, R. Singh, G. K. Rath, and V. Kochupillai. 1994. Chemotherapy followed by radiotherapy versus radiotherapy alone in locally advanced cervical cancer: a randomized study. *Gynecol Oncol* 54:307-315.
13. Leborgne, F., J. H. Leborgne, R. Doldan, E. Zubizarreta, B. Ortega, J. Maisonneuve, E. Musetti, L. Hekimian, and J. Mezzer. 1997. Induction chemotherapy and radiotherapy of advanced cancer of the cervix: a pilot study and phase III randomized trial. *Int J Radiat Oncol Biol Phys* 37:343-350.

14. Souhami, L., R. A. Gil, S. E. Allan, P. C. Canary, C. M. Araujo, L. H. Pinto, and T. R. Silveira. 1991. A randomized trial of chemotherapy followed by pelvic radiation therapy in stage IIIB carcinoma of the cervix. *J Clin Oncol* 9:970-977.
15. Sundfor, K., C. G. Trope, T. Hogberg, M. Onsrud, J. Koern, E. Simonsen, K. Bertelsen, and R. Westberg. 1996. Radiotherapy and neoadjuvant chemotherapy for cervical carcinoma. A randomized multicenter study of sequential cisplatin and 5-fluorouracil and radiotherapy in advanced cervical carcinoma stage 3B and 4A. *Cancer* 77:2371-2378.
16. Tattersall, M. H., V. Lorvidhaya, V. Vootiprux, A. Cheirsilpa, F. Wong, T. Azhar, H. P. Lee, S. B. Kang, A. Manalo, M. S. Yen, and et al. 1995. Randomized trial of epirubicin and cisplatin chemotherapy followed by pelvic radiation in locally advanced cervical cancer. Cervical Cancer Study Group of the Asian Oceanian Clinical Oncology Association. *J Clin Oncol* 13:444-451.
17. Keys, H. M., B. N. Bundy, F. B. Stehman, L. I. Muderspach, W. E. Chafe, C. L. Suggs, 3rd, J. L. Walker, and D. Gersell. 1999. Cisplatin, radiation, and adjuvant hysterectomy compared with radiation and adjuvant hysterectomy for bulky stage IB cervical carcinoma. *N Engl J Med* 340:1154-1161.
18. Morris, M., P. J. Eifel, J. Lu, P. W. Grigsby, C. Levenback, R. E. Stevens, M. Rotman, D. M. Gershenson, and D. G. Mutch. 1999. Pelvic radiation with concurrent chemotherapy compared with pelvic and para-aortic radiation for high-risk cervical cancer. *N Engl J Med* 340:1137-1143.

19. Rose, P. G., B. N. Bundy, E. B. Watkins, J. T. Thigpen, G. Deppe, M. A. Maiman, D. L. Clarke-Pearson, and S. Insalaco. 1999. Concurrent cisplatin-based radiotherapy and chemotherapy for locally advanced cervical cancer. *N Engl J Med* 340:1144-1153.
20. Whitney, C. W., W. Sause, B. N. Bundy, J. H. Malfetano, E. V. Hannigan, W. C. Fowler, Jr., D. L. Clarke-Pearson, and S. Y. Liao. 1999. Randomized comparison of fluorouracil plus cisplatin versus hydroxyurea as an adjunct to radiation therapy in stage IIB-IVA carcinoma of the cervix with negative para-aortic lymph nodes: a Gynecologic Oncology Group and Southwest Oncology Group study. *J Clin Oncol* 17:1339-1348.
21. McNeil, C. 1999. New standard of care for cervical cancer sets stage for next questions. *J Natl Cancer Inst* 91:500-501.
22. Beadle, B. M., A. Jhingran, M. Salehpour, M. Sam, R. B. Iyer, and P. J. Eifel. 2009. Cervix regression and motion during the course of external beam chemoradiation for cervical cancer. *Int J Radiat Oncol Biol Phys* 73:235-241.
23. Kavanagh, B. D., C. C. Pan, L. A. Dawson, S. K. Das, X. A. Li, R. K. Ten Haken, and M. Miften. 2010. Radiation dose-volume effects in the stomach and small bowel. *Int J Radiat Oncol Biol Phys* 76:S101-107.
24. Michalski, J. M., H. Gay, A. Jackson, S. L. Tucker, and J. O. Deasy. 2010. Radiation dose-volume effects in radiation-induced rectal injury. *Int J Radiat Oncol Biol Phys* 76:S123-129.

25. Viswanathan, A. N., E. D. Yorke, L. B. Marks, P. J. Eifel, and W. U. Shipley. 2010. Radiation dose-volume effects of the urinary bladder. *Int J Radiat Oncol Biol Phys* 76:S116-122.
26. Eifel, P. J., J. Moughan, J. Owen, A. Katz, I. Mahon, and G. E. Hanks. 1999. Patterns of radiotherapy practice for patients with squamous carcinoma of the uterine cervix: patterns of care study. *Int J Radiat Oncol Biol Phys* 43:351-358.
27. Beriwal, S., G. N. Gan, D. E. Heron, R. N. Selvaraj, H. Kim, R. Lalonde, J. L. Kelley, and R. P. Edwards. 2007. Early clinical outcome with concurrent chemotherapy and extended-field, intensity-modulated radiotherapy for cervical cancer. *Int J Radiat Oncol Biol Phys* 68:166-171.
28. Heron, D. E., K. Gerszten, R. N. Selvaraj, G. C. King, D. Sonnik, H. Gallion, J. Comerci, R. P. Edwards, A. Wu, R. S. Andrade, and S. Kalnicki. 2003. Conventional 3D conformal versus intensity-modulated radiotherapy for the adjuvant treatment of gynecologic malignancies: a comparative dosimetric study of dose-volume histograms small star, filled. *Gynecol Oncol* 91:39-45.
29. Lujan, A. E., A. J. Mundt, S. D. Yamada, J. Rotmensch, and J. C. Roeske. 2003. Intensity-modulated radiotherapy as a means of reducing dose to bone marrow in gynecologic patients receiving whole pelvic radiotherapy. *Int J Radiat Oncol Biol Phys* 57:516-521.
30. Mundt, A. J., A. E. Lujan, J. Rotmensch, S. E. Waggoner, S. D. Yamada, G. Fleming, and J. C. Roeske. 2002. Intensity-modulated whole pelvic radiotherapy in women with gynecologic malignancies. *Int J Radiat Oncol Biol Phys* 52:1330-1337.

31. Mundt, A. J., L. K. Mell, and J. C. Roeske. 2003. Preliminary analysis of chronic gastrointestinal toxicity in gynecology patients treated with intensity-modulated whole pelvic radiation therapy. *Int J Radiat Oncol Biol Phys* 56:1354-1360.
32. Portelance, L., K. S. Chao, P. W. Grigsby, H. Bennet, and D. Low. 2001. Intensity-modulated radiation therapy (IMRT) reduces small bowel, rectum, and bladder doses in patients with cervical cancer receiving pelvic and para-aortic irradiation. *Int J Radiat Oncol Biol Phys* 51:261-266.
33. Roeske, J. C., A. Lujan, J. Rotmensch, S. E. Waggoner, D. Yamada, and A. J. Mundt. 2000. Intensity-modulated whole pelvic radiation therapy in patients with gynecologic malignancies. *Int J Radiat Oncol Biol Phys* 48:1613-1621.
34. Salama, J. K., A. J. Mundt, J. Roeske, and N. Mehta. 2006. Preliminary outcome and toxicity report of extended-field, intensity-modulated radiation therapy for gynecologic malignancies. *Int J Radiat Oncol Biol Phys* 65:1170-1176.
35. van de Bunt, L., I. M. Jurgenliemk-Schulz, G. A. de Kort, J. M. Roesink, R. J. Tersteeg, and U. A. van der Heide. 2008. Motion and deformation of the target volumes during IMRT for cervical cancer: what margins do we need? *Radiother Oncol* 88:233-240.
36. Otto, K. 2008. Volumetric modulated arc therapy: IMRT in a single gantry arc. *Med Phys* 35:310-317.
37. Cozzi, L., K. A. Dinshaw, S. K. Shrivastava, U. Mahantshetty, R. Engineer, D. D. Deshpande, S. V. Jamema, E. Vanetti, A. Clivio, G. Nicolini, and A. Fogliata. 2008.

- A treatment planning study comparing volumetric arc modulation with RapidArc and fixed field IMRT for cervix uteri radiotherapy. *Radiother Oncol* 89:180-191.
38. Grigsby, P. W., A. Russell, D. Bruner, P. Eifel, W. J. Koh, W. Spanos, J. Stetz, J. A. Stitt, and J. Sullivan. 1995. Late injury of cancer therapy on the female reproductive tract. *Int J Radiat Oncol Biol Phys* 31:1281-1299.
39. Coia, L., M. Won, R. Lanciano, V. A. Marcial, K. Martz, and G. Hanks. 1990. The Patterns of Care Outcome Study for cancer of the uterine cervix. Results of the Second National Practice Survey. *Cancer* 66:2451-2456.
40. Hanks, G. E., D. F. Herring, and S. Kramer. 1983. Patterns of care outcome studies. Results of the national practice in cancer of the cervix. *Cancer* 51:959-967.
41. Lanciano, R. M., K. Martz, L. R. Coia, and G. E. Hanks. 1991. Tumor and treatment factors improving outcome in stage III-B cervix cancer. *Int J Radiat Oncol Biol Phys* 20:95-100.
42. Lanciano, R. M., M. Won, L. R. Coia, and G. E. Hanks. 1991. Pretreatment and treatment factors associated with improved outcome in squamous cell carcinoma of the uterine cervix: a final report of the 1973 and 1978 patterns of care studies. *Int J Radiat Oncol Biol Phys* 20:667-676.
43. Logsdon, M. D., and P. J. Eifel. 1999. Figo IIIB squamous cell carcinoma of the cervix: an analysis of prognostic factors emphasizing the balance between external beam and intracavitary radiation therapy. *Int J Radiat Oncol Biol Phys* 43:763-775.

44. Montana, G. S., W. C. Fowler, M. A. Varia, L. A. Walton, Y. Mack, and L. Shemanski. 1986. Carcinoma of the cervix, stage III. Results of radiation therapy. *Cancer* 57:148-154.
45. Akine, Y., H. Arimoto, T. Ogino, Y. Kajiura, I. Tsukiyama, S. Egawa, T. Yamada, K. Tanemura, R. Tsunematsu, K. Ohmi, and et al. 1988. High-dose-rate intracavitary irradiation in the treatment of carcinoma of the uterine cervix: early experience with 84 patients. *Int J Radiat Oncol Biol Phys* 14:893-898.
46. Chen, M. S., F. J. Lin, C. H. Hong, C. P. Tu, J. H. Lan, S. G. Tang, W. M. Leung, and T. R. Wang. 1991. High-dose-rate afterloading technique in the radiation treatment of uterine cervical cancer: 399 cases and 9 years experience in Taiwan. *Int J Radiat Oncol Biol Phys* 20:915-919.
47. Kapp, K. S., G. F. Stuecklschweiger, D. S. Kapp, J. Poschauko, H. Pickel, M. Lahousen, and A. Hackl. 1998. Prognostic factors in patients with carcinoma of the uterine cervix treated with external beam irradiation and IR-192 high-dose-rate brachytherapy. *Int J Radiat Oncol Biol Phys* 42:531-540.
48. Lertsanguansinchai, P., C. Lertbutsayanukul, K. Shotelersuk, C. Khorprasert, P. Rojpornpradit, T. Chottetanapasith, A. Srisuthep, S. Suriyapee, C. Jumpangern, D. Tresukosol, and C. Charoonsantikul. 2004. Phase III randomized trial comparing LDR and HDR brachytherapy in treatment of cervical carcinoma. *Int J Radiat Oncol Biol Phys* 59:1424-1431.

49. Nakano, T., S. Kato, T. Ohno, H. Tsujii, S. Sato, K. Fukuhisa, and T. Arai. 2005. Long-term results of high-dose rate intracavitary brachytherapy for squamous cell carcinoma of the uterine cervix. *Cancer* 103:92-101.
50. Patel, F. D., S. C. Sharma, P. S. Negi, S. Ghoshal, and B. D. Gupta. 1994. Low dose rate vs. high dose rate brachytherapy in the treatment of carcinoma of the uterine cervix: a clinical trial. *Int J Radiat Oncol Biol Phys* 28:335-341.
51. Petereit, D. G., and R. Pearcey. 1999. Literature analysis of high dose rate brachytherapy fractionation schedules in the treatment of cervical cancer: is there an optimal fractionation schedule? *Int J Radiat Oncol Biol Phys* 43:359-366.
52. Petereit, D. G., J. N. Sarkaria, D. M. Potter, and J. C. Schink. 1999. High-dose-rate versus low-dose-rate brachytherapy in the treatment of cervical cancer: analysis of tumor recurrence--the University of Wisconsin experience. *Int J Radiat Oncol Biol Phys* 45:1267-1274.
53. Shigematsu, Y., K. Nishiyama, N. Masaki, T. Inoue, Y. Miyata, H. Ikeda, S. Ozeki, Y. Kawamura, and K. Kurachi. 1983. Treatment of carcinoma of the uterine cervix by remotely controlled afterloading intracavitary radiotherapy with high-dose rate: a comparative study with a low-dose rate system. *Int J Radiat Oncol Biol Phys* 9:351-356.
54. Teshima, T., T. Inoue, H. Ikeda, Y. Miyata, K. Nishiyama, S. Murayama, H. Yamasaki, and T. Kozuka. 1993. High-dose rate and low-dose rate intracavitary therapy for carcinoma of the uterine cervix. Final results of Osaka University Hospital. *Cancer* 72:2409-2414.

55. Utley, J. F., C. F. von Essen, R. A. Horn, and J. H. Moeller. 1984. High-dose-rate afterloading brachytherapy in carcinoma of the uterine cervix. *Int J Radiat Oncol Biol Phys* 10:2259-2263.
56. Eifel, P. J. 1992. High-dose-rate brachytherapy for carcinoma of the cervix: high tech or high risk? *Int J Radiat Oncol Biol Phys* 24:383-386; discussion 387-388.
57. Bachtiry, B., A. Dewitt, M. Pintilie, J. Jezioranski, S. Ahonen, W. Levin, L. Manchul, I. Yeung, M. Milosevic, and A. Fyles. 2005. Comparison of late toxicity between continuous low-dose-rate and pulsed-dose-rate brachytherapy in cervical cancer patients. *Int J Radiat Oncol Biol Phys* 63:1077-1082.
58. Brenner, D. J., and E. J. Hall. 1991. Conditions for the equivalence of continuous to pulsed low dose rate brachytherapy. *Int J Radiat Oncol Biol Phys* 20:181-190.
59. Fowler, J., and M. Mount. 1992. Pulsed brachytherapy: the conditions for no significant loss of therapeutic ratio compared with traditional low dose rate brachytherapy. *Int J Radiat Oncol Biol Phys* 23:661-669.
60. Schwarz, G. 1969. An evaluation of the Manchester system of treatment of carcinoma of the cervix. *Am J Roentgenol Radium Ther Nucl Med* 105:579-585.
61. International Commission on Radiation Units and Measurements. 1985. Dose and Volume Specifications for Reporting Intracavitary Therapy in Gynecology. In Bethesda: International Commission on Radiation Units and Measurements.
62. Fellner, C., R. Potter, T. H. Knocke, and A. Wambersie. 2001. Comparison of radiography- and computed tomography-based treatment planning in cervix cancer in

- brachytherapy with specific attention to some quality assurance aspects. *Radiother Oncol* 58:53-62.
63. Pelloski, C. E., M. Palmer, G. M. Chronowski, A. Jhingran, J. Horton, and P. J. Eifel. 2005. Comparison between CT-based volumetric calculations and ICRU reference-point estimates of radiation doses delivered to bladder and rectum during intracavitary radiotherapy for cervical cancer. *Int J Radiat Oncol Biol Phys* 62:131-137.
64. Schoepfel, S. L., M. L. LaVigne, M. K. Martel, D. L. McShan, B. A. Fraass, and J. A. Roberts. 1994. Three-dimensional treatment planning of intracavitary gynecologic implants: analysis of ten cases and implications for dose specification. *Int J Radiat Oncol Biol Phys* 28:277-283.
65. Haie-Meder, C., R. Potter, E. Van Limbergen, E. Briot, M. De Brabandere, J. Dimopoulos, I. Dumas, T. P. Hellebust, C. Kirisits, S. Lang, S. Muschitz, J. Nevinson, A. Nulens, P. Petrow, and N. Wachter-Gerstner. 2005. Recommendations from Gynaecological (GYN) GEC-ESTRO Working Group (I): concepts and terms in 3D image based 3D treatment planning in cervix cancer brachytherapy with emphasis on MRI assessment of GTV and CTV. *Radiother Oncol* 74:235-245.
66. Brookland, R. K., S. Rubin, and B. F. Danoff. 1984. Extended field irradiation in the treatment of patients with cervical carcinoma involving biopsy proven para-aortic nodes. *Int J Radiat Oncol Biol Phys* 10:1875-1879.

67. Cunningham, M. J., C. J. Dunton, B. Corn, J. Noumoff, M. A. Morgan, S. A. King, S. C. Rubin, and J. J. Mikuta. 1991. Extended-field radiation therapy in early-stage cervical carcinoma: survival and complications. *Gynecol Oncol* 43:51-54.
68. Piver, M. S., J. J. Barlow, and R. Krishnamsetty. 1981. Five-year survival (with no evidence of disease) in patients with biopsy-confirmed aortic node metastasis from cervical carcinoma. *Am J Obstet Gynecol* 139:575-578.
69. Podczaski, E., J. A. Stryker, P. Kaminski, B. Ndubisi, J. Larson, K. DeGeest, J. Sorosky, and R. Mortel. 1990. Extended-field radiation therapy for carcinoma of the cervix. *Cancer* 66:251-258.
70. Weiser, E. B., B. N. Bundy, W. J. Hoskins, P. B. Heller, R. R. Whittington, P. J. DiSaia, S. L. Curry, J. Schlaerth, and J. T. Thigpen. 1989. Extraperitoneal versus transperitoneal selective paraaortic lymphadenectomy in the pretreatment surgical staging of advanced cervical carcinoma (a Gynecologic Oncology Group study). *Gynecol Oncol* 33:283-289.
71. Cohn, D. E., F. Dehdashti, R. K. Gibb, D. G. Mutch, J. S. Rader, B. A. Siegel, and T. J. Herzog. 2002. Prospective evaluation of positron emission tomography for the detection of groin node metastases from vulvar cancer. *Gynecol Oncol* 85:179-184.
72. Grigsby, P. W., B. A. Siegel, and F. Dehdashti. 2001. Lymph node staging by positron emission tomography in patients with carcinoma of the cervix. *J Clin Oncol* 19:3745-3749.

73. Grigsby, P. W., B. A. Siegel, F. Dehdashti, J. Rader, and I. Zoberi. 2004. Posttherapy [18F] fluorodeoxyglucose positron emission tomography in carcinoma of the cervix: response and outcome. *J Clin Oncol* 22:2167-2171.
74. Sironi, S., A. Buda, M. Picchio, P. Perego, R. Moreni, A. Pellegrino, M. Colombo, C. Mangioni, C. Messa, and F. Fazio. 2006. Lymph node metastasis in patients with clinical early-stage cervical cancer: detection with integrated FDG PET/CT. *Radiology* 238:272-279.
75. Choi, H. J., W. Ju, S. K. Myung, and Y. Kim. 2010. Diagnostic performance of computer tomography, magnetic resonance imaging, and positron emission tomography or positron emission tomography/computer tomography for detection of metastatic lymph nodes in patients with cervical cancer: meta-analysis. *Cancer Sci* 101:1471-1479.
76. Kidd, E. A., B. A. Siegel, F. Dehdashti, J. S. Rader, D. G. Mutch, M. A. Powell, and P. W. Grigsby. 2010. Lymph node staging by positron emission tomography in cervical cancer: relationship to prognosis. *J Clin Oncol* 28:2108-2113.
77. Fontanilla, H. P., A. H. Klopp, M. E. Lindberg, A. Jhingran, P. Kelly, V. Takiar, R. B. Iyer, C. F. Levenback, Y. Zhang, L. Dong, and P. J. Eifel. 2012. Anatomic distribution of [18F] fluorodeoxyglucose-avid lymph nodes in patients with cervical cancer. *Practical Radiation Oncology*.
78. Ouldamer, L., H. Marret, O. Acker, I. Barillot, and G. Body. 2012. Unusual localizations of sentinel lymph nodes in early stage cervical cancer: A review. *Surg Oncol* 21:e153-157.

79. Mutic, S., R. S. Malyapa, P. W. Grigsby, F. Dehdashti, T. R. Miller, I. Zoberi, W. R. Bosch, J. Esthappan, and D. A. Low. 2003. PET-guided IMRT for cervical carcinoma with positive para-aortic lymph nodes-a dose-escalation treatment planning study. *Int J Radiat Oncol Biol Phys* 55:28-35.
80. Fyles, A. W., M. Pintilie, P. Kirkbride, W. Levin, L. A. Manchul, and G. A. Rawlings. 1995. Prognostic factors in patients with cervix cancer treated by radiation therapy: results of a multiple regression analysis. *Radiother Oncol* 35:107-117.
81. Petereit, D. G., J. N. Sarkaria, R. Chappell, J. F. Fowler, T. J. Hartmann, T. J. Kinsella, J. A. Stitt, B. R. Thomadsen, and D. A. Buchler. 1995. The adverse effect of treatment prolongation in cervical carcinoma. *Int J Radiat Oncol Biol Phys* 32:1301-1307.
82. Girinsky, T., A. Rey, B. Roche, C. Haie, A. Gerbault, H. Randrianarivello, and D. Chassagne. 1993. Overall treatment time in advanced cervical carcinomas: a critical parameter in treatment outcome. *Int J Radiat Oncol Biol Phys* 27:1051-1056.
83. McIntyre, J. F., P. J. Eifel, C. Levenback, and M. J. Oswald. 1995. Ureteral stricture as a late complication of radiotherapy for stage IB carcinoma of the uterine cervix. *Cancer* 75:836-843.
84. Berger, D., J. Dimopoulos, P. Georg, D. Georg, R. Potter, and C. Kirisits. 2007. Uncertainties in assessment of the vaginal dose for intracavitary brachytherapy of cervical cancer using a tandem-ring applicator. *Int J Radiat Oncol Biol Phys* 67:1451-1459.

85. Grigsby, P. W., A. Georgiou, J. F. Williamson, and C. A. Perez. 1993. Anatomic variation of gynecologic brachytherapy prescription points. *Int J Radiat Oncol Biol Phys* 27:725-729.
86. Jones, N. D., J. Rankin, and D. K. Gaffney. 2004. Is simulation necessary for each high-dose-rate tandem and ovoid insertion in carcinoma of the cervix? *Brachytherapy* 3:120-124.
87. Nath, R., L. L. Anderson, G. Luxton, K. A. Weaver, J. F. Williamson, and A. S. Meigooni. 1995. Dosimetry of interstitial brachytherapy sources: recommendations of the AAPM Radiation Therapy Committee Task Group No. 43. American Association of Physicists in Medicine. *Med Phys* 22:209-234.
88. Rivard, M. J., B. M. Coursey, L. A. DeWerd, W. F. Hanson, M. S. Huq, G. S. Ibbott, M. G. Mitch, R. Nath, and J. F. Williamson. 2004. Update of AAPM Task Group No. 43 Report: A revised AAPM protocol for brachytherapy dose calculations. *Med Phys* 31:633-674.
89. Guizar-Sicairos, M., S. T. Thurman, and J. R. Fienup. 2008. Efficient subpixel image registration algorithms. *Opt Lett* 33:156-158.
90. Yu, Z. H., A. H. Klopp, Y. Zhang, P. Eifel, L. Dong, and F. Mourtada. 2011. Using deformable image registration to obtain composite 3D dose for external beam and brachytherapy of cervical cancer treatment. *Brachytherapy* 10:S34-S35.
91. Nag, S., B. Erickson, B. Thomadsen, C. Orton, J. D. Demanes, and D. Petereit. 2000. The American Brachytherapy Society recommendations for high-dose-rate brachytherapy for carcinoma of the cervix. *Int J Radiat Oncol Biol Phys* 48:201-211.

92. Court, L. E., and L. Dong. 2003. Automatic registration of the prostate for computed-tomography-guided radiotherapy. *Med Phys* 30:2750-2757.
93. Smitsmans, M. H., J. de Bois, J. J. Sonke, A. Betgen, L. J. Zijp, D. A. Jaffray, J. V. Lebesque, and M. van Herk. 2005. Automatic prostate localization on cone-beam CT scans for high precision image-guided radiotherapy. *Int J Radiat Oncol Biol Phys* 63:975-984.
94. Zhou, J., B. Uhl, K. Dewit, M. Young, B. Taylor, D. Y. Fei, and Y. C. Lo. 2010. Analysis of daily setup variation with tomotherapy megavoltage computed tomography. *Med Dosim* 35:31-37.
95. Bookstein, F. L. 1989. Principal warps: thin-plate splines and the decomposition of deformations. *Pattern Analysis and Machine Intelligence, IEEE Transactions on* 11:567-585.
96. Brock, K. K., M. B. Sharpe, L. A. Dawson, S. M. Kim, and D. A. Jaffray. 2005. Accuracy of finite element model-based multi-organ deformable image registration. *Med Phys* 32:1647-1659.
97. Chui, H., and A. Rangarajan. 2003. A new point matching algorithm for non-rigid registration. *Comput. Vis. Image Underst.* 89:114-141.
98. Fornefett, M., K. Rohr, and H. S. Stiehl. 1999. Elastic registration of medical images using radial basis functions with compact support. In *Computer Vision and Pattern Recognition, 1999. IEEE Computer Society Conference on.* 407 Vol. 401.

99. Xie, Y., M. Chao, and L. Xing. 2009. Tissue feature-based and segmented deformable image registration for improved modeling of shear movement of lungs. *Int J Radiat Oncol Biol Phys* 74:1256-1265.
100. Coselmon, M. M., J. M. Balter, D. L. McShan, and M. L. Kessler. 2004. Mutual information based CT registration of the lung at exhale and inhale breathing states using thin-plate splines. *Med Phys* 31:2942-2948.
101. Foskey, M., B. Davis, L. Goyal, S. Chang, E. Chaney, N. Strehl, S. Tomei, J. Rosenman, and S. Joshi. 2005. Large deformation three-dimensional image registration in image-guided radiation therapy. *Phys Med Biol* 50:5869-5892.
102. Lu, W., M. L. Chen, G. H. Olivera, K. J. Ruchala, and T. R. Mackie. 2004. Fast free-form deformable registration via calculus of variations. *Phys Med Biol* 49:3067-3087.
103. Thirion, J. P. 1998. Image matching as a diffusion process: an analogy with Maxwell's demons. *Med Image Anal* 2:243-260.
104. Wang, H., L. Dong, J. O'Daniel, R. Mohan, A. S. Garden, K. K. Ang, D. A. Kuban, M. Bonnen, J. Y. Chang, and R. Cheung. 2005. Validation of an accelerated 'demons' algorithm for deformable image registration in radiation therapy. *Phys Med Biol* 50:2887-2905.
105. Bennett, C. H. 1982. The thermodynamics of computation-a review. *International Journal of Theoretical Physics* 21:905-940.
106. Starkschall, G., K. Britton, M. F. McAleer, M. D. Jeter, M. R. Kaus, K. Bzdusek, R. Mohan, and J. D. Cox. 2009. Potential dosimetric benefits of four-dimensional radiation treatment planning. *Int J Radiat Oncol Biol Phys* 73:1560-1565.

107. Klopp, A. H., F. Mourtada, Z. H. Yu, B. M. Beadle, M. F. Munsell, A. Jhingran, and P. J. Eifel. 2012. Pilot study of a computed tomography-compatible shielded intracavitary brachytherapy applicator for treatment of cervical cancer. *Practical Radiation Oncology* (In Press).
108. Price, M. J., E. F. Jackson, K. A. Gifford, P. J. Eifel, and F. Mourtada. 2009. Development of prototype shielded cervical intracavitary brachytherapy applicators compatible with CT and MR imaging. *Med Phys* 36:5515-5524.
109. Boswell, S., W. Tome, R. Jeraj, H. Jaradat, and T. R. Mackie. 2006. Automatic registration of megavoltage to kilovoltage CT images in helical tomotherapy: an evaluation of the setup verification process for the special case of a rigid head phantom. *Med Phys* 33:4395-4404.
110. Gay, H. A., H. J. Barthold, E. O'Meara, W. R. Bosch, I. El Naqa, R. Al-Lozi, S. A. Rosenthal, C. Lawton, W. R. Lee, H. Sandler, A. Zietman, R. Myerson, L. A. Dawson, C. Willett, L. A. Kachnic, A. Jhingran, L. Portelance, J. Ryu, W. Small, Jr., D. Gaffney, A. N. Viswanathan, and J. M. Michalski. 2012. Pelvic normal tissue contouring guidelines for radiation therapy: a Radiation Therapy Oncology Group consensus panel atlas. *Int J Radiat Oncol Biol Phys* 83:e353-362.
111. Dice, L. R. 1945. Measures of the Amount of Ecologic Association Between Species. *Ecology* 26:297-302.
112. Zou, K. H., S. K. Warfield, A. Bharatha, C. M. Tempany, M. R. Kaus, S. J. Haker, W. M. Wells, 3rd, F. A. Jolesz, and R. Kikinis. 2004. Statistical validation of image segmentation quality based on a spatial overlap index. *Acad Radiol* 11:178-189.

113. Cootes, T., A. Hill, C. Taylor, and J. Haslam. 1994. Use of active shape models for locating structures in medical images. *Image and Vision Computing* 12:355-365.
114. Schultheiss, T. E., W. A. Tome, and C. G. Orton. 2012. Point/counterpoint: it is not appropriate to "deform" dose along with deformable image registration in adaptive radiotherapy. *Med Phys* 39:6531-6533.
115. Castillo, R., E. Castillo, R. Guerra, V. E. Johnson, T. McPhail, A. K. Garg, and T. Guerrero. 2009. A framework for evaluation of deformable image registration spatial accuracy using large landmark point sets. *Phys Med Biol* 54:1849-1870.
116. Kirby, N., C. Chuang, and J. Pouliot. 2011. A two-dimensional deformable phantom for quantitatively verifying deformation algorithms. *Med Phys* 38:4583-4586.
117. Kirby, N., C. Chuang, U. Ueda, and J. Pouliot. 2013. The need for application-based adaptation of deformable image registration. *Med Phys* 40:011702.
118. Lawson, J. D., E. Schreibmann, A. B. Jani, and T. Fox. 2007. Quantitative evaluation of a cone-beam computed tomography-planning computed tomography deformable image registration method for adaptive radiation therapy. *J Appl Clin Med Phys* 8:2432.
119. 2013. Particle Therapy Co-Operative Group: Particle therapy facilities in operation.
120. Lomax, A. J. 2008. Intensity modulated proton therapy and its sensitivity to treatment uncertainties 2: the potential effects of inter-fraction and inter-field motions. *Phys Med Biol* 53:1043-1056.

121. Lomax, A. J. 2008. Intensity modulated proton therapy and its sensitivity to treatment uncertainties 1: the potential effects of calculational uncertainties. *Phys Med Biol* 53:1027-1042.
122. Moyers, M. F., M. Sardesai, S. Sun, and D. W. Miller. 2010. Ion stopping powers and CT numbers. *Med Dosim* 35:179-194.
123. Zhang, L., L. Dong, L. Court, H. Wang, M. Gillin, and R. Mohan. 2005. Validation of CT-Assisted targeting (CAT) software for soft tissue and bony target localization. *Medical Physics* 32:2106-2106.
124. Hui, Z., X. Zhang, G. Starkschall, Y. Li, R. Mohan, R. Komaki, J. D. Cox, and J. Y. Chang. 2008. Effects of interfractional motion and anatomic changes on proton therapy dose distribution in lung cancer. *Int J Radiat Oncol Biol Phys* 72:1385-1395.
125. Wang, Y., J. A. Efstathiou, G. C. Sharp, H. M. Lu, I. F. Ciernik, and A. V. Trofimov. 2011. Evaluation of the dosimetric impact of interfractional anatomical variations on prostate proton therapy using daily in-room CT images. *Med Phys* 38:4623-4633.
126. Park, P. C., J. Cheung, X. R. Zhu, N. Sahoo, L. Court, and L. Dong. 2012. Fast range-corrected proton dose approximation method using prior dose distribution. *Phys Med Biol* 57:3555-3569.

Vita

Zhiqian Henry Yu was born in Wuhan, China on January 24th, 1984, the first of two sons to Liming Yu and Siqun Chen. He moved to Canada when he was 10 years old and lived in Toronto and Montreal for 4 years total. Finally, at the age of 14, he moved to Houston and stayed in Texas for the next 15 years. He attended the University of Texas at Austin between 2002 and 2006 and graduated with a B.S. in Physics. After graduation, he became a Research Assistant at the Department of Radiation at UT MD Anderson Cancer Center. He entered the University of Texas Health Science Center at Houston Graduate School of Biomedical Sciences in Fall 2008 with the dream of obtaining a Ph.D. degree in Medical Physics.

Permanent Address:

8106 Bulrush Canyon Trl

Katy, TX 77494